

# UNSTEADY AERODYNAMICS OF LOW-PRESSURE STEAM TURBINES OPERATING UNDER LOW VOLUME FLOW CONDITIONS

THÈSE N° 6096 (2014)

PRÉSENTÉE LE 16 MAI 2014

À LA FACULTÉ DES SCIENCES ET TECHNIQUES DE L'INGÉNIEUR  
LABORATOIRE DE THERMIQUE APPLIQUÉE ET DE TURBOMACHINES  
PROGRAMME DOCTORAL EN ENERGIE

ÉCOLE POLYTECHNIQUE FÉDÉRALE DE LAUSANNE

POUR L'OBTENTION DU GRADE DE DOCTEUR ÈS SCIENCES

PAR

**Benjamin MEGERLE**

acceptée sur proposition du jury:

Dr M. Farhat, président du jury  
Dr P. Ott, Dr I. W. McBean, directeurs de thèse  
Prof. D. Favrat, rapporteur  
Prof. T. Fransson, rapporteur  
Prof. F. Truckenmüller, rapporteur



ÉCOLE POLYTECHNIQUE  
FÉDÉRALE DE LAUSANNE

Suisse  
2014



## Acknowledgements

This work was conducted during my employment at ALSTOM (Switzerland) Ltd. in cooperation with the Group of Thermal Turbomachinery at the École Polytechnique Fédérale de Lausanne (EPFL) under the direction of Dr Peter Ott. First I like to thank ALSTOM as a company giving me the chance to elaborate a dissertation by providing the funding and giving me the required time. I have to thank Dr Peter Walker, Dr Michael Sell, Dr Ivan McBean and Dr Thomas Mokulys for supporting my plans to do a PhD and the trust given to me. I would also like to thank Luca Ripamonti for supporting my thesis as my department manager.

ALSTOM and the EPFL have provided me with an enriching environment for doing high-level research. Despite the distance, Dr Peter Ott gave me the best support as my Thesis Director at the EPFL by closely following and reviewing my work. His experience and different background was of great benefit. Peter, thank you for helping me to make my project an achievement in the academic world. I also appreciate that I was always very warmly welcomed by the whole staff of the institute during my visits to Lausanne. Thank for your hospitality.

Inside ALSTOM, I want to highlight two persons, which were essential to the success of my research.

Dr Ivan McBean, my Thesis Co-Director and Group Leader, who has followed the project over the years the closest, providing supervision and essential input in countless discussions and meetings. Thank you Ivan for the trust in me and for your commitment to the project.

Without comparison to measurement, CFD is really only “Colourful Fluid Dynamics”. Thanks to Tim Rice from the ALSTOM Turbine Testing Facility in Rugby, I received high quality measurement data to validate my numerical results. Thank you Tim for having time for me even in the busiest days and for sharing your broad knowledge.

My thanks go also to all the other colleges who supported my work, the testing team in St. Petersburg, for the hospitality they showed to me during my visit to the test facility and the members of the aero team in Baden for the good working environment.

I would like to dedicate this thesis to my father who passed away in February 2013. He taught me to value education and sparked my interest in technology. Without him, I would have never come so far in my career as an engineer. Special thanks also go to my family and to my fiancée Carolina for their loving support.

## Abstract

The diversification of power generation methods within existing power networks has increased the requirement for operational flexibility of power plants employing steam turbines. This has led to the situation where steam turbines may operate at very low volume flow (LVF) conditions for extended periods. Under operating conditions where the volume flow through the last stage moving blades (LSMBs) of a low-pressure (LP) steam turbine is below a certain limit, energy is returned to the working fluid rather than being extracted. This so-called “ventilation” phenomenon can produce non-synchronous aerodynamic excitation, which has the potential to lead to high dynamic blade loading. The aerodynamic excitation is a result of a rotating phenomenon, with similarities to rotating stall, which is well known in compressors.

Non-synchronous excitation under low volume operation can be a major risk to the mechanical integrity of LSMBs in LP steam turbines. Currently extensive validation of new blade designs is required to clarify whether they are subjected to the risk of not admissible blade vibration. Such tests are usually performed at the end of a blade development project. If resonance occurs a costly redesign is required, which may also lead to a reduction of performance. It is therefore of great interest to be able to predict correctly the unsteady flow phenomena and their effects.

Detailed measurements have been performed in a single stage model LP steam turbine operated with air and a multi-stage model LP steam turbine operated with steam under ventilation conditions. The analysis revealed that the rotating excitation mechanism observed in operating steam turbines, is reproduced in the model turbines. Numerical simulation has been applied to simulate the unsteady flow in the two model turbines. The numerical model consists of the last stage modelled as a full annulus, as well as the axial-radial diffuser. An unsteady computational fluid dynamics (CFD) analysis has been performed with sufficient rotor revolutions to obtain a globally time periodic flow. The simulation reproduces the main characteristics of the phenomenon observed in the tests. The CFD modelling has been further enhanced by applying scale-resolving turbulence modelling, which allows resolving large-scale turbulent fluctuations to occur. With this type of modelling qualitative and quantitative agreement between CFD and measurement for the unsteady and time averaged flow field has been achieved for both model turbines.

The results of the numerical investigation allow for a detailed insight into the dynamic flow field and reveals information on the nature of the excitation mechanism. The propagation mechanism of the stall cells is explained and comparison is made with compressor rotating stall theory. Different effects on the stall cells such as changing flow coefficient, the exhaust geometry and the LSMB tip clearance have been investigated. It has been concluded that the CFD approach developed can be used to assess LSMB blade designs prior to model turbine tests to check whether they are subjected to vibration under LVF caused by the rotating excitation mechanism. The model turbine testing becomes then the verification rather than a testing of the new LSMB design.

**Keywords:** low-pressure steam turbine, low-volume flow, blade excitation, unsteady aerodynamics, rotating stall, unsteady CFD.

## Zusammenfassung

Die Diversifikation der Energieerzeugung in bestehenden Verbundnetzen erfordert eine höhere Flexibilität von Dampfkraftwerken. Dies führt dazu, dass Dampfturbinen über längere Zeiträume mit sehr geringen Volumenströmen betrieben werden. Unter diesen Betriebsbedingungen fällt der Volumenstrom durch die Endstufenlaufschaufelreihe der Niederdruckdampfturbine unter einen bestimmten Grenzwert, ab welchem dem Dampf Energie zugeführt wird anstatt entzogen. Dieser Zustand wird oft als Ventilation bezeichnet und kann mit hohen dynamischen Schaufelbelastungen verbunden sein, welche durch eine asynchrone aerodynamische Anregung erzeugt werden. Diese Anregung ist das Ergebnis eines rotierenden Phänomens, welches Ähnlichkeiten zur der rotierenden Ablösung in Kompressoren hat.

Asynchrone Schaufelanregung unter Ventilationsbetrieb bedeutet ein hohes Risiko für die strukturelle Sicherheit von Niederdruck-Endstufenlaufschaufeln. Neue Schaufeldesigns benötigen deshalb eine ausgiebige Validierung in einer Modellturbine. Solche Untersuchungen werden typischerweise am Ende eines Schaufelentwicklungsprogramms durchgeführt. Treten hohe Schaufelvibrationen auf, ist eine aufwendige Neuauslegung erforderlich, welche auch zu einer Verringerung des Wirkungsgrades führen kann. Es ist deshalb von großem Interesse, die instationäre Aerodynamik unter diesen Bedingungen zuverlässig vorhersagen zu können, um mögliche Vibrationsprobleme auszuschließen.

Zur Untersuchung der umlaufenden Anregung wurden detaillierte Messungen in einer einstufigen mit Luft betriebenen Modellturbine und einer mehrstufigen mit Dampf betriebenen Modellturbine unter Ventilationsbetrieb durchgeführt. Es wurde nachgewiesen, dass die in Dampfturbinen beobachtete rotierende Ablösung auch in beiden Modellturbinen auftritt. In einem zweiten Schritt wurde eine numerische Untersuchung der instationären Aerodynamik beider Modellturbinen durchgeführt. Das Rechenetz besteht aus der kompletten Endstufe und dem Diffusor modelliert als voller Annulus sowie dem Abdampfgehäuse. Die instationäre Simulation wurde für eine ausreichende Zahl von Rotorumdrehungen durchgeführt bis sich ein global zeitperiodisches Strömungsfeld einstellt. Es zeigt sich, dass die Simulation die zentralen Eigenschaften der umlaufenden Ablösung wiedergibt. Um eine bessere Übereinstimmung der quantitativen instationären Größen zu erreichen, wurde die Modellierung weiter durch die Auflösung großskaliger turbulenter Fluktuationen verbessert. Mit dieser Modellierung wurde eine quantitative Übereinstimmung zwischen numerischer Simulation und den experimentellen Ergebnissen für beide Modellturbinen erreicht.

Die Ergebnisse der numerischen Simulation geben einen detaillierten Einblick in das dynamische Strömungsfeld und ermöglichen die Analyse der strömungsmechanischen Eigenschaften des Anregungsphänomens. Die Ausbreitung der Ablösezellen in Umfangsrichtung kann ebenso erklärt werden, wie auch der Zusammenhang mit der von Kompressoren bekannten rotierenden Ablösung. Zusätzlich wurden verschiedene Einflüsse auf die umlaufenden Ablösezellen untersucht. Dazu gehören die Abhängigkeit von der Durchflusszahl, der Geometrie des Abdampfgehäuses und dem Laufschaufelradialspalt. Es kann geschlossen werden, dass der hier entwickelte numerische Ansatz zur Analyse von neuen Endstufenschaufeldesigns vor der Modellturbinenvalidierung benutzt werden kann, um eine Laufschaufelanregung durch die rotierende Ablösung vorherzusagen.

**Stichworte:** Niederdruckdampfturbine, Schwachlast, Schaufelanregung, instationäre Aerodynamik, rotierende Ablösung, numerische Strömungssimulation.

# Table of contents

<b>Acknowledgements .....</b>	<b>I</b>
<b>Abstract .....</b>	<b>II</b>
<b>Zusammenfassung .....</b>	<b>III</b>
<b>List of figures .....</b>	<b>VI</b>
<b>Nomenclature .....</b>	<b>IX</b>
<b>1. Introduction .....</b>	<b>1</b>
<b>2. Literature review.....</b>	<b>4</b>
2.1 Low pressure steam turbines under low volume flow .....	4
2.1.1 Time averaged flow field .....	4
2.1.2 Blade excitation.....	5
2.1.3 Unsteady flow field .....	7
2.1.4 Numerical investigations .....	9
2.2 Unsteady effects in turbomachines.....	10
2.2.1 Turbulence .....	10
2.2.2 Rotor stator interaction and vortex shedding .....	12
2.2.3 Flutter.....	12
2.2.4 Surge and rotating stall .....	13
2.2.5 Concluding remarks on known unsteady effects .....	15
<b>3. Measurement and modelling methods.....</b>	<b>16</b>
3.1 Measurement methods.....	16
3.1.1 Similarity .....	17
3.1.2 Air model turbine .....	19
3.1.3 Steam model turbine .....	22
3.1.4 Measurement techniques .....	27
3.2 Numerical modelling .....	32
3.2.1 Flow solver.....	33
3.2.2 Computational mesh .....	33
3.2.3 Fluid modelling.....	38
3.2.4 Time accurate modelling .....	38
3.2.5 Turbulence modelling.....	39
<b>4. Results and discussion.....</b>	<b>45</b>
4.1 CFD test cases.....	45
4.1.1 Backward facing step and mixing plane .....	45
4.1.2 Rotating stall in a vaneless diffuser .....	47
4.2 Air model turbine .....	50
4.2.1 Time averaged flow field .....	50
4.2.2 Unsteady flow field .....	52

4.2.3	Rotating stall cells flow structure .....	55
4.2.4	Summary air model turbine .....	57
4.3	Steam model turbine .....	57
4.3.1	Steady state single passage calculation with equilibrium steam .....	58
4.3.2	Realistic exhaust geometry .....	60
4.3.3	Influence of the exhaust on the unsteady flow behaviour .....	62
4.3.4	Comparison to the air model turbine.....	62
4.4	Scale-resolving turbulence modelling .....	65
4.5	Flow coefficient influence.....	72
4.6	Tip gap influence .....	75
4.7	Exhaust influence .....	77
4.8	Flow physics and stall cell propagation mechanism.....	80
<b>5.</b>	<b>Conclusions.....</b>	<b>87</b>
<b>6.</b>	<b>Proposals for further investigations .....</b>	<b>89</b>
<b>7.</b>	<b>References .....</b>	<b>90</b>
	<b>Appendix: Air model turbine stall cell visualisation.....</b>	<b>93</b>
	<b>Curriculum vitae.....</b>	<b>96</b>

## List of figures

Figure 1: Typical steam turbine train of a conventional coal fired power plant, indicated with dashed circles: Last Stage Moving Blades (LSMBs) .....	2
Figure 2: General characteristic of a turbine stage over flow coefficient .....	2
Figure 3: Characteristic meridional flow field of a LP steam turbine under low volume flow operation.....	5
Figure 4: Schematic of alternating stress over flow coefficient for a case with non-synchronous excitation, see [7] .....	6
Figure 5: Energy content of the different turbulence scales .....	11
Figure 6: Rotating stall mechanism in axial compressors .....	13
Figure 7: LSMB tip pressure ratio as a function of volume flow .....	15
Figure 8: Meridional view of the air model turbine with traversing locations.....	20
Figure 9: Carpet intensity plot recorded by the strain gauge (arbitrary contour scale) and the dynamic pressure probe (contour in [mbar] (RMS)).....	21
Figure 10: Cross-section of the steam model turbine, see [37].....	23
Figure 11: Exhaust hood of the investigated steam turbine model.....	23
Figure 12: (a) Cross-sectional view of the steam model turbine rear stage, (b) Upstream view of plane 62, probe traverse locations marked in red .....	24
Figure 13: Strain gauge locations on the LSMB of the steam model turbine, location 11 thermal couples.....	25
Figure 14: Measurement result from the steam model turbine, carpet intensity plot recorded by the strain gauge (arbitrary contour scale) and the dynamic pressure probe (contour in [mbar] (RMS)) .....	26
Figure 15: Seven hole disk probe head.....	29
Figure 16: Kiel probe head, probes for the air model (top) and in the steam model (bottom).....	30
Figure 17: Coarse grid at mid span .....	34
Figure 18: Exhaust configurations.....	35
Figure 19: LSMB tip gap mesh.....	36
Figure 20: CFD model with realistic exhaust configuration .....	37
Figure 21: Pressure signal between stator vane and rotor blade at 80% span from a representative transient calculation .....	39
Figure 22: Idealized spectrum of turbulence with different turbulence modelling strategies .	42
Figure 23: Geometry of the backward facing step .....	45
Figure 24: Computational mesh detail with mixing plane.....	46
Figure 25: Measurement versus CFD axial velocity profiles, measurement results from Schulte [48].....	47
Figure 26: Flow field after rotating stall has been established .....	48
Figure 27: Instantaneous helicity under rotating stall with different turbulence models .....	49
Figure 28: Blending factor for the SAS-SST turbulence model .....	49
Figure 29: Meridional flow field (blue arrows: time averaged measurement, red arrows: steady state CFD) .....	51



Figure 30: Circumferential velocity in front and behind the rotor blade .....	52
Figure 31: FFT for one static pressure monitor point between stator and rotor, 80% span, CFD, relative frame of reference .....	53
Figure 32: Unsteady pressure amplitude for different cell counts, the traverse positions are shown in Figure 12, page 24 .....	54
Figure 33: Rotor blade leading edge plane, axial velocity.....	55
Figure 34: One cell passing in the relative frame at 50% span with relative velocity vectors in the blade-to-blade plane, radial velocity as contour and indicative white arrows .....	56
Figure 35: Inter-blade space plane with deviation of the axial Mach number from circumferential average value, left: Measurement, right: CFD .....	57
Figure 36: Meridional cross-section of the full steam model turbine cylinder including the axial radial exhaust, blade rows in grey.....	58
Figure 37: Expansion lines for different volume flows, four stage CFD result - steam model turbine.....	59
Figure 38: LSMB blade surface temperature measured at the strain gauge location G, see Figure 13.....	60
Figure 39: Time averaged flow field downstream of the steam model turbine LSMB in plane 62, see Figure 12 .....	61
Figure 40: FFT analysis of 10 rotor revolutions, static pressure in plane 61 at 95% span height.....	62
Figure 41: Circumferentially averaged meridional stream lines from CFD at $v_x/u_{hub}=0.06$ ....	63
Figure 42: Unsteady pressure traverses for CFD and measurement, pressure amplitude of dominant cell pattern at $v_x/u_{hub}=0.06$ .....	64
Figure 43: Blade-to-blade view at 70% span with radial velocity contour normalized with $u_{hub}$ and projected flow vectors at $v_x/u_{hub}=0.06$ (profile geometry is indicative for confidentiality reasons).....	65
Figure 44: Spanwise distribution of time averaged flow velocity in the 62 plane of the steam model turbine .....	66
Figure 45: Iso-surface to detect vortex structures: Q-Criterion: $Q=\Omega^2-S^2$ ( $S$ = Strain rate, $\Omega$ = vorticity rate) = $10e7$ , eddy viscosity contour on the iso-surface.....	67
Figure 46: Circumferentially averaged eddy viscosity in a meridional plane of stator and rotor, steam model turbine .....	68
Figure 47: Time moving FFT for a pressure monitor point between stator and rotor at 87% span, SST turbulence model, steam model turbine .....	68
Figure 48: Time moving FFT for a pressure monitor point between stator and rotor at 87% span, SAS turbulence model, steam model turbine.....	69
Figure 49: Time moving FFT for a pressure monitor point between stator and rotor at 87% span, SAS turbulence model, steam model turbine .....	70
Figure 50: Time moving FFT of an unsteady pressure signal of the steam model turbine recorded at 87% span between rotor and stator, steam model turbine.....	70
Figure 51: Zoom-in: Time moving FFT of an unsteady pressure signal of the steam model turbine recorded at 87% span between rotor and stator, steam model turbine .....	71
Figure 52: Unsteady traverse measurement plane 61 (between stator and rotor), steam model turbine .....	72

Figure 53: Flow coefficient versus fractional speed and pressure amplitude at the casing between stator and rotor plane 61, low frequency stall pattern, steam model turbine.....	73
Figure 54: Flow coefficient versus fractional speed and pressure amplitude at the casing between stator and rotor plane 61, high frequency stall pattern, steam model turbine.....	73
Figure 55: Unsteady traverse measurement plane 61 (between stator and rotor), steam model turbine .....	74
Figure 56: Flow coefficient versus fractional speed and pressure amplitude at the casing between stator and rotor, air model turbine .....	74
Figure 57: Unsteady traverse measurement plane 61 (between stator and rotor), CFD SST turbulence model, steam model turbine .....	75
Figure 58: Unsteady traverse measurement plane 61 (between stator and rotor), CFD SAS turbulence model, steam model turbine .....	76
Figure 59: Flow coefficient versus tip gap size and pressure amplitude at the casing between stator and rotor plane 61, steam model turbine .....	76
Figure 60: Different exhaust configurations for the steam model turbine .....	77
Figure 61: Time moving FFT for an unsteady pressure monitor point (between stator and rotor), CFD SAS turbulence model, no LSMB tip gap, steam model turbine.....	78
Figure 62: Unsteady pressure signal at the casing between stator and rotor, plane 61, measurement, steam model turbine .....	78
Figure 63: Circumferential velocity downstream of the LSMB, plane 62,CFD time averaged, steam model turbine .....	79
Figure 64: Left: Unsteady pressure distribution (CFD) on the blade surface caused by seven stall cells; right, instantaneous blade-to-blade view illustrating the separation region and pressure variation from the time average, CFD SAS model, steam model turbine (profile geometry is indicative for confidentiality reasons) .....	80
Figure 65: Corresponding phase to Figure 64 with a 0.6 mbar threshold, CFD, SAS model, steam model turbine .....	81
Figure 66: Meridional cuts at different theta positions, CFD SAS model, steam model turbine .....	83
Figure 67: Blade-to-blade view for different span heights, axial velocity contour, CFD SAS model, steam model turbine (profile geometry is indicative for confidentiality reasons) .....	84
Figure 68: Plane perpendicular to the machine axis at a 50% axial location between stator trailing edge and rotor leading edge, CFD SAS model, steam model turbine .....	82
Figure 69: 3D steam lines entering the rotor blade row at 75% span contour colouring of the streamlines is the relative circumferential velocity in the rotor domain, SAS model, steam model turbine .....	85
Figure 70: Plane perpendicular to the machine axis at a 50% axial location between stator trailing edge and rotor leading edge, CFD SAS model, air model turbine .....	93
Figure 71: Meridional cuts at different theta positions, CFD SAS model, air model turbine .	94
Figure 72: Blade-to-blade view for different span heights, axial velocity contour, CFD SAS model, air model turbine (profile geometry is indicative for confidentiality reasons).....	95
Figure 73: 3D steam lines entering the rotor blade row at 75% span contour colouring of the streamlines is the relative circumferential velocity in the rotor domain, SAS model, air model turbine.....	95

## Nomenclature

### Acronyms

3D	Three-dimensional
CFD	Computational Fluid Dynamics
CFL	Courant–Friedrichs–Lewy (number)
DNS	Direct Numerical Simulation
LSMB	Last Stage Moving Blade
LVF	Low Volume Flow
PS	Pressure Side (of a blade)
RANS	Reynolds Averaged Navier Stokes
RMS	Root Mean Square
SAS	Scale-Adaptive-Simulation
SS	Suction Side (of a blade)
SST	Shear Stress Transport (turbulence model)
URANS	Unsteady Reynolds Averaged Navier Stokes

### Latin symbols

$A$	Flow section surface [ $\text{m}^2$ ]
$a$	Speed of sound [ $\text{m/s}$ ]
$c$	Chord length [ $\text{m}$ ]
$c_p$	Isobaric heat capacity [ $\text{J}/(\text{kg K})$ ]
$f$	Frequency [ $\text{Hz}$ ]
$f_{red}$	Reduced frequency [ $\text{Hz}$ ]
$G$	Fractional speed $G = \omega_C / \omega_R$ [-]
$H$	Blade height [ $\text{m}$ ]
Span	Radial position relative to blade height $Span = (R - R_{Hub}) / H \cdot 100\%$ [%]
$\dot{m}$	Mass flow [ $\text{kg/s}$ ]
$Ma$	Isentropic Mach number [-]
$N$	Rotor speed [ $\text{Rev/min}$ ], Number of time samples [-]
$Re$	Reynolds number [-]
$St$	Strouhal number [-]
$k$	Scaling factor [-]
$p$	Static pressure [ $\text{mbar}$ ]
$p_t$	Total pressure [ $\text{mbar}$ ]

$T$	Static temperature [K]
$T_t$	Total temperature [K]
$Ta$	Taylor number [-]
$y^+$	Dimensionless wall distance [-]
$t$	Time [s]
$U$	Circumferential velocity [m/s]
$u, v, w$	Velocity components [m/s]
$\vec{v}$	Velocity vector [m/s]
$v$	Scalar velocity [m/s]
$x, y, z$	Cartesian coordinates [m]
$Z$	Blade count [-]

#### Greek symbols

$\alpha$	Flow angle with respect to the axial direction [°]
$\Delta$	Delta, difference between to neighbouring numerical values
$\delta$	Boundary layer thickness [m]
$\phi$	Flow coefficient [-]
$\kappa$	Isentropic exponent [-]
$\omega$	Angular velocity [rad/s]
$\Pi_{12}$	Pressure ratio $p_2 / p_1$
$\rho$	Density [kg/m <sup>3</sup> ]
$\mu$	Dynamic viscosity [Pa s]
$\mu_a$	Stage load [-]
$\nu$	Kinematic viscosity $\nu = \mu / \rho$ [m <sup>2</sup> /s]

#### Subscripts

1	Inlet flow plane
2	Outlet flow plane
BL	Boundary layer
C	Referring to stall cell
CP	Control plane
Max	Maximum of the quantity within the flow field
Norm	Normalised
Hub	Position at the inner boundary or hub of the flow path
Inlet	Referring to the inlet of the domain

LE	Leading edge (of a blade)
TE	Trailing edge (of a blade)
Model	Referring to the model turbine
Original	Referring to the real turbine
R	Rotor
RS	Rotating stall
S	Stator

# 1. Introduction

Power generation across the world is undergoing a rapid change. Developing countries are drastically increasing their electrical power generation capacity to meet their high energy demand. Simultaneously, the carbon dioxide emissions from power generation have to be reduced to mitigate the risk of global climate change. In addition, the majority of the conventional power generation is associated with the consumption of natural resources and therefore not sustainable. This has led to a strong growth in renewable and localised power production, which is expected to address these problems. This diversification of power generation methods has increased the requirement for operational flexibility of steam turbines in power production. Renewable energy sources cannot provide a continuous and reliable power production as their output is often difficult to predict and storage capacity is not available in the required quantities. This results in large variations of the power demand from conventional power production. In addition, steam turbines are also employed in renewable power generation, for example concentrated solar power plants or geothermal power plants. In particular, concentrated solar power plants demand a high flexibility from their steam turbines due to seasonal variations or daily starts and shutdowns, if no thermal storage or co-firing is used. Finally, steam turbines are increasingly expected to operate in regions without sufficient water-cooling such as desert regions. Air-cooled power plants experience a larger variation of the cooling water temperature, which consequently leads to a large change in steam turbine condenser pressure.

Why are an increased number of start-ups and shut-downs, operation under house load, varying power demand or operation with a poor condenser vacuum a challenge for existing steam turbine technology? Figure 1 illustrates a typical steam turbine configuration in a conventional power plant. Due to the large pressure drop through the turbine from up to 250 bar to near vacuum many turbine stages are required. Additionally, the turbine is divided into different modules to cope with the different pressure levels and keep the free shaft length in limits. The critical components in terms of flexible operation are those enduring high temperature and high pressure such as the inlet valves or the rotor of the high and intermediate turbine, which can suffer from low cycle fatigue under high thermal transients. Other vulnerable parts are the last stage moving blades (LSMBs) of the low-pressure (LP) turbine, see Figure 1 (circled in red). The length of these blades is maximized to increase the exhaust area. This is done to reduce the kinetic energy in the steam leaving the last stage. A longer LSMB can also be used to reduce the number of LP flows maintaining a similar leaving loss. The LSMBs are highly stressed by the centrifugal force. Due to their relatively slender form, they can be subject to vibration caused by the surrounding flow. The research presented will focus on this part of the steam turbine investigating possible sources of blade vibrations caused by the steam flow under flexible or rather off-design conditions.

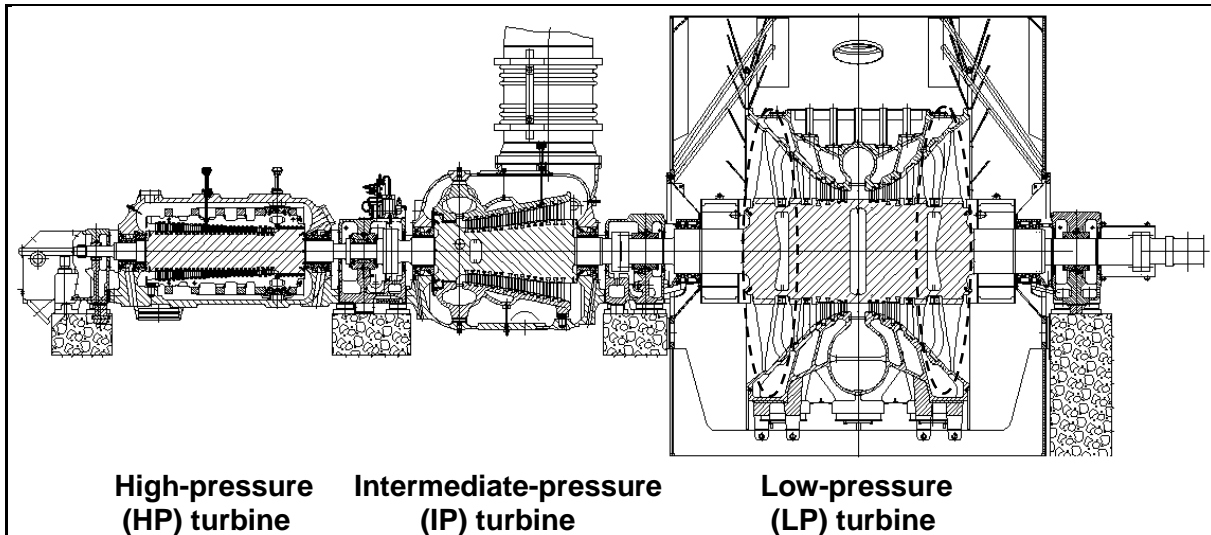


Figure 1: Typical steam turbine train of a conventional coal fired power plant, indicated with dashed circles: Last Stage Moving Blades (LSMBs)

The operating regime of the LSMB is characterised by the volume flow leaving the stage. The volume flow can vary due to a reduction in inlet mass flow to the stage under low load conditions of the power plant, or with large extraction mass flows for district heating, or steam used for chemical processes. As discussed earlier, a poor condenser pressure can also lead to a reduced volume flow as the fluid density is rising while maintaining the mass flow. Figure 2 shows the general characteristic of a turbine stage if the volume flow is varied. The stage load is the non-dimensional work output of a turbine stage. With a reduction in volume flow the work output is reduced and consequently the power output. At typically around 20% to 30% of the design volume flow, depending on the actual turbine geometry the stage is no longer producing power. A further reduction in volume flow leads to a power consumption of the stage, where energy is returned from the shaft to the fluid. This region is sometimes called ventilation region because the rotor blade is swirling in the globally slow moving fluid with small pressure differences. In this report, the term Low Volume Flow (LVF) operation is used.

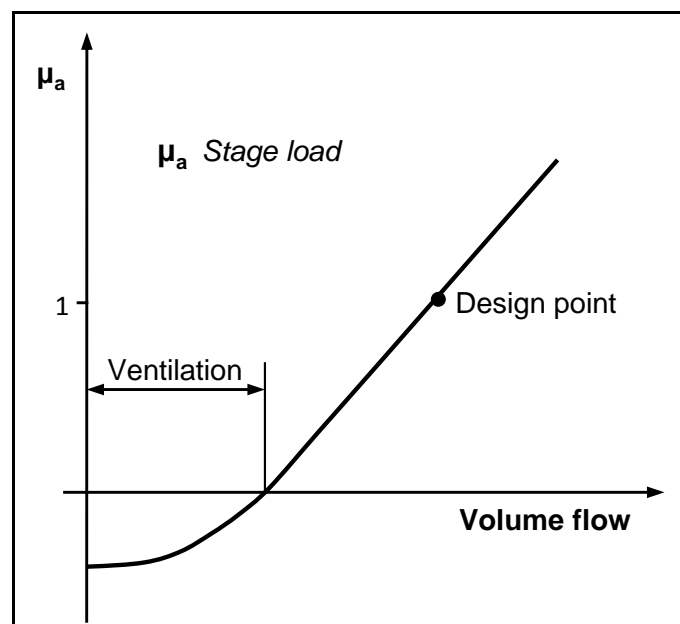


Figure 2: General characteristic of a turbine stage over flow coefficient

It has been observed that under LVF, LSMBs can suffer from high blade vibration. These vibrations are often induced by rotating aerodynamic instabilities similar to rotating stall in compressors. Currently extensive validation of new blade designs is required to clarify whether they are subject to the risk of not admissible blade vibration. Such tests are usually performed at the end of a new LSMB development project. If the excitation mechanism causes resonance to occur, a costly redesign is required, which may also lead to a reduction in turbine efficiency. It is also unclear whether older blade designs may suffer from this problem in future if they have not been tested extensively under these operating conditions. Although plants may have operated safely over a long period of time new flexible operating regimes as previously described, could result in blade damage. It is therefore of great interest to be able to predict the unsteady flow phenomena and their effects correctly.

In the present research, different methods have been used to investigate the unsteady aerodynamic flow phenomena described. Detailed unsteady pressure measurements have been performed in a single stage model steam turbine operated with air under LVF conditions. Numerical simulation has been applied to the unsteady flow in the air model turbine. It has been shown that the simulation reproduces the characteristics of the phenomena observed in the tests well. This methodology has been also applied to a more realistic steam turbine multi stage model. The numerical results have been validated against measurement data from a multi stage model LP steam turbine operated with steam. Measurement and numerical simulation show good agreement with respect to the global flow field, the number of stall cells and the intensity of the rotating excitation mechanism.



## **2. Literature review**

The following section will discuss the current understanding of aerodynamics and vibration behaviour of LP steam turbines operating under low volume flow conditions. To the author's knowledge, the aerodynamic blade excitation mechanism under LVF is not yet fully understood. The second part of the literature review will therefore address various known unsteady effects in turbomachines. This will help to categorize the observed phenomenon and draw conclusions about its physical nature. Furthermore, up until the preparation of this work no other analysis has been achieved with the same level of agreement with measurement. Guidance for the numerical modelling used here has thus far been derived from the modelling of more commonly studied problems such as rotating stall in compressors.

### **2.1 Low pressure steam turbines under low volume flow**

Fundamental research into the flow field under LVF conditions has been undertaken by Troyanovskii [1], Lagun et al. [2] and Shnee et al. [3]. The research was mainly driven by the extensive usage of extraction steam turbines for district heating in the former Soviet Union in the 1970's. A number of LSMB failures occurred during the operation under steam extraction with very low volume flows passing through the last turbine stage. Due to the highly complex nature of the flow field under ventilation, most of the research in the past has been performed using either model turbines or measurements in power plants.

#### **2.1.1 Time averaged flow field**

Troyanovskii describes how the flow structure changes with a reduction in volume flow. A typical spanwise variation of reaction common for a LP steam turbine last stage is 15% at the hub increasing to 65% at the tip at design conditions. The low reaction sections at the root of the rotor blade are the first to be affected by a reduction in volume flow. As the steam can no longer pass through the zone close to the root, it is redirected towards the tip and hence, a separation region develops behind the rotor blade. Lagun et al. [2] analyzed the ventilation behaviour with a single stage air turbine, which was driven by an electric motor. They stated that parts of the rotor blade operate as a compressor. As well as the hub separation zone behind the rotor blade, another separation zone establishes itself at even lower volumetric flows close to the casing in the axial gap between stator and rotor blade. This torus vortex moves in a circumferential direction with a considerable velocity, which is close to the rotational velocity of the rotor blade. The two separation zones and the centrifugal force guide the flow through the rotor blade into a diagonal direction with a dominant radial velocity component, as shown in Figure 3. With a further reduction in volume flow, the penultimate stage also starts to ventilate experiencing a similar separation pattern.

A number of measurements were conducted in recent years confirming the findings previously described. Major differences are the onset and the size of separation, during the reduction of volume flow. Both are highly dependent on the individual turbine design. A rule of thumb says that the first characteristic changes of the flow field appear below approximately 50% of the rated volume flow, see Teufelberger [4].

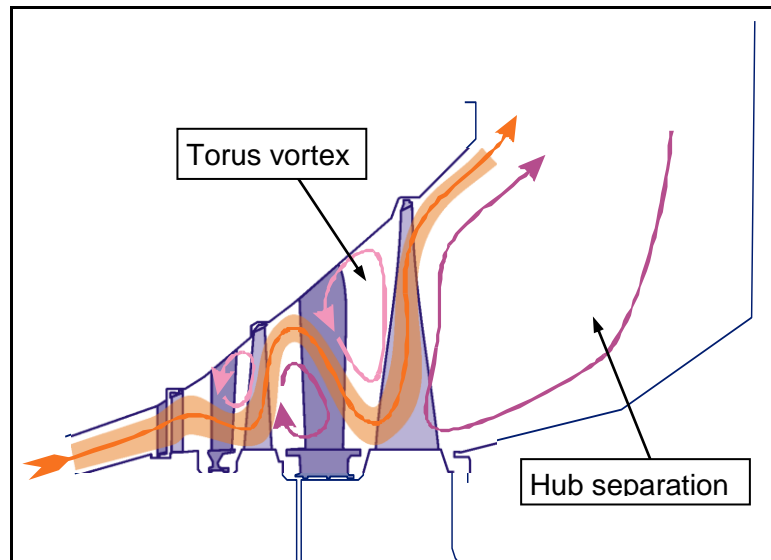


Figure 3: Characteristic meridional flow field of a LP steam turbine under low volume flow operation

### 2.1.2 Blade excitation

The most commonly understood excitation in turbomachinery under any operating regime is synchronous excitation due to circumferential symmetry imperfections, blade passing effects etc. Since natural frequencies can be predicted quite well, LSMBs are designed to be free from resonance from rotational frequency harmonics up to between the fifth and tenth engine order (multiple of the rotating frequency).

By contrast, resonance from non-synchronous excitation is more difficult to predict and therefore more difficult to avoid. Such excitation can be present over a wide frequency range. For example, rotating stall known from compressors can cause various excitation frequencies depending on the number of stall cells, their relative speed and the turbine rotational speed. Although excitation forces may be small, in the case of resonance high dynamic blade stresses may result where damping is low. Furthermore, aero-elastic instability may occur if the blade vibration is amplified by the resulting unsteady flow field. This phenomenon is known as flutter or stall-flutter.

Increased dynamic loading in LP steam turbines under ventilation has been reported frequently. Troyanovskii et al. [1] state that the reverse transient flows lead to additional dynamic stresses under ventilation, which can result in blade fractures. Shnee et al. [5] recorded an occurrence of increased dynamic stresses at part load even when the LSMBs are not subject to resonance from synchronous excitation. In the rig test conducted, the blades were monitored with strain gauges. While operating under low volume flow, the stresses sharply increased with values 2-3 times higher than the dynamic stresses at rated conditions. The rise in stress seems to be associated with the change from turbine operational mode to a compressor type operational mode where pressure and flow velocity is increased in the LSMB tip region.

In the literature reviewed, differing statements are made about the operating conditions with the highest dynamic blade loading. Engelke et al. [6] measured the minimum alternating

stress in a model steam turbine close to the point where the last stage produces zero power. If the volume flow is further reduced, the dynamic stress rises steadily until the maximum is reached at zero flow. The excitation is described as random, exciting various vibration modes without exceeding the allowable limits for alternating stresses.

In contrast to the Engelke et al. findings the vast majority of authors located the maximum dynamic stress under ventilation between the zero last stage work condition and operation with zero flow, see [6]. Gloger et al. [7] highlighted, that the volume flow leaving the stage is the parameter characterising the flow field in the last stages of a LP turbine. The alternating blade stress was influenced by the flow coefficient and is roughly proportional to the stage backpressure, or rather the steam density. The blade stimulus increased until it reached a maximum at 30% of the zero work volume flow where the last stage power output is zero, see Figure 4. When the flow is reduced to zero the excitation reduces again to lower values.

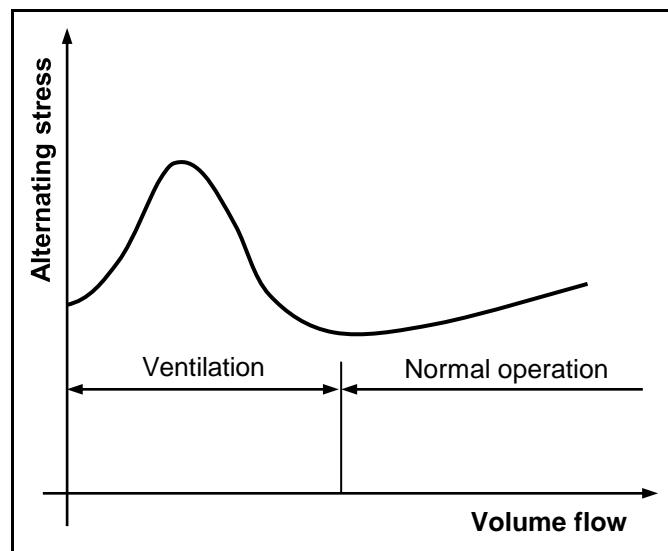


Figure 4: Schematic of alternating stress over flow coefficient for a case with non-synchronous excitation, see [7]

It is certain that there is an increased vibration level operating under ventilation conditions. However, the mechanism causing the excitation is unclear. Kondakov et al. [8] and Gloger et al. [7] found the excitation as random, exciting all natural frequencies of the LSMB. Kondakov et al. also mentioned that the excitation level varies sizably with time. A source of excitation could be the separation zone at the hub or the one at the casing between stator and rotor. At the tip of the LSMB, the high angle of attack could cause a separation phenomenon leading to excitation. Gloger et al. [7] describe different possible mechanisms and state whether they are likely or not. As the most probable candidate the unsteady conditions of the reverse flow is mentioned. A second possibility is buffeting known as a compression shock-boundary layer interaction. To allow buffeting the Mach number needs to be between 0.9 and 1.2, which is only the case in a certain operating range of LP turbines. LSMBs developed in the late 1960s have not shown any buffeting effects. It was also not possible to identify any excitation caused by condensing shocks. A third possible cause is rotating stall, which is a well-known phenomenon in compressors occurring shortly before the surge limit. Although the tip section of the LSMB operates as a compressor under ventilation, Gloger et al. saw it as unlikely that rotating stall is present in LP steam turbines. They state that the flow through the rotor blade is much too radial and has a small axial component. Furthermore, the compressor effect is mainly caused by the forces accelerating the fluid from hub to tip.

### 2.1.3 Unsteady flow field

The blade excitation only gives an indirect indication of the unsteadiness of the flow, as unsteadiness may be present without causing blade excitation. Shnee et al. [5] therefore used unsteady pressure probes to analyse the flow field by traversing upstream and downstream of the LSMB in a test turbine. They recorded a slight decrease in pressure fluctuation as the through flow was reduced to the zero work point of the last stage. The fluctuations reached a maximum between the zero work point and zero flow. The maximum coincided with the point where the compressor effect was highest. A further decrease in volume flow either decreased the fluctuations or did not affect them. Inside the turbine, the fluctuations were at a minimum in the separation zone behind the rotor blade adjacent to the hub. This was explained by the low energy of the separation zone. The level of disturbances was highest at the lower boundary of the torus vortex close to the casing. The amplitude was found to be 16% of the pressure drop in the stage under rated conditions. The investigation also revealed that the disturbance contained a harmonic, which was not a multiple of the rotational frequency. Shnee et al. point out, that such a disturbance can cause failure of the rotor blade where it coincides with a natural frequency.

Besides unsteady pressure probe traverses; different researchers also used unsteady pressure sensors on the casing in front of, above and behind the LSMB to detect pressure fluctuations. Stetter et al. [9] detected a rotating pressure disturbance in a model LP steam turbine. The transducer downstream of the rotor blade recorded the excitation mechanism as rotating at around half the rotor speed, in the direction of rotation. Schmidt et al. [10] used a four stage air turbine with blading similar to LPs. Non-synchronous pressure fluctuations were present in a critical volume flow range of 10% to 25%. The signals from the angular shifted probes above the LSMB were interpreted as four to five pressure cells moving around the wheel with approximately half the rotor speed. The fluctuations appeared in a stochastic manner with an intermittent stability. The fluctuations were clearly associated with the last stage, which was demonstrated by upstream pressure transducers. According to Schmidt et al., the phenomenon has similarity to rotating stall as it is present in the operating region of highest pressure rise across the LSMB tip.

By comparing the mechanical blade excitation and the pressure fluctuation under ventilation the fundamental question arises as to whether the blade vibration is caused by the fluctuation or if they influence each other. In other words, is the nature of the blade vibrations an aero-elastic stability problem, or are the blades excited by a flow inherent instability such as rotating stall? A first attempt to analyse the stability of LP steam turbine blades was made by Pigott et al. [11]. The large negative incidence angles as they are found in the tip region of LSMBs under low volume flow are likely to stall the flow around the aerofoil. Below a critical angle of attack, Pigott expected stall flutter to occur. An analytical investigation was carried out with a mechanical blade model and aerodynamic forces from measurements. Pigott claimed to detect self-excitation between 5% and 24% of the rated volume flow. Unfortunately, the stability is highly dependent on the mechanical damping, of which the modelling and measurement is afflicted by significant uncertainty. Kostyuk [12] uses a similar analytical approach. He also finds instability in a narrow range of volume flows. Queune and He [13] investigated separation-related blade aero-elasticity instabilities. An artificial tip separation was generated by a casing step in a linear cascade. The unsteady pressure in the separation zone had a destabilizing effect. Queune and He state that both stall flutter and large scale separation pattern such as rotating stall could exist at the same time and show a lock-in effect.

In contrast to stall flutter, there is clear evidence that a rotating excitation mechanism is present in different model LP steam turbines operating under ventilation without necessarily causing blade vibration, see [10, 14, 15]. Furthermore, if the blades are excited, conclusions can be drawn on the nature of the mechanism based on the circumferential mechanical

wave propagation in the LSMB assembly. Usachev et al. [16] monitored blade vibration for different LP turbines by the use of tip timing. They found a low frequency disturbance, which was rotating at about 40% of the rotor speed. Due to the intensity of the forward and backward travelling waves around the rotor, it was demonstrated that the excitation is not stationary relative to the blade, thus excluding flutter as the mechanism. Schmidt et al. [10] excluded a flutter mechanism for the pulsations they found in a model air turbine, as the rotor blade stiffness was far too high for an aero-elastic instability.

Some of the most recent published measurements of a LP model steam turbine under ventilation were conducted by Truckenmüller [15] and Gerschütz [14]. Two designs have been tested, which are scaled from LP turbines with  $10\text{m}^2$  and  $12.5\text{m}^2$  exhaust areas respectively. The turbines had three stages and freestanding LSMBs. Steady and unsteady pressure probe traversing was performed in the  $10\text{m}^2$  scale model. Unsteady pressure probe traversing and two unsteady pressure sensors in the casing above the LSMB, which were circumferentially shifted, have been used to investigate rotating excitation mechanisms in the  $12.5\text{m}^2$  scale model. An unsteady pressure probe traversing in the axial gap between stator and rotor of the  $10\text{m}^2$  scale revealed high activity between 80% and 100% relative span. As well as a high underlying noise level, discrete frequency peaks were visible. With the circumferentially shifted probes it was demonstrated, that each peak belonged to a specific number of pressure cells travelling around the wheel. The constant spacing between the peaks in the frequency domain indicated a constant fractional speed of each pattern relative to the wheel of roughly half the rotor speed. It was shown that only one pattern existed at any one instant in time. The presence of a pattern is stochastic with a preference for a number of cells indicated by the highest pressure amplitude. The phenomenon excited the second natural frequency of the LSMB in a relative volume flow band between 13% and 14%. A pattern with eight cells coincided with the second natural frequency of the freestanding LSMB. The dynamic blade stressing was still below the fatigue limit, but six times higher than without the phenomenon. Gerschütz investigated the  $12.5\text{m}^2$  scale model turbine in more detail to understand the nature of the fluctuations. The phenomenon was also present in this turbine, but with a significantly higher frequency level, which led to negligible excitation of higher order modes. Furthermore, the fluctuations were in a smaller fraction of the channel height between 96% and 100% span. The  $12.5\text{m}^2$  scale model had the same rotational frequency and LSMB count as the  $10\text{m}^2$  scale model. The frequency difference was suspected to be associated with the more modern blade design although details are not given about what the differences were. Gerschütz performed a number of variations in the thermodynamic boundary conditions and the geometry of the  $12.5\text{m}^2$  scale to investigate the effect on the fluctuations. A variation of the inlet temperature led to a significant change of the frequency and amplitude. An increase of 60K increased the frequency by 75 Hz while the pressure amplitude was decreasing. An increase in rotational speed also had an effect by increasing the frequency, amplitude and static pressure rise across the LSMB tip. By contrast, an increased condenser pressure whilst maintaining the volume flow had nearly no effect on the frequency whereas the amplitude increased proportionally. This shows a weak dependency on the Reynolds number. Finally, the radial LSMB clearance was increased with exchangeable rig casings. The largest clearance led to a frequency increase of about 300Hz as well as an amplification of the unsteady pressure fluctuations. Gerschütz also discusses possible mechanisms for the fluctuations. He points out that the phenomenon has a number of similarities to rotating instabilities such as those found in compressors and fans. The strong dependency of the fluctuations to the radial clearance has been observed in different experiments with axial fans and compressors. The mechanism is also found to initiate rotating stall in compressors.

It is likely that Gerschütz [14] found a mechanism similar to the rotating instabilities in the  $12.5\text{m}^2$  scale turbine under ventilation conditions. However, the frequency of the fluctuations was significantly lower as it would be expected from the fan and compressor experience. The  $10\text{m}^2$  scale had even lower frequency levels. Furthermore, the larger radial extent of the

fluctuation casts doubt on the theory of tip leakage flow related instability. Nevertheless, the tip leakage flow could still play an important role in initiating and influencing the rotating excitation mechanism.

#### 2.1.4 Numerical investigations

The highly complex flow field under ventilation is challenging for experimental measurement. This is also true for a numerical investigation. The first attempts were made to predict the flow field using a meridional flow solver by Petrovic and Riess [17]. Experimental calibration factors were needed to predict the onset of separation. Furthermore, the analysis was limited to a minimum relative mass flow of 20%.

Herzog et al. [18] applied steady state CFD-simulations to a four stage model air turbine. The 3D-Navier-Stokes Solver was used with a Spalart-Allmaras one-equation turbulence model. Regarding the complexity of the flow, good agreement was found with the global turbine parameters as they were measured. Larger discrepancies were found in the temperature distribution at very low volume flows. The major difficulty was the convergence of the CFD-calculations. Only with careful initialization was it possible to obtain converged results.

Sigg et al. [19] analysed a LP model steam turbine with steady state 3D-CFD. A fine mesh with a  $y^+$  around 1 on the blade surface was used in combination with a k-epsilon turbulence model. The fluid properties were described with an equilibrium steam model. The model was seen as sufficient as only small wetness levels were identified. The results were compared with measurements from a test rig. Global parameters such as the total power as well as local phenomena such as the pressure rise over the LSMB tip were predicted reasonably well.

It has been observed through measurement that the flow field under ventilation has an inherent unsteadiness. Steady state CFD is therefore a coarse approximation of the real flow field. With computational power increasing, unsteady CFD is becoming a more viable method to analyse transient flow behaviour. A first attempt to simulate the pressure fluctuations in LP steam turbines under LVF has been made by Zhang et al. [20]. Although the flow field has a dominant radial flow component, a 2D blade-to-blade approach has been used to reduce the computational effort. In a subsequent study a 3D model has been used extending over a limited number of passages with an adapted blade count to achieve pitch matching at the stage interface, see Zhang et al. [21]. Periodic symmetry conditions have been applied at the interfaces of the flow domain. No direct comparison is shown with unsteady measurement results, but it is stated that a 20 pressure cell rotating instability is observed, opposite to the 8 to 10 cells found in the test results of Truckenmüller [15]. This is most likely linked to the fact that the model has not covered the full annulus constraining the unsteady effects.

Low-frequency non-synchronous pressure fluctuations such as rotating stall or rotating instabilities cannot be investigated using single passage CFD models as they have been used so far, as the nature of the phenomenon is not bladed wise circumferentially periodic. Different researchers have used full annulus models to investigate compressor or fan instabilities, see for example Vahdati et al. [22]. In open literature, no reports have been found up to now where such a CFD approach has been applied to LP steam turbines under low volume flow operation conditions.

## 2.2 Unsteady effects in turbomachines

The unsteady flow effect observed in LP steam turbines under low volume flow may be either categorized into one of the known unsteady effects in turbomachinery or represents a new unsteady effect. For such a judgment, generally accepted unsteady effects found in turbomachinery, are briefly introduced and compared with the state of the art knowledge of the unsteady effects in LP steam turbines under low volume flow.

### 2.2.1 Turbulence

The following main characteristics of turbulent flow are given by Rotta [23]. Turbulent flow is irregular with velocity variations depending on location and time. A single measurement does therefore not deliver an exactly repeatable result. The result is in other words stochastic. Furthermore, turbulent flow is an unsteady eddy flow and three dimensional. For example, the Von Kármán vortex street behind cylinder is a vortex flow, but regular and coherent and therefore not a turbulence phenomenon. As turbulent flow is not free of rotation, the viscosity of a fluid is of great importance. The occurrence of turbulence is typical for flows with a high Reynolds number:

$$Re = \frac{vl\rho}{\eta}$$

with  $v$  being a characteristic flow velocity,  $l$  a characteristic length,  $\rho$  the fluid density and  $\eta$  the dynamic viscosity. If the Reynolds number is below a critical value, damping friction forces prevent turbulent movement, [23]. The flow is then referred to as laminar.

Turbulence usually has a characteristic range of frequencies and energy. As larger vortex structures break up into smaller scales or respectively higher frequencies, the spectrum of turbulence is also named as energy cascade, see Figure 5. Large vortex structures are influenced by the domain boundaries and the global flow field. If large scale turbulence exists it is often difficult to distinguish turbulence from coherent structures, Hussian [24]. Coherent structures are defined as “a connected fluid mass with instantaneous phase-correlated vorticity over a spatial extent”, see Hussian [24]. Vortices, which contain the highest amount of kinetic energy, are described by the Taylor scale. In the inertial range, the vortex breakup can be described by inertial effects and viscous effects are negligible. The very small vortices contain a low amount of overall energy but contribute the most to the dissipation. The smallest turbulent vortices are defined by the Kolmogorov micro scale.

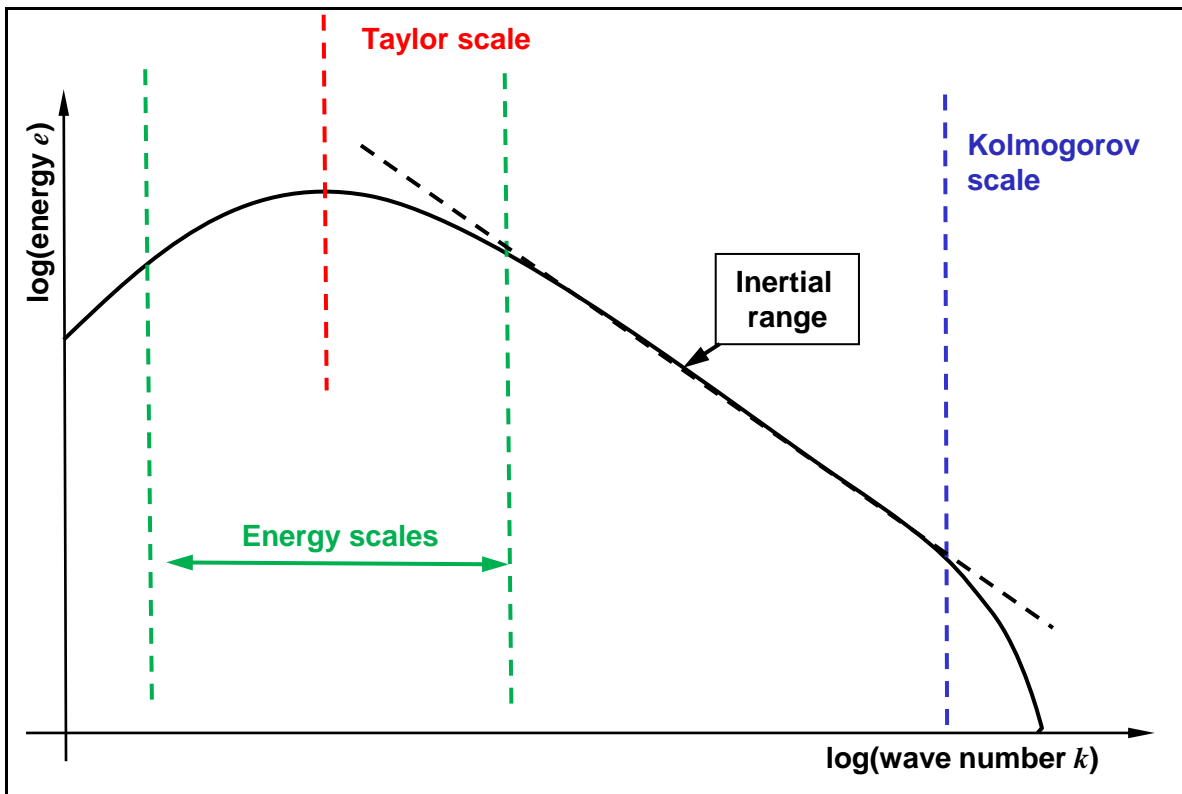


Figure 5: Energy content of the different turbulence scales

In the case of LP steam turbines under low volume flow, various types of turbulent flow can be expected. Relatively high levels of free stream turbulence are likely to enter the last stage. This is because upstream stages may already operate with large separations. The level of free stream turbulence has an impact on the stability of boundary and shear layers. Respectively, high free stream turbulence induces earlier along a boundary layer length the laminar-turbulent transition. The typically relatively small turbulence scales found in the boundary layer are of importance for the level of skin friction and the tendency to separation due to adverse pressure gradients. A major source of turbulent fluctuations and therefore unsteadiness is the highly separated and vortical flow. Shear layers between the separated and through flow are likely to generate a range of turbulent scales. Clearly some of these random pressure fluctuations will excite the natural frequencies of LSMB to a certain degree. As described earlier the kinetic energy of turbulent fluctuations is distributed over a range of frequencies. This means relatively small forces are acting onto the LSMB at the critical resonance frequencies. These forces depend also linearly on the fluid density. General blade vibration levels are therefore expected to rise gradually with an increase of condenser pressure at a fixed volume flow where the structure of the separation zones is maintained. Blade excitation caused by turbulent fluctuations is therefore directly correlated with the unsteady fluid force. As described, the amount of unsteady forcing is relatively low at low back-pressures. Secondly, the level of vibration can be limited by introducing a limit for the condenser pressure based on validation and experience.

The discrete dynamic pressure frequencies observed in LP steam turbines are clearly not a turbulent flow phenomenon, as they are not distributed stochastically in terms of their energy and frequency scale. Nevertheless, increased levels of turbulence are reported if such type of unsteadiness occurs. There may be also interaction between turbulence and the rotating pressure fluctuations.



### 2.2.2 Rotor stator interaction and vortex shedding

Due to the presence of stator and rotor blades, unsteady flow perturbations are observed both in the stationary and rotating frame of reference. Harmonics of the stator disturbance as well as interactions between stator and rotor disturbances can excite the rotor blade. Kubota et al. [25] pose a check whether modes of the rotor can be excited or not with the equation

$$hZ_R \pm N = qZ_S$$

where  $h$  and  $q$  are positive integers,  $Z_R$  and  $Z_S$  are the number of rotor and stator blades, and  $N$  is the excited nodal diameter. The nodal diameter mode is a fixed pattern of vibration rotating in the same or opposite direction of the rotor. The direction is given by the sign of  $N$  to satisfy the equation, a positive value means a forward travelling wave, and a negative one, a backward travelling wave. If the equation is satisfied, the value of  $q$  represents which harmonic of the rotor blade passing frequency is excited. Secondly, the harmonic of the blade passing frequency needs to coincide with a natural frequency of the rotor blades. Although many integer combinations fulfil the equation above for a steam turbine LSMB, blade vibration due to rotor stator interaction appears to be unlikely due to its high frequency. Typical last stage blade counts are relatively high to limit the rotor length and individual blade weight, which reduces the rotor imbalance in case of a LSMB failure. Therefore, possible excitation frequencies are relatively high. On the other hand, the natural frequencies of LSMBs are relatively low due to their slender form. In addition, the first set of natural frequencies are carefully tuned to be out of resonance with the engine order excitations. It is also not clear why LVF operation should increase possible vibration due to rotor stator interaction. The blade loading is significantly lower under these conditions and so is the resulting potential pressure field and wake of the stator blade row.

Vortex shedding is present if the flow detaches periodically from the back of a body forming a Von Kármán vortex street. Such a flow situation can occur on the trailing edge of a blade profile. The resulting frequency can be estimated using the Strouhal number. The trailing edge size is usually minimized to reduce the trailing edge loss. Consequently, the shedding frequency is high compared to the blade natural frequency. Under LVF, the flow is expected to separate from the blade surface over a substantial distance of chord. A periodically separating pattern is resulting at significantly lower frequencies, which could excite the LSMB. The inflow to the rotor blade row is nearly tangential, this means a potential formation of vortices would possibly interact with the neighbouring passages. A periodic separation pattern is a plausible cause for the observed unsteadiness. This could allow to derive a characteristic Strouhal number or explain effects such as that the excitation frequency is close to independent from the Reynolds number over a wide range, see Gerschütz [14].

### 2.2.3 Flutter

Flutter is an aero-elastic instability, which is found in many types of turbomachinery and can lead to blade failure. Initially small motions of the blade change the surrounding flow field in such a way that the unsteady fluid forces acting on the blade are amplifying the vibration. A basic parameter to check whether flutter is likely to occur is the reduced frequency

$$f_{red} = \frac{2\pi fc/2}{v}$$

where  $f$  is the vibration frequency,  $c$  the chord length and  $v$  a mean velocity from inlet to the outlet of the blade section. The reduced frequency is the ratio of the time for a blade vibration cycle compared to the time a fluid particle needs to pass from inlet to the outlet. Flutter can occur below a critical value of reduced frequency. Most steam turbine LSMBs are

subjected to this risk. It can be controlled with an appropriate blade design, sufficient structural damping and blade mistuning. In addition, the operating range is limited to a maximum mass flow. This is done because the unsteady pressure forces acting on the blade scale linearly with the fluid density. The structural damping is expected to be constant over the operating range at constant rotor speed. This means if a LSMB is aerodynamically unstable sufficient mechanical damping will only prevent blade vibration up to a certain density limit or in other words mass flow. The critical region for flutter is therefore typically the higher mass flow region. Under LVF operation the mass flow is usually very low, however high density levels can be achieved if the condenser pressure is increased. This poses two questions: is the separated flow field leading to an unstable situation and are the fluid forces high enough to overcome the structural damping? As discussed earlier, He [26] provided evidence that a separated flow field can be destabilizing. It is therefore likely that flutter occurs under LVF if the condenser pressure is increased to high levels. Only little information is available on LVF flutter. This phenomenon has to be clearly distinguished from the rotating pressure fluctuations found in many LP steam turbines. These pressure fluctuations are also present without blade vibration and therefore are not an aero-elastic phenomenon.

#### 2.2.4 Surge and rotating stall

A characteristic feature of the operating map of radial and axial compressors is the stability or stall line. This line determines at which combination of pressure ratio and reduced mass flow the compressor operation becomes unstable. Compressors transport fluid from a low pressure to a high pressure volume continuously. If the system is overloaded, fluid can flow back from the high pressure region to the low pressure inlet. As the pressure ratio is then reduced, the compressor can move back to normal operation until the stability line is reached again. This effect is commonly termed surge or surge cycle. It can be treated as a one dimensional global mass flow fluctuation where the inlet piping, throttle or valve and outlet chamber need to be taken into account, see Greitzer [27].

Before an axial compressor enters the surge cycle, other local instabilities can appear. Close to the stability line, individual compressor stages are highly loaded. The flow in individual passages can separate due to small disturbances. The actual initiation of the stalling is an active field of research. Different mechanisms are described such as rotating instabilities related to the tip leakage flow, model waves and spikes, see Mailach et al. [28], Day [29] and Camp [30]. If the flow separates in one passage, this has also effect on the inlet flow angle to the passage and consequently on the neighbouring passage. This can lead to stalling of the neighbouring passage because the angle of attack is increased, see Figure 6. The stall cell then propagates in a direction from the pressure side to the suction side of the profile tangentially or for a rotor blade row against the direction of rotation in the reference frame of rotor rotation.

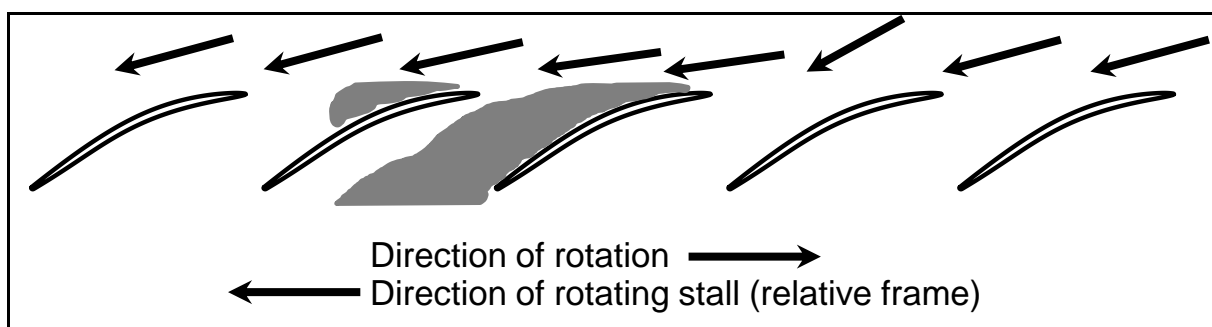


Figure 6: Rotating stall mechanism in axial compressors

This phenomenon known as rotating stall can, once initiated, develop rapidly into different types of rotating stall and finally surge. First, the stalled region is confined to a small span section of the passage. It can then grow to a full-span rotating stall blocking the whole passage and also neighbouring passages simultaneously, see Day et al. [29]. In some cases, there are multiple large full-span stall cells typically with a low number of individual cells. In compressors with slender blades, the local disturbance can develop into smaller part-span stall cells close to the casing for the rotor or close to the hub for the stator. The part span stall cells propagate generally at higher speeds against the rotor rotation than the full-span cells, see Day [29] and Inoue et al. [31], with fractional speeds ranging between 50% and 80%. The part span stall can feature many individual stall cells and develops after a certain period into full span rotating stall.

There are similarities between axial compressor rotating stall and the phenomenon observed in LP steam turbines under LVF. The closest analogy is found with part span rotating stall. However, there remain distinct differences: in a steam turbine the flow is already highly separated before entering the unstable region which allows the separation zones to readjust if the diffusion becomes too high. The insufficient flow and compression makes surge impossible. The same is true for full-span rotating stall. In addition, the way rotating stall is treated is different between compressor world and LP steam turbines. A steam turbine has to be capable to operate in the unstable region. In contrast to compressors, the problem is not to determine the stability line but the magnitude and frequency of the unsteady force. From a design point of view a simple and effective design tool is needed to demonstrate that a compressor is free of stall as Vahdati et al. [22] point out. For LP steam turbines the allowable operating range cannot be restricted in the same way since this would seriously limit the operation flexibility of the power plant. It is therefore of second order interest to predict the stability line.

Rotating stall can be found in radial compressors too, although here the stall cell propagation mechanism is less obvious than for the axial compressor. Rotating stall can occur in both the impeller and the stationary diffuser depending on the impeller speed, see Kämmer and Rautenberg [32]. Only limited information is known on the inception of the rotating stall in radial compressors, see Ljevar [33]. Single and multiple stall cells can exist and rotate at a fraction of the rotor speed or even be stationary, [32]. Typically, two types of diffusers are used in radial compressors. Diffusers including vanes offer a superior performance in a narrow operating range, whereas vaneless diffusers are efficient over a wide operating range. Interestingly, rotating stall does also occur in vaneless diffusers where no blade-to-blade propagation mechanism is possible. The term “stall” as normally referred to as a large separation from a profile, if the critical angle of attack is exceeded, does not apply. However, if the inflow to the vaneless diffuser becomes nearly tangential multiple pressure cells can appear and rotate at a fraction of the impeller speed.

Lejevar [34] showed that the Taylor–Couette instability could be a plausible explanation for rotating stall in a vane less radial diffuser. This hydrodynamic instability can occur in the gap between two rotating cylinders and is also named centrifugal instability, see Drazin [35]. The flow in the cylindrical void is initially steady in the rotating frame but subjected to a centrifugal force due to the rotation. If the centrifugal force becomes too high, a secondary vortex flow develops similar to the Rayleigh–Bénard convection. The Taylor number represents the ratio between the tangential forcing and the viscous friction force

$$Ta = \frac{\omega^2 r_m d_0^3}{\nu^2}$$

where  $\omega$  is the angular velocity of the cylinders,  $r_m$  is the average radius,  $d_0$  the distance between the inner cylinder and the outer cylinder and  $\nu$  is the kinematic viscosity. Above a critical Taylor number instability occurs.

Under LVF operation in steam turbines, highly tangential flow is present between stator and rotor close to the casing. A more complex flow instability could occur forming a system of cells around the circumference rotating at a certain velocity. The number of stall cells should than be determined by the outer boundaries of the flow domain. In addition, the phenomenon would exist in a laminar flow situation, too. Unfortunately, this is difficult to prove, as turbulent flow is difficult to avoid in turbomachinery. A test case with a very low speed rotor could lead to such a situation, as flow velocities are low, but this will also lead to low tangential velocity and therefore no instability to occur.

### 2.2.5 Concluding remarks on known unsteady effects

Phenomenological, rotating stall has the most similarities to the rotating pressure fluctuations observed in LP steam turbines under low volume flow. Already Lagun et al. [2] have pointed out that parts of the LSMB of LP steam turbines under low volume flow (LVF) operation act similar to a compressor. Figure 7 illustrates the LSMB tip pressure ratio while reducing volume flow. As the volume flow is reduced, the operational mode moves from expansion to compression. With a further reduction, a peak pressure rise is obtained. According to Gerschütz, Schmidt et al. and Truckenmüller [10, 14, 15] this is also the region with highest flow unsteadiness, see Figure 7. A pressure rise over the tip is therefore a precondition for the phenomenon to occur.

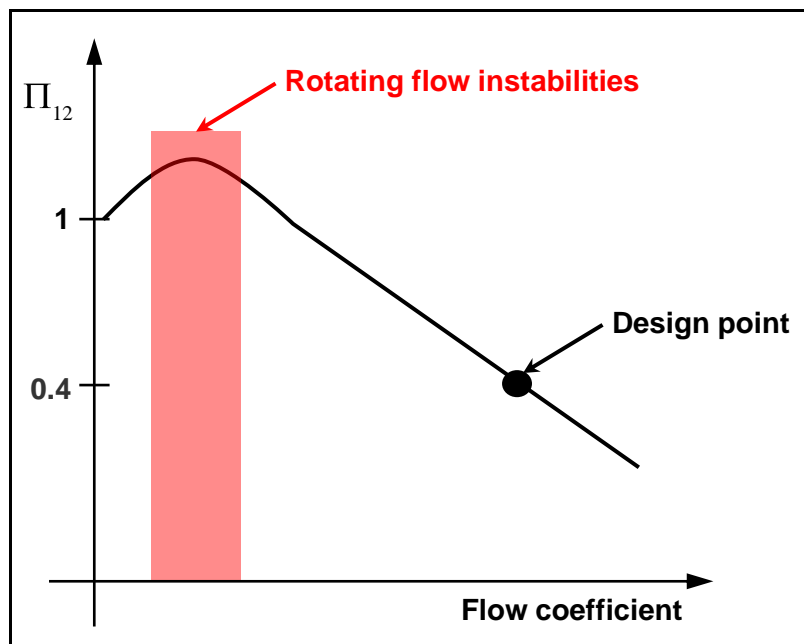


Figure 7: LSMB tip pressure ratio as a function of volume flow

The unsteadiness also features discrete frequencies, which can be associated to multiple pressure cells travelling around the wheel at a fraction of the rotor speed. These cells are most prominent at the casing, which is in line with the part-span rotating stall situation. It is not an aero-elastic phenomenon and can therefore occur without structural blade vibration motion. A deeper insight to the actual mechanism driving the phenomenon is not given in literature. To highlight the nature of the flow phenomenon and for simplicity reasons, the term rotating stall will be used in the following chapters.

### 3. Measurement and modelling methods

The research involved using both measurement and numerical methods. The measurement campaigns have been conducted in the ALSTOM turbine testing facility. Measurement results are required to develop and validate a reliable numerical approach. The detailed results of the numerical investigation are then used to gain an in depth understanding of the rotating stall phenomenon.

#### 3.1 Measurement methods

Data from two different test rigs have been obtained. One model turbine is operated with air, whereas the second model is using steam as the working fluid. Results of the model air turbine have already been available prior to this research project. The steam model results have been specified and obtained during the research project. A brief comparison of the two test rigs is given in Table 1. The air model is a simplified model of a real steam turbine, which allows many measurements and rapid changes of the geometry and of the measurement equipment. In contrast, the steam model turbine is representing the full size turbine as closely as possible including important features of the full size turbine such as multiple stages and a realistic exhaust geometry. Illustrations of the blade profiles and three dimensional blade shape can be found in Figure 68 and 69 for the steam model and Figure 72 and 73 for the air model.

Table 1: Comparison of turbine models

	Full size steam turbine	Steam model	Air model
Scale and geometry $k$	1:1	1/3 Upstream stages present	1/10 Single stage model
Full scale exhaust area $A$		~7 m <sup>2</sup>	~14 m <sup>2</sup>
Stator blades		54	50
Rotor blades		67	90
LSMB design		modern blade with integral snubber, tip sections optimised for transonic flow	conventional blade design with lacing wire
Hub to tip ratio LSMB		~0.45	~0.47
Fluid	Steam	Steam	Air
Exhaust pressure level $p$	~100 mbar	~100 mbar	1000 mbar

	Full size steam turbine	Steam model	Air model
<b>Mach number</b> <i>Ma</i>		Similarity achieved	Considerably lower than the full size steam turbine
<b>Shaft speed</b>	Typically 3000 rpm or 3600 rpm	9000 rpm	4000 rpm
<b>Flow coefficient</b> $\phi$		Full range of volumetric flow is covered	Limited range, but covering dynamic effects
<b>Reynolds number</b> <i>Re</i>	$\sim 9 \cdot 10^4$ (dependent on operating conditions)	$\sim 3 \cdot 10^4$ (dependent on operating conditions)	$\sim 2.7 \cdot 10^4$

### 3.1.1 Similarity

An important aspect to judge the results of a model turbine test is the comparability between the model and the full-scale turbine. Similarity is achieved if the relevant non-dimensional flow quantities are kept constant as well as the geometry has a sufficient similarity with the full-scale fluid device.

For steam turbines, the respective model turbines are typically chosen to be significantly smaller than the real machine. This is mainly linked to economic and operational reasons. The turbine geometry is scaled by a scaling factor

$$k = \frac{l_{Model}}{l_{Original}},$$

where  $l$  is any length of the geometry.

To maintain the identical velocity triangles, the rotor rotational speed

$$N_{Model} = \frac{1}{k} N_{Original}$$

is often increased by the inverse of the scaling factor. The preferred medium for LP steam turbines is steam to have matching fluid properties under condensing conditions. Again, for practicality and cost reasons, some model turbines are operated with other fluid such as air. In this case, some other similarity parameters are not maintained.

The Mach number

$$Ma = \frac{c}{a}$$

describes the compressibility effect of the fluid. The similarity is for example maintained if a correct speed scaling is given and the local speed of sound is unchanged due to the same medium and temperature level. If a similarity in flow velocity is not kept, the Mach number may be maintained with an appropriately chosen fluid. Compressibility effects are likely to be relevant under ventilation because of the high velocity of the LSMB tip, which leads to high relative velocities. Yet, tests in the air model turbine with low Mach numbers have shown that the rotating stall phenomenon is also present in a close to incompressible flow conditions. This leads to the conclusion that compressibility may influence the rotating stall, but is not the driving physical factor.

Due to the reduced characteristic length  $l$  in the model turbine, the Reynolds number

$$Re = \frac{cl\rho}{\eta}$$

cannot be maintained, with  $c$  being a characteristic flow velocity, hence no Reynolds similarity is achieved. However, various measurements in the model steam turbine have shown that the unsteady behaviour of the highly separated flow regime under ventilation conditions is not significantly dependent on the Reynolds number in the given case. This is also stated in open literature, see Gerschütz [36]. To achieve a variation of the Reynolds number tests have been performed at different pressure levels in the steam model turbine. The changed density leads then to a different Reynolds number by a factor of 2 to 3.

Another similarity parameter is the flow coefficient,

$$\phi = \frac{\dot{V}}{AU} = \frac{u}{U}$$

which describes the axial flow velocity  $u$  relative to the blade circumferential velocity  $U$ . Gloger et al. [7] highlighted, that the flow coefficient is the key parameter characterising the flow field in the last stages of a LP turbine. The flow coefficient correlates with the operating regime from where the ventilation region starts and the operating regime interval in which rotating stall occurs. It is therefore the most important similarity parameter for investigating the low flow behaviour of LP steam turbines.

As well as the thermodynamic and aerodynamic similarity, the vibration behaviour of the rotor blades is also of importance. Choosing the same blade material leads to change of the blade natural frequencies

$$f_{n, Model} = \frac{1}{k} f_{n, Original}$$

by the inverse of the scaling factor  $k$ , if correct speed scaling is applied. Although the blade is geometrically scaled correctly, deviations to the real turbine may occur due to the tolerances, which are not scaled. As discussed in the introduction, rotating stall does also occur without blade vibration. A correct mechanical modelling of the full size turbine is therefore not essential. Nevertheless, if resonance appears aero-elastic effects on the phenomenon can be investigated. On the other hand, it may be difficult to operate the test rig safely due to high blade vibration.

Possible sources of excitation do also change their frequency  $f_e$  along with the scaling factor which can be described using the example of the Strouhal number

$$St = \frac{f_e l}{v}.$$

Typically, the Strouhal number is constant for a range of Reynolds numbers for a specific geometry. With a reduction in characteristic length  $l$  the excitation frequency rises accordingly, if the flow velocity  $v$  is maintained. It can be concluded that with a correct speed scaling and consistent material choice resonance can be expected at similar operating regimes in the model turbine and in the full size turbine. The resulting blade vibration amplitude of the forced response is linked to the damping of the mechanical system. As well as the structural damping, which is given by the blade material, damping is also defined by the contact surfaces in the root attachment or blade couplings such as shrouds or snubbers. In addition different manufacturing tolerances, surface qualities and contact forces can lead to different damping. Blade vibration amplitudes from model turbines have therefore to be handled with care. Measurements of the full size steam turbine are needed to confirm the values gained in the model test.

### 3.1.2 Air model turbine

The air model turbine has been specifically constructed to investigate the unsteady flow phenomenon under ventilation. Figure 8 shows a cross-section from the approximately 1/10 scale model. The rig includes the last stage blading, together with the axial-radial diffuser. No upstream stages have been added to maintain simplicity. The inflow direction is therefore axial entering the rig from the left. The blade geometry is derived from a conventional full size design with around 14m<sup>2</sup> exhaust area with a rotating frequency of 50 Hz.

The rig is instrumented with four probe traversing locations allowing the measurement of the flow up and downstream of the rotor blade, Figure 8. Different pneumatic pressure probes can be inserted to measure the time averaged and unsteady flow field. In addition, the rotor blades are instrumented with strain gauges to monitor the blade vibration behaviour.



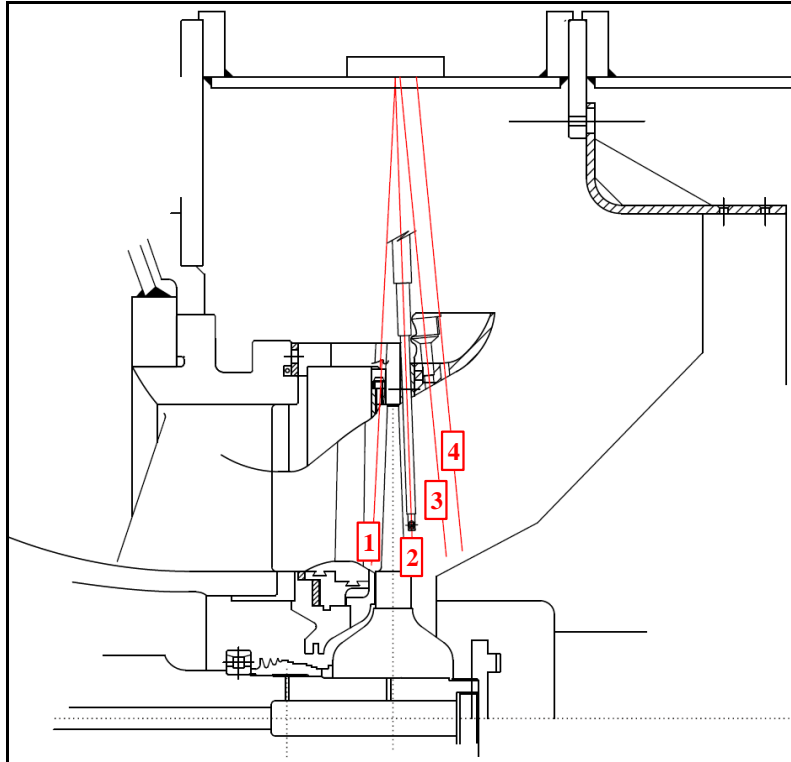


Figure 8: Meridional view of the air model turbine with traversing locations

To generate flow conditions similar to an LP steam turbine stage under ventilation, it was necessary to drive the turbine shaft. In the given case, the turbine shaft is driven with an electric motor. However, due to restrictions of the rig and the electric motor it was not possible to achieve a correct speed scaling, leading to lower rotor speeds. In combination with using air as the medium, strict Mach number scaling was not achieved. During consideration of these tests an alternative approach was found; that being to conduct the tests at a representative volumetric flow, while relaxing some of the more usual similarity parameters. The volumetric flow parameter  $\phi$  is defined here as the average axial flow velocity through the channel annulus area just downstream of the rotor blade trailing edge divided by the blade root tangential speed. Previous experience has indicated that rotating stall can be encountered in the range  $0.05 < \phi < 0.15$ . Working with the available equipment meant that the rig would operate at about one tenth of the correct speed scale. In combination with air as the medium in atmospheric conditions, peak Mach numbers of about 0.3 are present. This is much lower than in a typical LP steam turbine where transonic conditions are encountered. For this arrangement, a butterfly valve was placed upstream of a flow meter, followed by the model turbine. The exhaust from the turbine was open to atmosphere. The tests were started with the butterfly valve open. To achieve a range of volumetric flow, the butterfly valve was slowly closed, reducing the flow drawn through the turbine by the driven rotor. Most tests were conducted in this way, with the motor speed held constant throughout.

With the experimental setup it was found that a maximum  $\phi$  of just above 0.12 could be achieved. While this does not extend beyond the range of volumetric flow of interest, in this case it turned out that the full range with rotating stall had been covered. The spectrum from the dynamic pressure probe showed the characteristic series of equally spaced lines when plotted in the frequency domain, see Figure 9. The rotating stall cells were established, despite operating the rig considerably off conditions for the Mach number and pressure level. It was decided that the rig could be used to gain an understanding of the nature of the rotating events, with the proviso that the events might not be identical to those found in the full size machine operated with steam as the working fluid.

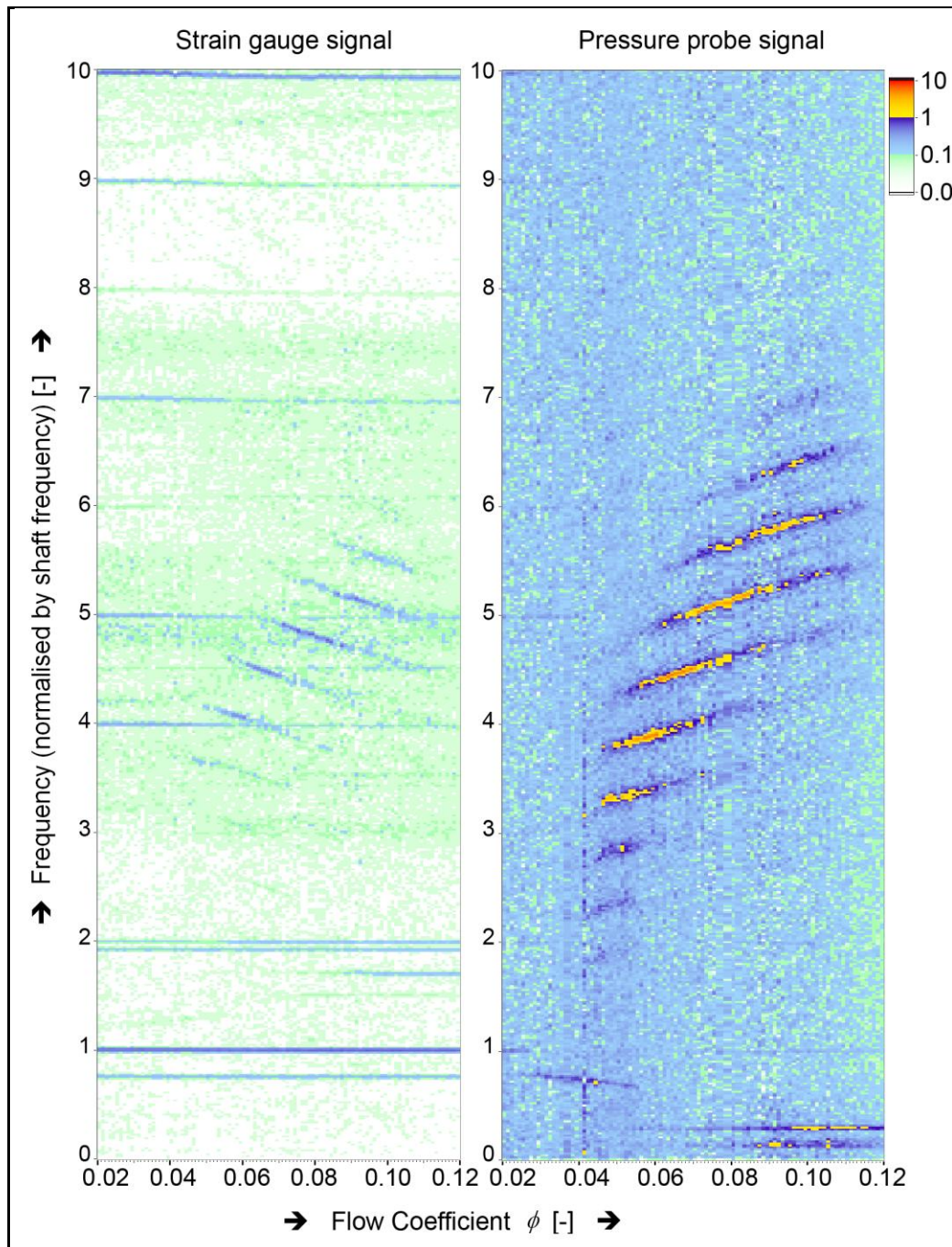


Figure 9: Carpet intensity plot recorded by the strain gauge (arbitrary contour scale) and the dynamic pressure probe (contour in [mbar] (RMS))

Two intensity charts are used to show the information from a rotating strain gauge and the stationary dynamic pressure probe, see Figure 9. The y-axis is a frequency scale (in this

case indicated by engine order), the x-axis is volumetric flow, and the amplitude found is indicated by colour level. The rotating stall unsteady pressure signal is most clearly seen in the pressure probe, where there is a trend towards lower cell numbers as the volumetric flow is decreased by closing the butterfly valve. The signals of the rotating stall cells is also identified as a forced vibration in the strain gauge signal, which because they are rotating, appear with a change of sign of gradient compared to the stationary signal. The number of cells can be cross-correlated by comparing the amplitude of the individual unsteady peaks and their corresponding peak as a forced vibration signal. This allows also the calculation of the fractional speed of the stall cell systems.

The frequency content measured from the pressure probe has shown a variety of cell counts, with the most dominant of these being identified as 8 stall cells on the wheel rotating at a fractional speed to the rotor of approximately  $0.5 \pm 0.03$ . This identification is conclusive because the associated forced vibrations can be seen in the rotating frame of reference, as measured by the rotating strain gauges. The asynchronous pressure events did not excite the natural frequencies of the LSMB allowing for a safe operation of the rig. Furthermore, the unsteady aerodynamic behaviour of the rotating stall cells is not influenced by blade vibration movement allowing an isolated observation. This is because the blade vibration amplitudes resulting from the off resonance forced response are very small.

It can be concluded that the air model turbine reproduces a rotating stall situation similar to the one found in LP steam turbines. It is therefore a valid tool to investigate the observed effects.

### **3.1.3 Steam model turbine**

The ALSTOM steam model turbine test facility is used to investigate various aspects of new last stage blade designs, McBean et al. [37]. The test turbine is designed to model the full-scale low pressure steam turbine as closely as possible. The steam is delivered by a neighbouring power plant and is then throttled to the required inlet conditions. The test turbine comprises multiple stages to model the correct inlet boundary conditions to the last stages. The split shaft design with a front and a rear rotor allows measuring the torque of individual stages or stage groups, see Figure 10. In the investigated setup, the front shaft comprises two stages and the rear shaft the two last stages. Each of the two shafts rotational speed can be controlled using a water brake. The rear shaft including the last and penultimate stage is additionally connected to a Curtis drive turbine. This is required to drive the turbine under ventilation conditions. In this way, the behaviour of the real steam turbine is modelled where the ventilating rear stages are driven by upstream turbine sections, which are still doing positive work on the shaft. The investigated blade geometry is a modern state of the art design scaled from a  $7\text{m}^2$  exhaust area 50Hz full-scale turbine.

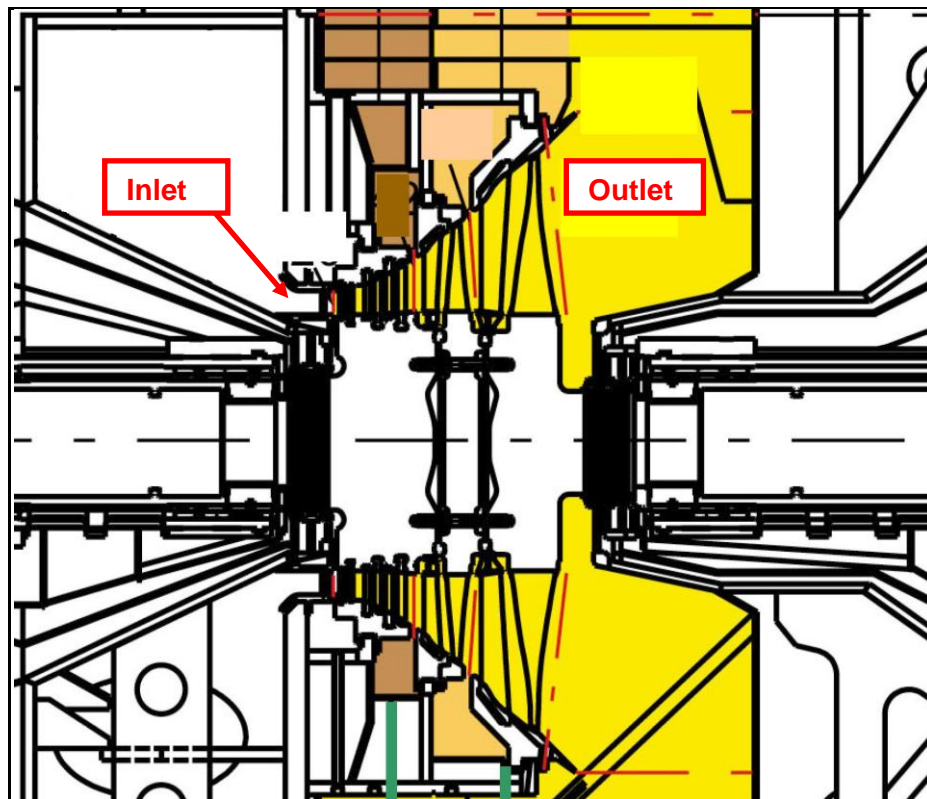


Figure 10: Cross-section of the steam model turbine, see [37]

As well as the bladed flow path itself, also the exhaust system is modelled in detail. In addition, the exhaust hood is modelled including all stiffening plates and struts, which are found in the full-scale turbine for mechanical reasons, see Figure 11. Unlike in most power plants the steam is directed in the exhaust box upwards. This is a unique feature, which allows an quicker assembly and disassembly of the test rig. No impact on the comparability to a real turbine is expected, as the gravity influence acting on the low-density steam is negligible.

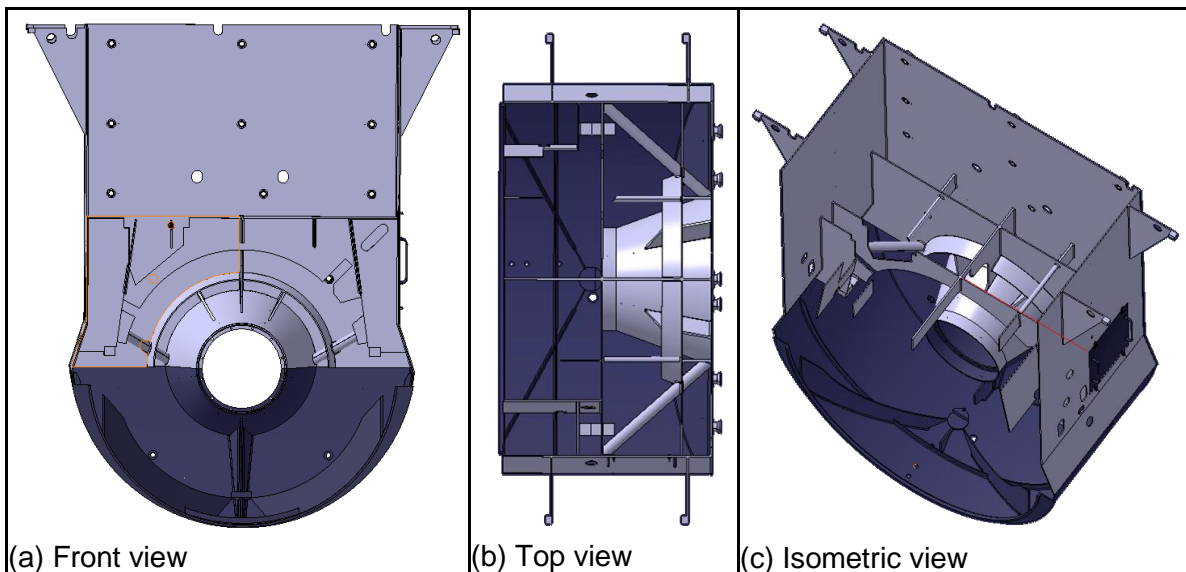


Figure 11: Exhaust hood of the investigated steam turbine model

Figure 12 illustrates some of the measurement locations of the steam model turbine. The instrumentation can either be conventional pneumatic measuring probes, or contain a dynamic pressure sensor. It is possible to traverse up and downstream of the rotor blade. The upstream probe can only be inserted 14% of span radially inwards due to limited space. The flow downstream of the rotor blade is highly circumferentially non-uniform because of the exhaust geometry. To capture these effects three traversing locations are placed around the circumference with a 120° enclosed angle, Figure 12 (b).

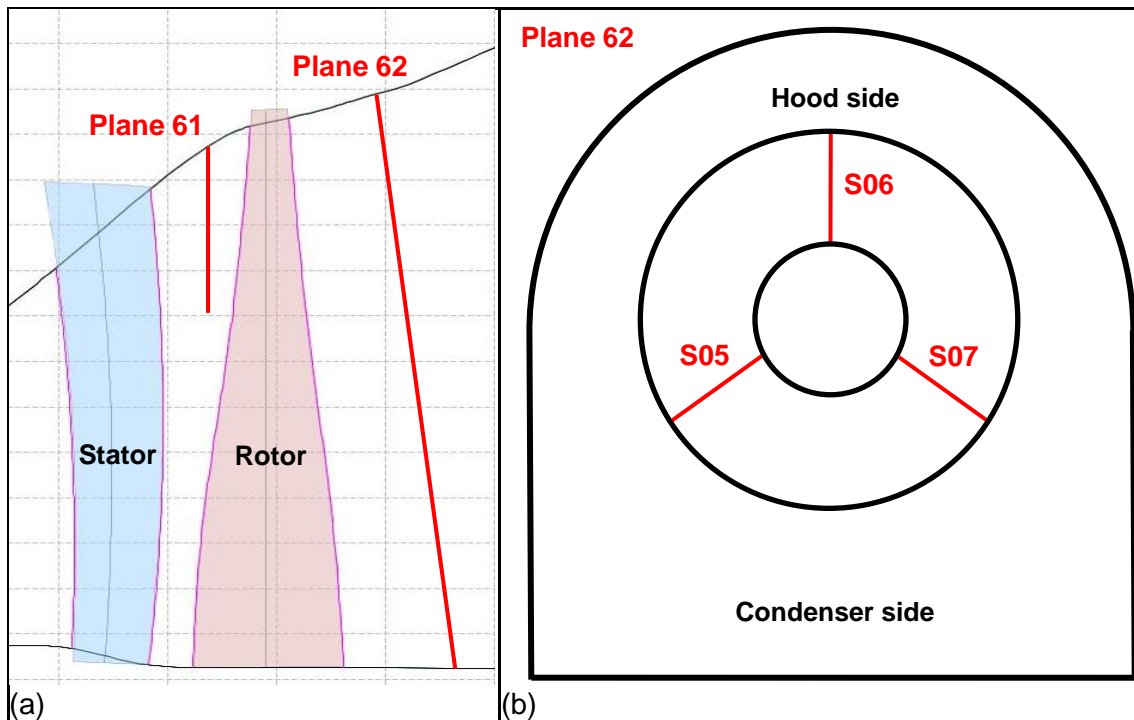


Figure 12: (a) Cross-sectional view of the steam model turbine rear stage, (b) Upstream view of plane 62, probe traverse locations marked in red



The rig also includes a strain gauge instrumentation of the LSMB. The measurement data is transferred via a slip ring system. Two strain gauge locations are equipped with a thermal couple to monitor the temperatures to calibrate the signals, see Figure 13. A large number of measurement systems and locations are installed in the rig, but they will not be described in further detail.

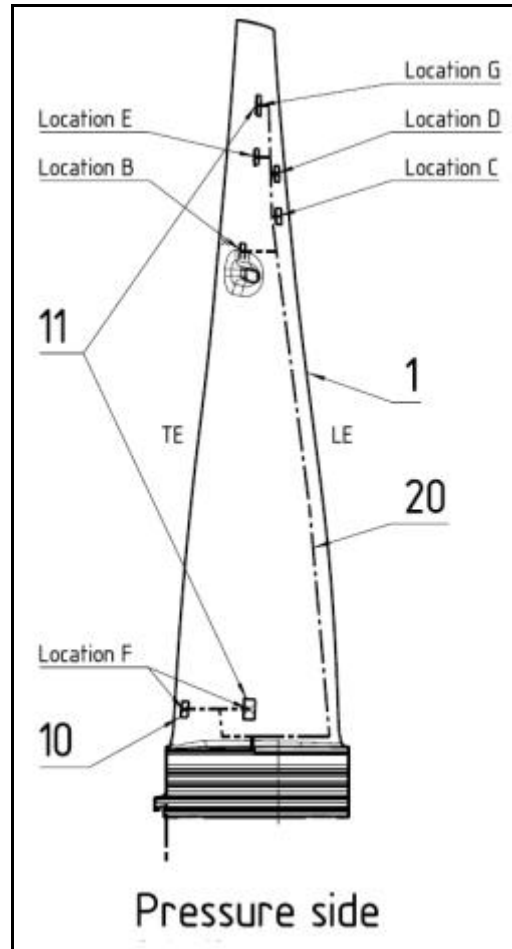


Figure 13: Strain gauge locations on the LSMB of the steam model turbine, location 11 thermal couples

As stated in Table 1, the steam model is a scaled version of the full-scale machine by a factor of approximately 1/3. For similarity of the velocity triangle, the rotor speed is increased by a factor of three with respect to the real machine. This enables Mach number similarity in combination with steam as medium with an equivalent inlet temperature. Compressibility effects are therefore correctly modelled. The Reynolds number is three times smaller than in the real turbine. This can lead to a changed flow separation behaviour, transition effects and pressure loss associated with skin friction. As previously stated, it has not been found for the given case that the unsteady flow behaviour is sensitive to the Reynolds number. This is illustrated by measurements at different pressure levels and measurement results from literature, see Gerschütz [36].

Unlike the air model, the steam model can cover a wide range of flow coefficients. Similar flow coefficients can be achieved at different pressure levels, by adapting inlet mass flow and condenser pressure combinations. This allows investigating additional dependencies such as on the fluid density or Reynolds number. As in many other low pressure steam turbines rotating stall is found between flow coefficients of approximately 0.05 to 0.15. Figure 14 illustrates a measurement result with dynamic pressure signals downstream of the LSMB in plane 62 at the casing and strain gauge data.

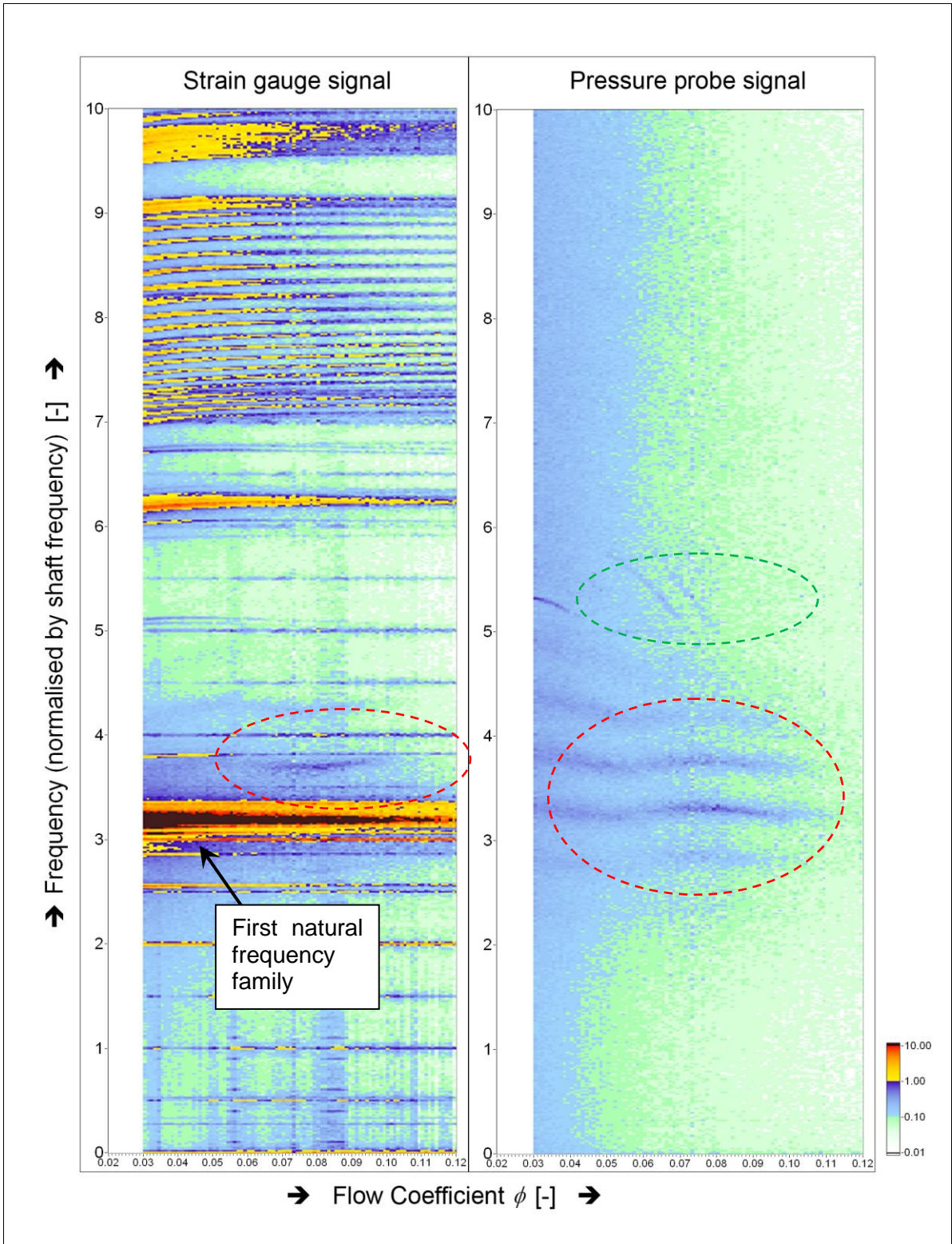


Figure 14: Measurement result from the steam model turbine, carpet intensity plot recorded by the strain gauge (arbitrary contour scale) and the dynamic pressure probe (contour in [mbar] (RMS))

Maintaining the inlet mass flow at a constant level the condenser pressure is gradually increased. Along with the resulting reduction of volume flow, a rotating stall cell system is appearing in both the unsteady pressure signal and the strain gauge signal. This allows again the identification of the number of cells and their fractional speed relative to the rotor speed. The steam model presents a more complex picture of rotating cells with lower cell numbers which having a relatively stable frequency with changing flow coefficient (circled in

red) and a system with higher cell numbers with a steep gradient against the flow coefficient (circled in green). The strain gauge signal is harder to read as it contains clear engine order signals and a response of the first natural frequency family close to the shadows of the stall cells (also circled in red). The higher cell numbers cannot be identified easily by eye, but can still be cross-correlated with an appropriate post-processing routine. The set of cells is not in resonance with a blade natural frequency, therefore there is low blade vibration over the operating range with a gradual increase towards higher backpressure due to the increased fluid density and turbulent fluctuations. With a change in rotor speed, the blade can be forced in resonance with a particular cell number. Additionally in this case, the vibration levels are acceptably low due to the relatively weak stall cells and the mechanically well damped LSMB. This means the stall cells can be investigated without the influence of the blade vibration motion. This is both advantageous for the safe rig operation and the numerical modelling. It has to be pointed out that under certain changed conditions high blade vibrations can occur. The setup has solely been chosen as the main aim is to investigate the unsteady flow physics and the accuracy of numerical frequency and pressure amplitude prediction. The aero-mechanical problem of the resonance situation is not studied here in further detail.

In summary in terms of non-dimensional similarity, the steam model is closest to a full-scale turbine. Similarities, which are not achieved, have shown to be not relevant for the observed phenomenon. A system of rotating stall cells is present which can be investigated and used for numerical validation.

### **3.1.4 Measurement techniques**

For a valid comparison of the results, the global test rig operating point has to be determined. The mass flow is measured with a Venturi flow meter in both rigs. The steam model is measured over a wide range of mass flows, however the accuracy of the flow measurement with small mass flows is poor using the same Venturi diaphragm opening. This problem is addressed by using a second flow measuring device. A water flow meter is used to quantify the amount of liquid water extracted from the condenser under stable operating conditions. This allows a considerably more precise mass flow measurement under low mass flow conditions.

The turbine inlet temperature is measured with a temperature rake just before the first stator row. The rotor speed is continuously measured with a sensor placed at the turbine shaft. This allows for a stable rotor speed and continuous rotor speed variations. The condenser pressure is measured at 4 wall mounted pressure tapping in a horizontal plane of the exhaust box. The low flow velocity under low volume flow conditions in the exhaust system leads to a relatively homogeneous static pressure field resulting in a precise measurement of the condenser static pressure using the wall conditions only.



The volume flow downstream of the LSMB (air model plane 2 and steam model plane 62) can be derived in different ways. The axial velocity in the control plane is directly measured with the traversing system. This has the disadvantage that information is only available in combination with traverse measurement at fixed operating points. Furthermore, large quantities of reverse flow present in the control plane are challenging both in terms of averaging to receive a 1D quantity and the ability of the five hole probes to measure highly radial flow. In addition, the velocity profile does also vary in tangential direction where only limited information is available. The approach which is seen as the most reliable and has been applied to both the measurement and numerical results is based on the conservation of mass. The axial exit velocity in the control plane is

$$u_{CP} = \frac{\dot{m}_{Inlet}}{A_{CP} \rho_{CP}}.$$

Obtaining the required quantities is straight forward for the air turbine where the mass flow is continuously measured and the density in the control plane is given by the density of air at atmospheric conditions expecting almost incompressible flow with Mach numbers in the control plane below 0.2. In the steam model turbine, highly accurate measurements of the mass flow can only be made under stable operating conditions. The thermodynamic state of the steam in the control plane has to be estimated based on temperature and pressure measurements. Fortunately, because of the ventilation power added to the fluid the steam thermodynamic state is clearly above the saturation line. This is removing the complication of measuring the wetness content. The continuously measured mass flow is much less accurate being based on venture flow meter readings. In addition, the estimation of the thermodynamic state is less accurate as a number of wall mounted pressure tap sensors are not recorded continuously. Continuous volume flow measurements in the steam model have therefore to be handled with care, whereas individual global measurements under stable operation are highly accurate.

The method to obtain the traverse measurements is described in the following two sections. It has to be pointed out that these measurements have been performed under stable global operating conditions. It has also been monitored in the steam model that the metal temperature of the casing is stabilized minimizing the thermal flux allowing the modelling of the turbine to be adiabatic at the flow boundaries.

#### **3.1.4.1 Time averaged flow measurements**

Although the focus of the presented research is the unsteady flow behaviour, a solid understanding of the time averaged flow field is required as it already presents a complex picture and gives indications on the effects observed in the time and frequency domain.

The highly separated flow field with a dominant radial flow component represents a challenge to the available measurement equipment. In the air model velocity components were measured with the 7 hole disc probe along 4 traverse lines, see Figure 15. This probe carries static pressure tapings on either side of the disc. The probe was rotated to achieve a balance of the side pressures, resulting in the probe being set parallel with the swirl angle. A series of pressure sensors, evenly spaced around the disc, were then measured. The maximum measured pressure, together with the two neighbouring measurements, was then processed through a calibration routine to give total Mach number and pitch angle. While this method is not as spatially accurate as the more conventional 5-hole probe, it has the advantage of a much higher acceptance angle. It is therefore more appropriate for the measurement of recirculating flows, where the likely approach angle is not known before the measurement. At each traverse location, the flow was measured at a series of radial positions. The overall view of the flow field was built up by combining the information from all four traverses.

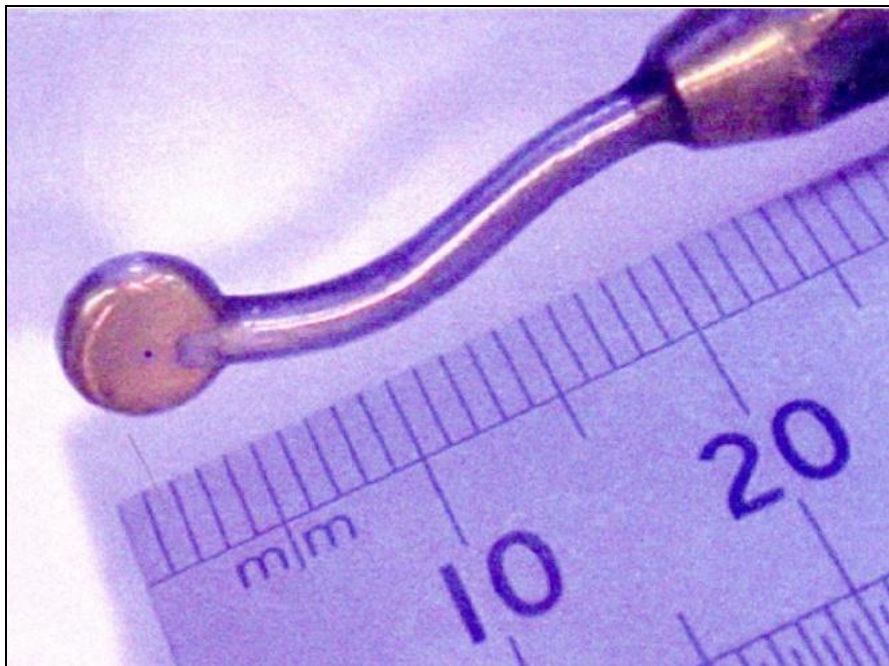


Figure 15: Seven hole disk probe head

In the steam model turbine a conventional five hole probe was available to measure the flow field downstream on the LSMB in three circumferential positions. Between stator and rotor, no readings are available because of the limited axial space. Although the spatial accuracy of the five hole probe is higher, regions with mainly radial flow cannot be measured accurately because of the pitch angle has been calibrated only in a range of  $\pm 40^\circ$ . This is linked to limitations of the steam calibration channel, where the five hole probe is calibrated up to Mach numbers of 0.9. The actual probe is inserted with an inclination of  $6.5^\circ$  reducing the negative pitch angle range to  $-33.5^\circ$ . Nevertheless, the probe has been employed as it gives reliable results over a certain span height, whereas readings with higher pitch angles can only be considered as indicative.

### 3.1.4.2 Unsteady flow measurements

Unsteady pressure signals in the stationary frame of reference were obtained from a traversing probe carrying a dynamic pressure sensor. The probe is inserted at the same locations as the five and seven hole probes for the time averaged measurement for the steam and air model turbine. In effect, measurements have to be performed sequentially requiring stable operating conditions. This miniature cylindrical sensor is mounted on the axis of the probe. The probe head features a small cylindrical cavity at the sensor tip, with one drilled hole to admit pressure to be measured. A Kiel type surround was included in this probe, to make it less sensitive to flow direction. Although the probe carries a miniaturized sensor, in terms of the model scale it is still a relatively intrusive device, particularly with regard to circumferential blockage in the axial clearance between stator and rotor in both the air and the steam turbine, see Figure 16.

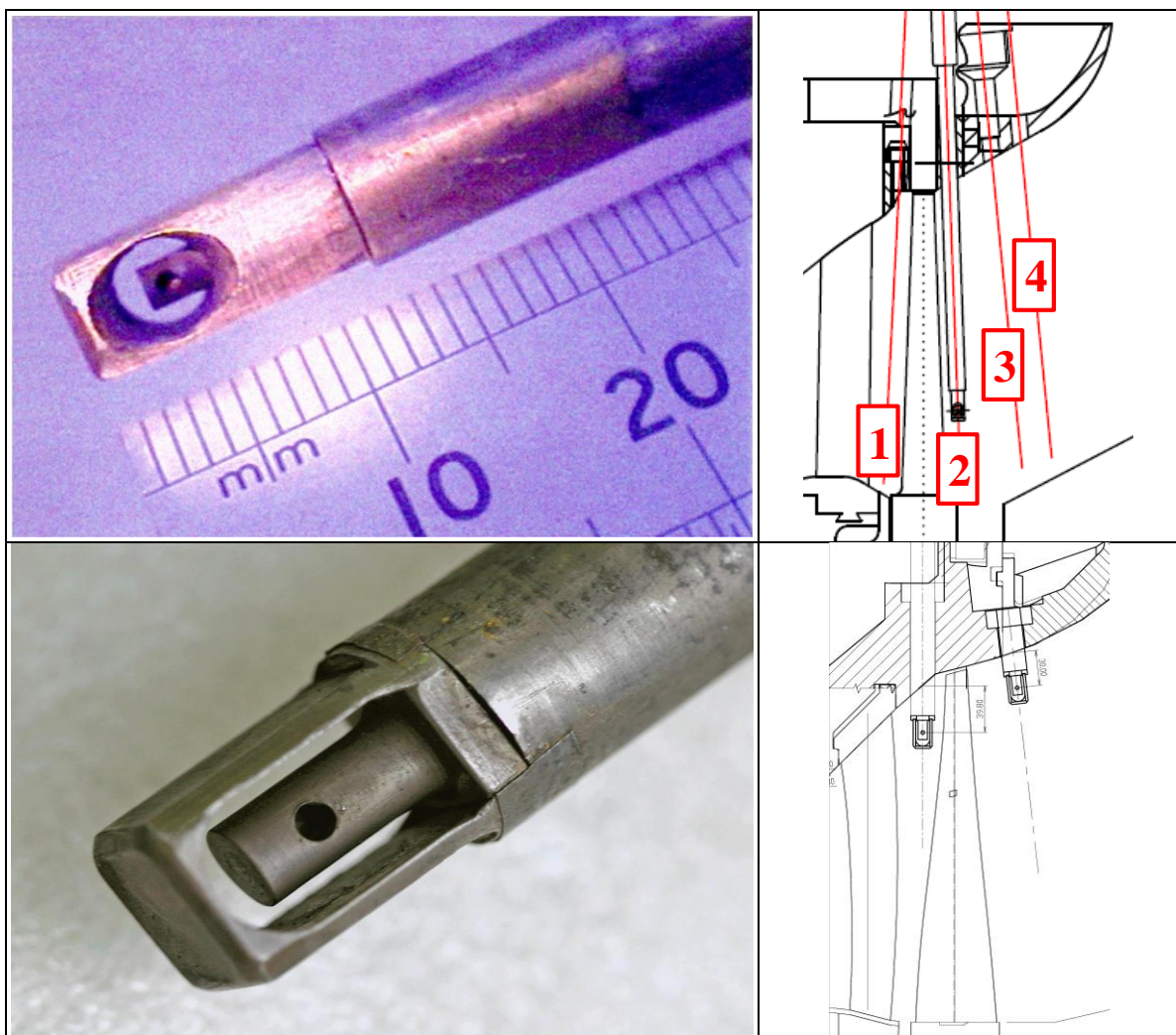


Figure 16: Kiel probe head, probes for the air model (top) and in the steam model (bottom)

The Kiel head arrangement is oriented to face into the flow direction. Accordingly, the probe is measuring total pressure fluctuations. In the case of low volume flow operation measurements, this means they are positioned to measure a flow which is predominantly circumferential.

The probe used in the air model is of a stepped design with the diameter of the probe decreasing towards the sensor. The main body of the probe has a 13 mm diameter. The

inner probe cylinder has a 6 mm diameter. The sensor used is an *Endevco 8507C2*, chosen to fit inside this 6 mm size. The volume of the drilling to the sensor was minimized in the design, in order to keep a high natural frequency for the probe. On its own, the sensor has a natural frequency of 60 kHz. For the probe, the volume of the cross drilling has a natural frequency of 20 kHz. In the work described, measurements are sometimes taken at 10 kHz, but more commonly at 5 kHz, with the frequencies of primary interest around 500 Hz. There is very little cause for temperature variations in the air rig. Fluid temperature changes are reduced because the speed at which the shaft is moved is quite modest, and the rig is operated in an open cycle, these factors mean that changes in room temperature during the day can be higher than temperature changes during operation. The sensor carries thermal compensation circuitry that delivers a linear voltage with pressure for a much wider temperature range than experienced with this model turbine configuration.

The steam model dynamic pressure probe has an outer tube size of 20mm and is utilising an *Endevco 8540C15* sensor, which is more suitable for the harsh steam environment, see Figure 16.

The analogue dynamic pressure signal is converted to a digital signal for recording and post-processing. The current hardware system uses a 24bit A2D converter, delivering a dynamic range with digital steps of 2.5  $\mu\text{V}$ . The clock rate of the conversion is checked against a reference signal generator.

Before the transformation to the frequency domain, the signal is preconditioned to obtain better results. The signals are subject to an anti-aliasing filter, which is a low pass filter. The position of this filter is dynamically positioned to be at 95% of the highest frequency to be analyzed. Due to the fact that the time signal is of finite length, a periodicity of the time sample cannot be guaranteed. This may lead to non-physical effects such as spillage, where additional amplitude appears in the wrong FFT frequency bin. Therefore a Hanning window

$$w(n) = \frac{1}{2} \left( 1 - \cos \left( \frac{2\pi n}{N-1} \right) \right)$$

is employed where  $N$  is the number of time samples. The window  $w$  is then multiplied with the time sample gradually fading the signal in and out reducing dependencies on the finite sample length. In the second step a Fast Fourier Transformation is applied to the time signal  $x$  with

$$X(k) = \sum_{j=1}^N x(j) \omega_N^{(j-1)(k-1)},$$

where

$$\omega_N = e^{(-2\pi i)/N}$$

is an  $N$ th root of unity and  $k$  the next power of 2 from above the length of  $x$ .

The process of Hanning windowing reduces the amplitude in the spectra, which need to be compensated by multiplying the resulting FFT amplitude by a factor of two. Additionally the spectrum is plotted as a root mean square (RMS), which is achieved by dividing the amplitudes with square root of two.

Because of the different fluid and size, a suitable normalisation of the unsteady pressure amplitude is required to compare the air and steam model results. The normalisation can also compensate differences in density due to different temperature levels, which can occur in the measurement and the CFD modelling of the steam model turbine. The following normalization has been applied:

$$p_{norm} = \frac{p}{\frac{1}{2} \rho_{Fluid} U_{Hub}^2},$$

where  $p$  is the measured amplitude,  $\rho_{Fluid}$  the fluid density and  $U_{Hub}$  the LSMB hub tangential speed. It is an interesting fact that the dynamic head used for the normalization is only 20% higher for the steam model as the change of density is counterbalanced by the change in blade speed. Due to the speed scaling, a real steam turbine would result in the same head as the steam model turbine.

### 3.1.4.3 Blade vibration measurements

For the air model, two strain gauges are fixed to the blade aerofoils near the blade root, on opposite blades to maintain the rotor balance. The signals are provided for assistance of the frequency analysis, and the semi-conductor gauges employed are not calibrated to deliver a known stress. In this turbine configuration, interesting forced response patterns are observed, but it is regarded as sufficient to know that these are vanishingly small compared to permissible dynamic stress - something that would be difficult to achieve at the modest shaft speeds possible with the motor used. The signals are delivered from the rotating frame of reference using telemetry. Transmitters are mounted on the disc locking ring, with the aerial located in the front of the diffuser cone.

The steam turbine model employs a more detailed vibration measurement as critical blade vibration levels can occur. A set of strain gauge locations is used to monitor different vibration mode shapes, see Figure 13. Ideally, the strain gauges are placed close to the location of maximum amplitude of the mode shape of interest. Amplification factors are calculated based on finite element analysis for each strain gauge allowing the measurement of the real amplitude and alternating stress. The strain gauge signal is transmitted from the rotating system using slip rings on the turbine shaft.

## 3.2 Numerical modelling

For the choice of an appropriate numerical method, a list of requirements has been noted based on the knowledge of the observed rotating stall phenomenon at the time. The main requirements were:

- 3D Navier-Stokes Solver
- Temporal integration of second order accuracy
- Sufficient validation (Solver results been extensively compared to measurements)
- Numerical convergence (Solver should converge for all reasonable defined cases)
- Numerical stability (Same set of relaxation factor and smoothing should be used for all cases and does not need calibration)
- State of the art turbulence models (Two equation eddy viscosity models)
- Ability to handle large 360° models (Efficient parallel implementation)
- Online monitoring and frequency analysis
- Anticipation of unknown requirements and future support

A number of ALSTOM in-house and commercial CFD codes have been assessed. In addition, it has been discussed, if the model size could be reduced by the use of a harmonic method. In this method, the unsteady content of the flow is treated in the frequency domain. Typically, only a single passage has to be used instead of an arc section or full annulus model. This can significantly reduce the computational effort. Hembera et al. [38] point out that for such methods the frequency of the phenomenon to be investigated has to be known beforehand. It is therefore an efficient method for unsteady flow problems such as engine order excitation, rotor stator interaction and flutter. In contrast, large scale rotating stall type phenomena cannot be investigated with this method as the frequency is not known a priori.

Different CFD tools fulfilled the requirements stated above leading to the pragmatic solution to choose *ANSYS CFX 12.1*, which was already available and met the requirements. During the project the list of requirements had to be extended because of new findings, which were in particular the need to model the complex exhaust geometry with unstructured, tetrahedral mesh and the demand for scale-resolving turbulence modelling. Fortunately, both additional requirements were also met by the *ANSYS CFX 12.1* solver. This allows consistent comparison between all obtained CFD results.

### **3.2.1 Flow solver**

In *ANSYS CFX*, the Reynolds Averaged Navier–Stokes (RANS) equations are discretised using a vertex-based finite volume method, which is conservative and time implicit. The computational hybrid and unstructured mesh can consist of different element types such as hexahedrals, prisms, wedges and tetrahedrals. A control volume is constructed around each nodal point of the mesh and the fluxes are computed at the integration points located at the sub faces between two control volumes, see [39]. The discrete equations are evaluated using a bounded high-resolution advection scheme. The mass flow is evaluated such that a pressure-velocity coupling is achieved by the 4th order pressure smoothing, see Raw [40].

### **3.2.2 Computational mesh**

It was decided to begin the analysis with the air turbine configuration due to the availability of measurement data. In the first part, the meshing of the air turbine is described. In the second part details on the modelling of the steam turbine model are given, which represents a more complex case, but makes use of the experience gained with the air turbine.

#### **3.2.2.1 Air model turbine**

The following considerations have been made about the extent of the computational domain: for the phenomenon to be investigated standard simplifications in turbomachinery flows cannot be used. The rotating pressure events are not fixed to the frame of reference of the rotor blade. While the pattern itself may show a rotational symmetry, the number of pressure cells is unknown and potentially varies over time. Hence, the computational domain cannot be simplified to one or a number of passages in a time domain calculation. In fact, the whole annulus needs to be modelled. Furthermore, due to the small axial distance between stator and rotor blade, a rotational symmetry of the stator domain would also impose too many constraints on the flow in the inter-row space, the modelling of which was found to be very important for the phenomenon. Therefore, the stator assembly has been modelled in full annulus fashion, too. The same is true for the exhaust arrangement. A short section of the inlet duct was modelled as a passage and connected with a mixing plane to ensure rotational symmetric inflow. The interfaces between stator and rotor domain and rotor and diffuser domain have been modelled as transient stage interfaces, where flow quantities are interpolated over the interface.



A high quality hexagonal grid has been obtained with a minimum face angle higher than 30°, see Figure 17. It is apparent, that the grid density is constrained to lower values to keep the computational time within reasonable limits. The investigation was started with a coarse grid with dimensions as shown in Table 2. However, the grid density is kept relatively uniform to capture flow disturbances up and downstream and in the mid passage.

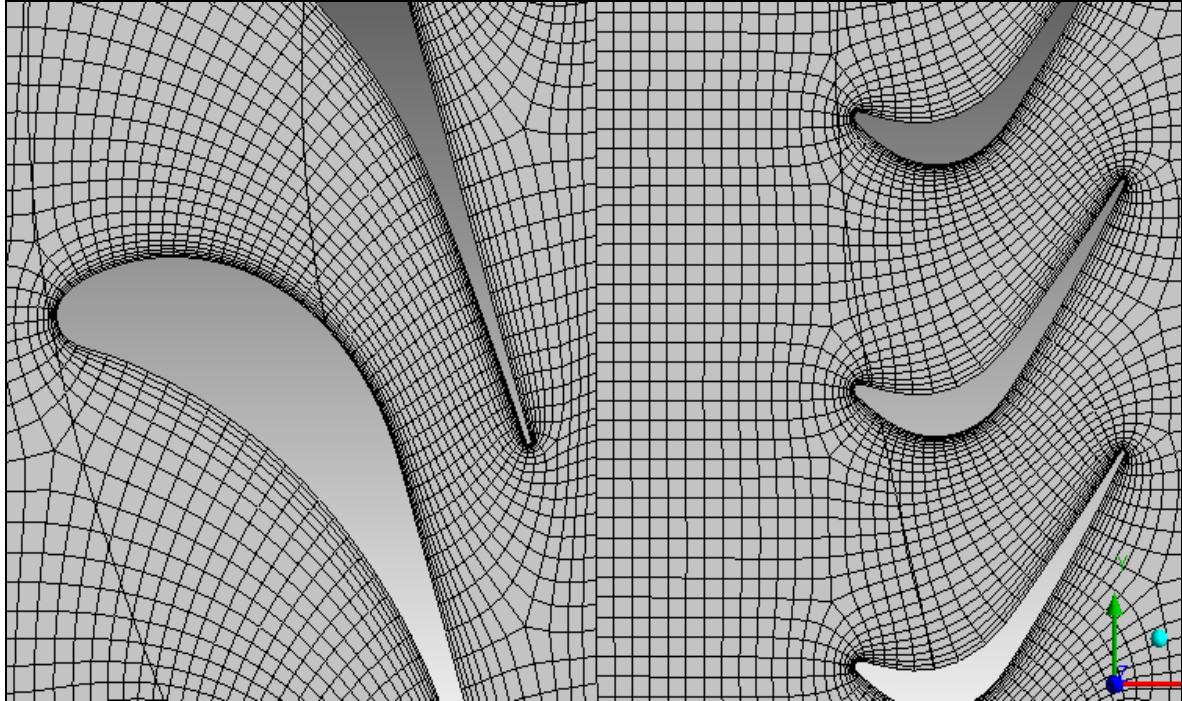


Figure 17: Coarse grid at mid span

For the purpose of a grid independency study a fine grid has been generated where the rotor domain was considerably refined, see Table 2. It was demonstrated that the number of stall cells and, more important, the fractional speed of the pattern relative to the rotor did not change with the refined grid.

Table 2: Number of nodes used in different grid domains

		<b>Stator</b>	<b>Rotor</b>	<b>Diffuser and Box</b>	<b>Total</b>
<b>Coarse</b>	Per passage	53'920	49'472	1'836	105'228
	Full annulus	2'696'000	4'452'480	165'240	7'313'720
<b>Fine</b>	Per passage	53'920	215'140	1'836	270'896
	Full annulus	2'696'000	19'362'600	165'240	22'223'840

The unstable nature of the rotating stall cells may be sensitive to the boundary conditions. Therefore, two different exhaust configurations shown in Figure 18 have been used to test their influence. As well as the axial-radial diffuser, a simplified rotational symmetry exhaust box was also modelled. The purpose was to obtain a sufficiently long distance between the unsteady flow phenomena and the outlet to minimize the sensitivity to the outlet boundary condition. Whereas at the inlet a constant total pressure and temperature is given with an axial inflow, the outlet boundary is defined as a fixed average static pressure over the entire outlet. Due to the small volume flows, the flow at the outlet boundary area may not have sufficient momentum, consequently in some areas the flow tends to enter the domain. For the exhaust variant “cone”, the outlet area was reduced until a sufficient through flow was achieved. The pressure ratio was adapted to match the measured volume flow. The variant “box” uses an opening type boundary condition, which allows flow to enter the domain. It is known from the measurement that the number of pressure cells found at one moment in time

is random in an interval. Similar behaviour has been found in the CFD calculations. The “cone” and “box” exhaust type calculations showed a different number of stall cells. The number of cells always remained in the range of cell numbers observed in the measurements. As the number of cells is of a stochastic nature, the characteristic feature of a pattern is the fractional speed relative to the rotor. The fractional speed was very similar for both exhaust configurations. This shows that the phenomenon is not or is not significantly affected by the chosen, rotational symmetric outlet boundary condition. For the following investigations, the “cone” type outlet has been applied.

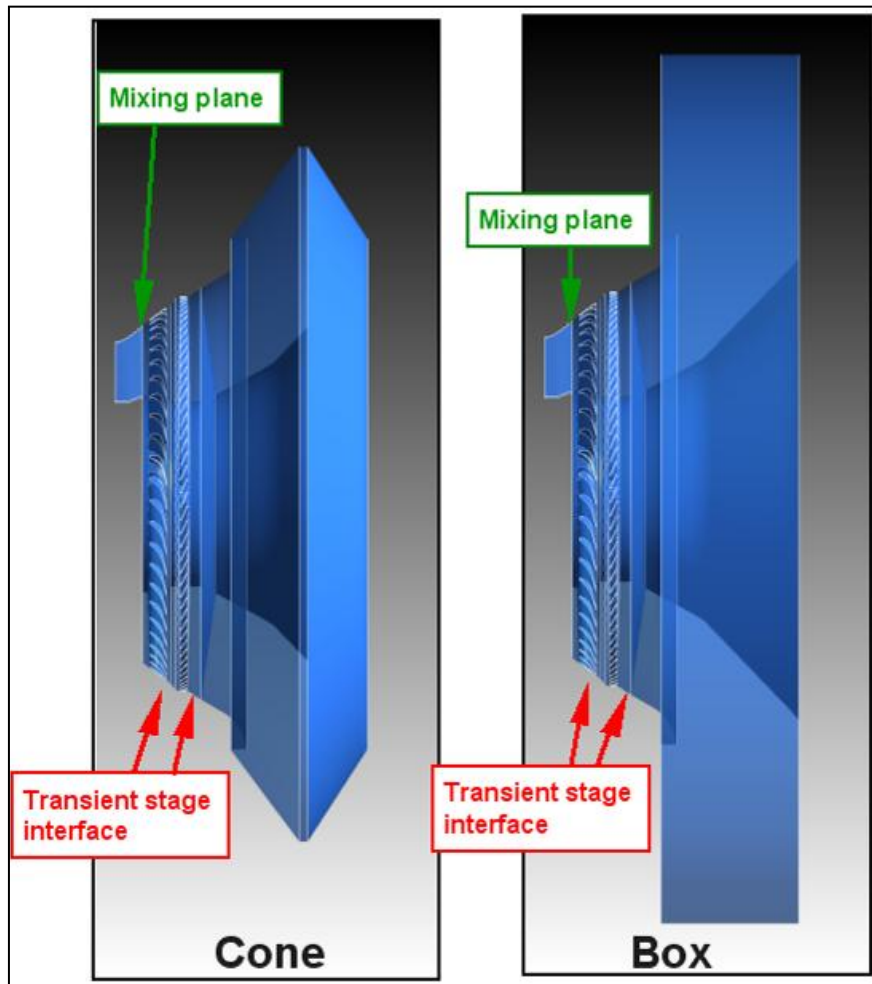


Figure 18: Exhaust configurations

First calculations have neglected geometry features like clearances. Gerschütz [14] found a sizable dependency of the fluctuations on the rotor blade radial clearance, so calculations have been performed which included the addition of a tip block grid, see Figure 19. The tip block has a one to one connection to the surrounding block domains. Along a line from leading to trailing edge, the tip block is split using a General Grid Interface (GGI), which allows connections without node matching. Although this requires interpolation, it is necessary to obtain a high quality main flow mesh with the given block topology.



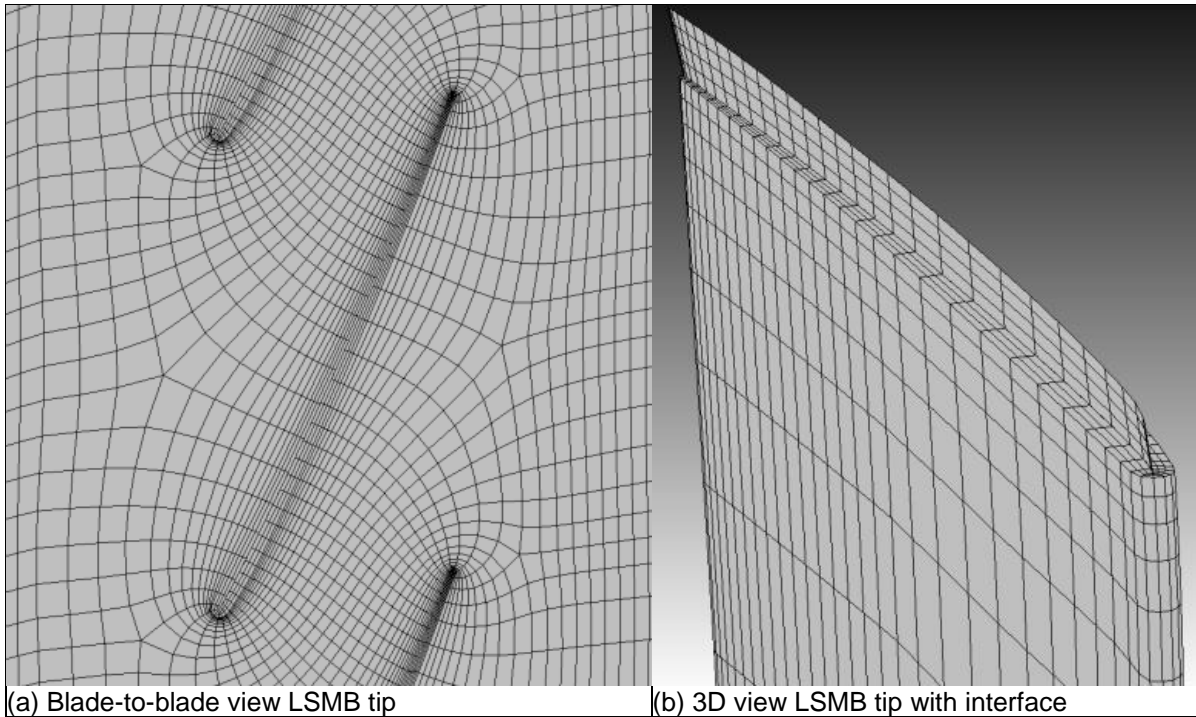


Figure 19: LSMB tip gap mesh

### 3.2.2.2 Steam model turbine

A number of changes were needed to adapt the air turbine model to the steam turbine environment. For more realistic inlet boundary conditions, an additional stage has been added to the computational domain. To limit the computational effort this stage has been modelled as single passage. A mixing plane has been used to model the stage interface. This clearly filters out any effects due to circumferentially non-uniform flow leaving the penultimate stage. On the other hand, the spanwise flow distribution is captured resulting in a high incidence on the following stator blade row. The penultimate stage contributes also significantly to the stability of the calculations as it acts as a nozzle into the full annulus domain keeping the total inlet mass flow constant. The last stage is then again modelled as a full annulus with sliding planes as stage interfaces. At first, also a rotational symmetric exhaust configuration has been selected of the type “cone”, see section 3.2.2.1.

In the course of investigation also the real exhaust geometry has been modelled, see Figure 20. To mesh this very complex geometry a hybrid approach has been applied. While the blade zone remains discretised with hexahedral elements, the exhaust domain is meshed with tetrahedral elements. This allows an automatic meshing of the complex geometry. The interface between the two mesh types is placed in the diffuser downstream of the LSMB. In addition, here a sliding plane approach is used as stage interface. This permits capturing the pressure variations in circumferential direction at the LMSB trailing edge caused by the non-axisymmetric exhaust.

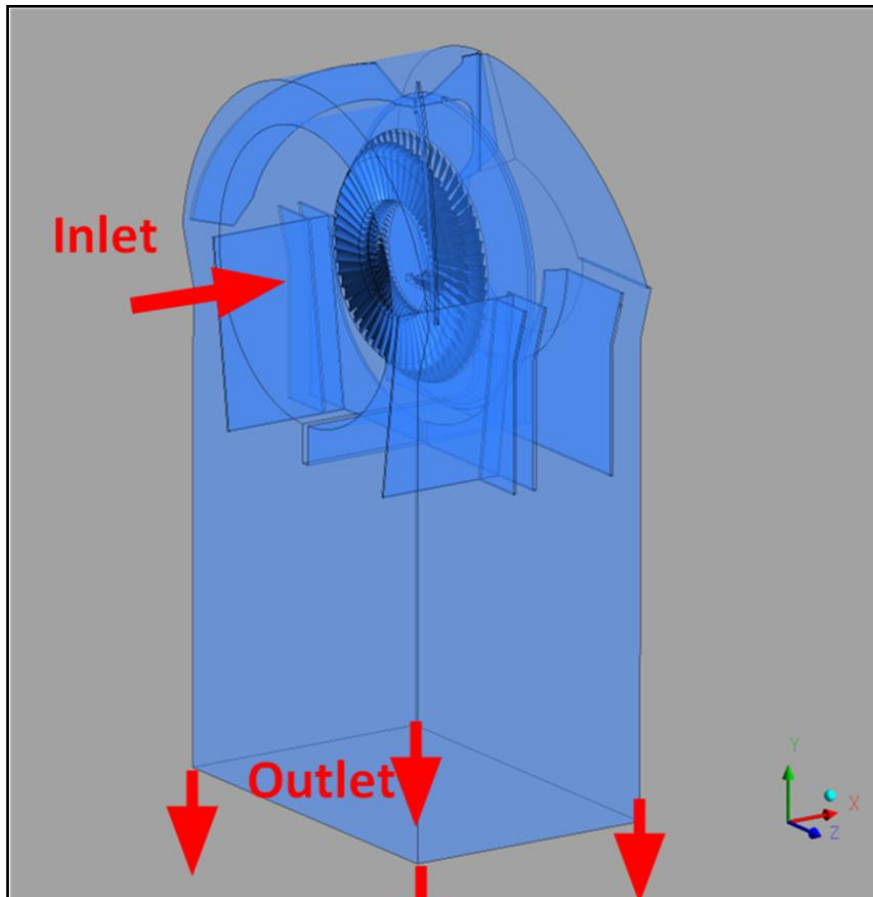


Figure 20: CFD model with realistic exhaust configuration

Table 3 shows the mesh sizes for the different configurations. It has been found that the coarse mesh does not resolve the rotating stall type phenomenon for both exhaust variants. The model is anyway useful to establish a steady state flow field, which is then interpolated onto the medium mesh. For the realistic exhaust variant, an even finer mesh with 15.9 million nodes has been used to confirm mesh independence. It has been found that a further mesh densification does not lead to changed results with respect to the observed quantities of interest. The following presented results are based on the medium mesh.

Table 3: CFD mesh size for the different variants

		<b>Turbine</b>	<b>Diffuser and Box</b>	<b>Total</b>
		[Nodes]	[Nodes]	[Nodes]
<b>Symmetric exhaust</b>	Coarse	1'878'656	250'944	2'129'600
	Medium	4'178'912	250'944	4'429'856
<b>Realistic exhaust</b>	Coarse	1'878'656	699'242	2'577'898
	Medium	4'178'912	699'242	4'878'154

With the same approach as in the air turbine, a tip gap has been included to the LSMB to study the influence of the leakage flow. Since effects on the stall cells have been observed, two different tip gap sizes were modelled to investigate the sensitivity.

### 3.2.3 Fluid modelling

The fluid in the air model turbine has been modelled as a perfect gas using the properties of air under atmospheric conditions. Due to the low speed conditions, only small changes in pressure and temperature occur allowing the assumption of perfect gas conditions.

Typically, in low-pressure steam turbines non-negligible variations of gas properties appear because of the large changes in density and temperature and especially due to the crossing of the saturation line. Measurements and steady state CFD calculations have demonstrated that under the given LVF conditions the steam remains well above the saturation line due to the heat produced by ventilation. This allows the usage of an equivalent perfect gas condition as the change of the perfect gas coefficients is small in the range of pressure and temperature present in the fluid domain.

### 3.2.4 Time accurate modelling

Apart from the spatial resolution of the domain, considerations on the time scale and runtime have to be made for an unsteady CFD calculation. *ANSYS CFX* offers the choice of a first or second order transient term. In the presented work, a second order backward Euler scheme is used. This scheme is robust, implicit, conservative in time and does not have a time step limitation. It is second-order accurate in time, but not bounded which may lead to some non-physical oscillations. For quantities where such oscillations may occur, a modified second order Euler scheme is used instead.

Different aspects have to be taken into account to select an appropriate time step. The time step has to be maximized to reduce the computational time without compromising the modelling accuracy. The stator and rotor domain are connected with a transient stage interface. Hence, blade passing and rotor stator interaction occur. To avoid artificial clocking effects the blade passing needs to be resolved with sufficient time steps. On the other hand, the frequency of the rotating stall cells is more than a magnitude smaller than the blade passing frequency. As the blade passing effects are of second order interest a relatively large time step can be chosen from this perspective, leading to a minimum of 10 to 20 evaluations per blade passing. Another criterion to select an appropriate time step is the Courant–Friedrichs–Lewy (CFL) number

$$C = \frac{v\Delta t}{\Delta x},$$

where  $v$  is the flow velocity,  $\Delta t$  is the time step and  $\Delta x$  the discretization length scale. It is a criterion for numerical stability. The *ANSYS CFX* solver uses an implicit transient scheme allowing CFL numbers far above one. For standard two equation turbulence models, maximum CFL numbers up to 20 have been used. More advanced turbulence models, such as the scale-resolving SAS-SST are recommended to use a CFL number of one or smaller, see [41]. The final assessment of the chosen time step has been done with a sensitivity analysis reducing the time step by a factor of two. As time step independence has been achieved, the larger time step is used for the subsequent investigations.

Beside the time step, the total runtime must also be selected appropriately. The calculation starts with an initial guess of a blade periodic steady state solution, which has been done beforehand. It takes a certain time to establish the set of rotating cells. Figure 21 shows an example where the instability established after approximately one revolution. To analyze the

frequency of the fluctuations a sufficiently large FFT window is needed. This is because the total signal length defines the minimum FFT bin size or in other words frequency resolution. Although the size of the time series can be artificially increased to increase the frequency accuracy by compromising the amplitude resolution by zero padding a certain number of rotor revolutions is regarded as minimum to obtain reliable spectral results. For example, a resolution of 12 Hz, which corresponds to roughly 2% of the frequency level of interest, approximately 6 rotor revolutions are required. This requires a stable set of cells for this period of time. The total computational time is also sufficiently long to allow a fluid particle to pass from inlet to outlet, as the time of flight is about three rotor revolutions. Furthermore, it has been checked that the global mass flow has been stabilized.

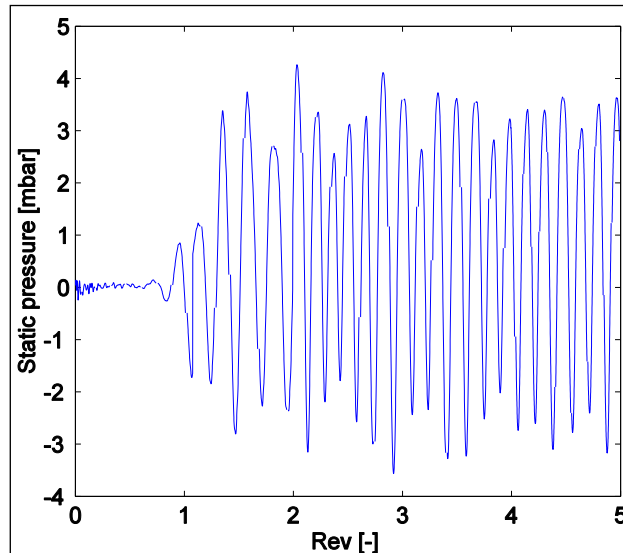


Figure 21: Pressure signal between stator vane and rotor blade at 80% span from a representative transient calculation

The stochastic nature of the number of cells presents a problem: in the measurement, several seconds can be recorded easily. In this time frame, all possible numbers of stall cells appear leading to the characteristic bell shaped group of peaks in the FFT plot. The CFD calculation was usually stopped after 10 to 15 rotor revolutions to limit the computational time. It is therefore most likely not possible to resolve all possible stall cell counts. Nevertheless, the nature of the phenomenon and its dependencies as well as the fractional speed can be investigated.

### 3.2.5 Turbulence modelling

In most industrial applications and especially turbomachinery, turbulent flow is present over large parts of the flow domain. In the case of LP steam turbines under low volume flow, turbulent flow is also expected both in boundary layers, as well as in the free stream turbulence. The most common way to close the Navier-Stokes-Equations and account for turbulence is the Reynolds Averaging known as Reynolds Averaging Navier-Stokes Equations (RANS). A variety of turbulence models are available for this closure, which are calibrated with empirical data of prototypical flows, Hussian [24]. For a steady state calculation an averaged velocity field is calculated, where artificial eddy viscosity accounts for the effects of turbulence. This type of modelling can also be employed in an unsteady mode named as URANS (Unsteady RANS). For flows with slow variation of statistical properties (slow compared to the characteristic turbulent time-scale) a finite-time temporal average can be used, see Hussian [24]. The aim is to resolve unsteady structures without recalibrating the model coefficients, see Fröhlich and von Terzi [42].

Generally, one can distinguish between two types of unsteadiness. Large scale unsteadiness can be imposed by a variation of the thermal boundary conditions or moving wall boundaries. This type of unsteadiness has typically a substantially lower frequency than turbulence. This allows a separation of scales, which means the RANS modelling assumptions are valid and the variation of the statistical mean values is caused by the external effects, Tucker [43]. The second type of flow unsteadiness is as a result of internal flow instabilities, which occur for example in shear layers. In this case the separation of scales is more difficult as larger coherent structures may depend on the smaller turbulent structures. This larger vortical structures may also disintegrate into smaller vortices downstream. Such an interaction may not always be handled with URANS as it is not calibrated for this situation. Therefore, URANS is likely to fail to predict the interaction between resolved fluctuations and unresolved turbulent fluctuations. A catalogue of URANS failures in such situations is reported in Tucker [44].

The fundamental question arises whether this is also the case for rotating stall in LP steam turbines. Tucker [43] proposes the following checks whether a spectral gap exists or not. In other words: is the frequency of the turbulence clearly larger than the frequency of the coherent structure to be investigated? For the example of wake boundary layer interaction a reduced frequency to characterize the ratio of the approximate period for a fluid particle to pass through a blade passage to the wake passing period can be calculated

$$\tilde{f}_c = \frac{1}{t_c} \frac{c}{v},$$

where  $c$  is the blade profile chord,  $v$  the relative flow velocity at the trailing edge and  $t_c$  the wake passing period, which is for compressors typically between 0.8 and 1.2. The Strouhal number of the shedding is

$$\tilde{f}_b = \frac{1}{t} \frac{l_{TE}}{v} \approx 0.3,$$

with  $l_{te}$  as trailing edge length and  $t$  the shedding period. The boundary layer thickness  $\delta$  can be assumed as fully turbulent flow with

$$\frac{\delta}{x} = 0.37 R e_x^{-0.5}$$

and the turbulent eddy scale  $l=0.09\delta$ . If the convection speed is around half the free stream velocity and the zone of interest is at half chord the reduced frequency of the boundary layer turbulence is calculated as

$$\tilde{f}_{BL} \approx f_{BL} \frac{c}{v} \approx 30 R e_c^{1/5}.$$

With a Reynolds number of around  $1 \times 10^5$ , a sufficient gap of  $\sim 300$  exists. For the rotating stall situation, the flow periodically separates from the blade surface. The eddy frequency of a shear layer caused by a separation bubble can be estimated with the Kelvin-Helmholtz frequency

$$f_{KH} \approx \tilde{f}_{KH} \frac{v}{\theta} \approx 0.032 \frac{v}{\theta},$$

where  $\theta$  is the momentum thickness and  $v$  the mean velocity of the two shear layer streams. For a half chord length separation bubble the reduced frequency can then be calculated as

$$\tilde{f}_{KH} \approx f_{KH} \frac{c}{v} \approx 0.025 R e_c^{0.5}.$$

The steam turbine model has a Reynolds number based on chord and trailing edge velocity of around  $3 \times 10^4$ , which results in a reduced frequency of  $\sim 4$ . The air model turbine is in a similar range with a Reynolds number of  $2.7 \times 10^4$  and a reduced frequency of  $\sim 4.1$ . The characteristic time of a stall cell passing a passage is

$$t_{RS} = \frac{1}{f_{RS}},$$

where  $f_{RS}$  is the stall cell rotating frequency in the relative frame. Assuming the reduced frequency of the rotating stall to be

$$\tilde{f}_{RS} = \frac{1}{t_{RS}} \frac{c}{v}$$

it follows that the reduced frequency  $\sim 0.2$  of the rotating stall is about a magnitude smaller than the eddy scale of the selected characteristic separation. In theory, a separation of scales could just be possible, but the half chord length separation region selected by Tucker [43] is very likely too small in the context of rotating stall. Larger separation zones do exist in LP steam turbines under low volume flow, which consequently leads to lower turbulence frequencies and larger eddy length scales. Hence, having a RANS model to resolve lower frequency turbulence and unsteady modelling to pick up larger unsteady scales might lead to an overestimation of artificial eddy viscosity and consequently wrong results.

On the other hand, Lübcke et al. [45] point out the possibility that the formal requirement of a spectral gap between statistical modelling and the transient mean flow is heavily violated, without undermining the applicability of URANS. This is the case if the flow distortion of the unsteady effects is much smaller than the time scale of the free stream turbulence. This situation can for example occur in wake flows behind blunt bodies. The insufficient time of the turbulent effect to influence the mean flow reduces the effect of inaccurate modelling. Opposite to this, the turbulent scales in the boundary layer are much smaller than the unsteady mean flow effects. For this situation, the URANS model operates in a quasi-steady mode and there are no more reasons to question the model than in steady conditions. In Lübcke et al. [45] they conclude that the inferior predictive capabilities of URANS is then often a result of inaccurate modelling of fluid flow phenomena such as streamline curvature or high straining.

Another way to answer the question if scale-resolving modelling is required are the actual flow physics of the rotating stall situation. It is well known that URANS has difficulties to

model certain types of flows. The main problem is here that many types of these flow situations are present under low volume flow, which excludes URANS for accurate prediction such as vortex shedding, coherent vortex structures, larger unstable regions, anisotropic turbulence and high swirling flow. However, the stall cells themselves have only an analogy with these effects but cannot directly be compared. The stall cells for example can be seen as a vortex shedding, which seems plausible as their frequency is largely independent of the Reynolds number similar to the well-known Von-Karman vortex street. URANS has shown to give in some cases reasonable results for the frequency but leading to a large scatter of eddy viscosity in the separation zone, see Lübcke et al. [45]. Another assumption is to consider the rotating stall cells as an flow instability such as the Taylor instability. The number and size of the stall cells is then defined by the dimensions of the confined space, see Ljevar et al. [34]. It has been shown in [34] that this type of instability is sensitive to fluid viscosity. This leads to the conclusion that the cells may not be related to turbulence and may also not directly interact with turbulence, hence having a spectral gap or are below large free stream turbulence scales. However, the URANS result is still likely to be inaccurate because of the overall highly vortical and separated flow field leading to a significant overestimation of eddy viscosity consequently changing the nature of the stall cells. Concluding that scale-resolving simulation is required not necessarily because of the rotating stall phenomenon, but because of the overall flow situation.

In the last part of the numerical investigation a step towards scale-resolving turbulence modelling has been done. This has been mainly driven by the fact that the frequency of the rotating stall was actually not correctly predicted by URANS when compared with measurement data. Additionally, the pressure amplitude did not compare well with the measurement for certain configurations. The scale-resolving model, which has been employed, is the SAS SST model available in ANSYS CFX. It is a pragmatic approach towards resolving turbulence as it demands less strict requirements on the mesh density than a large eddy simulation (LES) and has URANS as a fall back in regions without unsteadiness. Figure 22 gives an overview of the steps from URANS to scale-resolving models. Numerous models exist which will not be discussed here. It is clear that a detached eddy simulation (DES) or LES could also lead to similar improvements. Furthermore, details of turbulent interaction with the boundary layer could be studied. Unfortunately, due to the large model size a further mesh densification to achieve the DES/LES requirements is far beyond the present study. This is even more a problem for Direct Numerical Simulation (DNS) where the effect of turbulence is not approximated, but directly solved. Already the SAS-SST computational requires up to two months of computational time on a 40 CPU cluster.

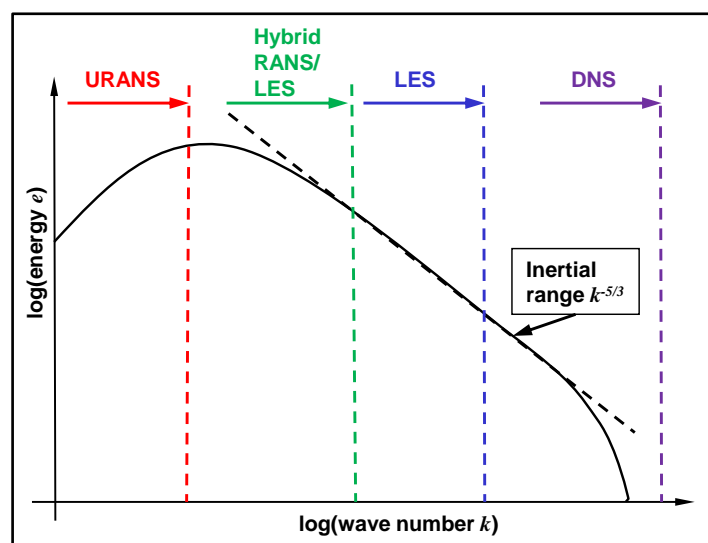


Figure 22: Idealized spectrum of turbulence with different turbulence modelling strategies

Coming back to the initial question: does the case of rotating stall in steam turbines allow the separation of scales? No final proof can be given here. It is possible that an URANS model exists or can be calibrated to correctly predict the rotating stall cell frequency and amplitude. On the other hand, it is clearly shown here that only the scale-resolving model delivers accurate results for the frequency of the rotating cells. It can therefore be claimed that the employed state of the art URANS model fails to separate the scales or overpredicts eddy viscosity because of the overall flow situation and can only be used to obtain qualitative results or in the worst case suppresses the stall cells.

Nevertheless, RANS and URANS have been used to an extent in this investigation purely for pragmatic reasons. It is clear that any turbulence scale-resolving method results in a significant increase of computational time. In addition, RANS is able to resolve the global time averaged flow field sufficiently well as it will be shown in the results section. If URANS resolves the internal flow instability, namely the rotating stall, it can give a good indication on the qualitative unsteady flow although the quantification of unsteady effects is questionable.

### 3.2.5.1 RANS and URANS model

The RANS and URANS turbulence model which has been used is the Shear Stress Transport (SST) model proposed by Menter [46]. It combines the  $k-\omega$  turbulence model and the  $k-\varepsilon$  turbulence model. This approach tries to combine the positive attributes of both models. The  $k-\varepsilon$  model does not require damping factors and is applied in a part of the boundary layer, this leads to higher numerical stability without compromising accuracy. The  $k-\omega$  model is used in the logarithmic part of the boundary layer where it is superior to the  $k-\varepsilon$  model in the case of adverse pressure gradients. On the other hand, the  $k-\varepsilon$  model is applied in the wake caused by the boundary layer as it is less sensitive to the free stream vorticity. In free shear layers, the  $k-\varepsilon$  model is employed as it represents a good compromise.

A special attribute of the SST model is the modified eddy viscosity function. This again increases the accuracy in flows with high adverse pressure gradients and adverse pressure gradient induced separations. The modification leads to a transport of turbulent shear stress, which is based on the observation that the transport of shear stress is proportional to the turbulent kinetic energy.

The described characteristics of the model make it the best suited RANS/URANS model for the presented numerical investigation.

### 3.2.5.2 SAS-SST model

A good explanation of the SAS-SST model is given in Menter and Egorov [47], which is briefly summarized here. Standard two equation models are built upon the basic concept that the effect of turbulence on the mean flow is obtained by two independent transport equations. The starting point is an exact equation of the turbulent kinetic energy  $k$ , which then requires a model for turbulent diffusion. For the second equation, has a term that is turbulent scale dependent, different formulations have been proposed. The most popular formulations are the  $\varepsilon$  and  $\omega$  equation. These equations are modelled in analogy with the  $k$ -equation using mostly dimensional and intuitive arguments.

A more fundamental model has been developed by Rotta [23], which is the  $k-kl$ -model. It uses an exact transport equation with the integral length scale  $L$  of the turbulent kinetic energy. The distinguishing feature of the model was a source term with a length scale involving a third derivative. This term has shown to be problematic and was omitted as it could not fulfil the boundary layer logarithmic law. Without this term it proved to be inferior to



the  $k-\varepsilon$  and  $k-\omega$  models. In recent years, the  $k-kl$ -equations have been modernised. It has been shown that the model is more consistent in inhomogeneous flows if the third derivative of the length scale source term is dropped rather than the second derivative. With this modification, the model allows the resolution of turbulent structures without dissipating them as a classical RANS model would do. The now termed Scale-Adaptive Simulation (SAS) automatically balances the contribution of resolved and modelled turbulent stresses. The model changes smoothly from a LES model through different stages of eddy resolution back to unsteady RANS dependent on the specified time step and integral length scale. The model has been formulated as one and two equation model. The SAS model employed here is based on the SST formulation, which has been explained in the above section. The standard SST  $\omega$  formulation is extended with a SAS term containing the length scale discussed.

## 4. Results and discussion

Initial CFD calculations have been performed investigating simple cases to verify the correct functioning of certain modelling aspects such as the mixing plane under reverse flow conditions. In addition, a simplified case of rotating stall in a vane less diffuser has been analysed to test different turbulence models and modelling settings. Due to the availability of the measurement data, a first set of steady state and unsteady calculations have been performed with the air model turbine in a full annulus configuration.

The numerical investigation of the steam model turbine began with a single passage calculation involving the full turbine cylinder. In addition, equilibrium steam properties have been used to model the fluid. Various operating points under LVF have been simulated. This has been done to derive inlet boundary conditions for the two-stage full annulus rear stage calculation using perfect gas as a medium. After obtaining unsteady results for the steam model turbine and comparing them to measurement data, different model parameters have been varied. This included the exhaust geometry, radial clearance of the LSMB and the operating point in terms of volume flow. In addition, more advanced turbulence modelling has been employed as significant discrepancy has been found between numerical results applying the standard engineering SST turbulence model and the measurement results.

After demonstrating the validity of the proposed CFD approach, the actual physics of the rotating stall phenomenon is discussed in detail. A statement is made about the initial assumption that the phenomenon can be categorised as rotating stall, as it is known from compressors.

### 4.1 CFD test cases

As described earlier the ANSYS CFX 12.1 CFD solver has been used for the numerical investigation. In an initial step some simplified test cases have been investigated, which are regarded to represent certain flow features of the LVF operation of LP steam turbines.

#### 4.1.1 Backward facing step and mixing plane

To investigate the behaviour of the CFD code under reverse flow conditions particularly over the mixing plane, which will be applied to stages upstream of the last stage, a channel flow over a backward facing step has been chosen. The geometry and measurement data has been obtained from Schulte [48]. The geometry of the channel is illustrated in Figure 23. It has to be emphasised here that the focus of this investigation is the correct functioning of the mixing plane under reverse flow rather than a good agreement with the measurement data.

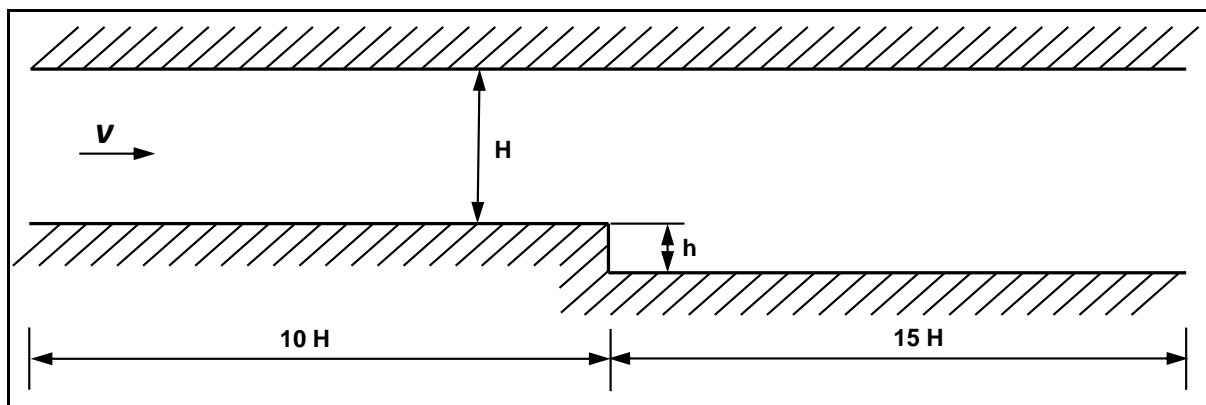


Figure 23: Geometry of the backward facing step

The corresponding parameters for the backward facing step can be found in Table 4. The medium in the measurement and CFD calculations has been water.

Table 4: Geometry and boundary conditions

<b>h</b>	<b>v</b>	<b>H</b>	<b>Re<sub>h</sub></b>
[mm]	[m/s]	[mm]	[-]
20	6.02	50	1.204*10 <sup>5</sup>

The CFD domain extends to the same space as shown in Figure 23. The computational mesh consists of an O-Grid layer at the wall boundaries and inner hexagonal blocks. To simulate a stage interface, the mesh domain has been split, see Figure 24. To allow a later rotation of one of the mesh regions, an axis of rotation in x direction has been introduced with a large radius to prevent a curved domain in tangential direction. Although this case could be treated in 2D, three computational nodes are introduced in tangential direction, because the CFD solver does not allow purely 2D computations. Symmetry conditions are enforced at the periodic faces of the domain in the out of plane direction.

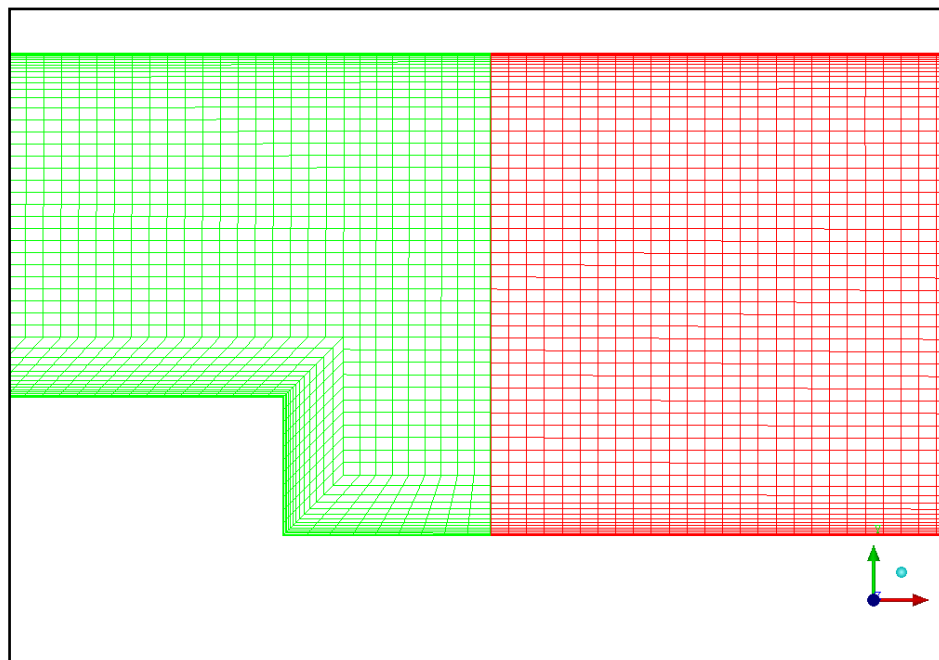


Figure 24: Computational mesh detail with mixing plane

It is well known that it is difficult to predict the correct reattachment length for a backward facing step with turbulent flow conditions. The relatively coarse mesh in combination with the  $k-\varepsilon$  turbulence model used here also leads to some deviation from the measurement results, see Figure 25. The numerical result reattaches earlier between the axial measurement positions four and six, whereas the measurement indicates a reattachment between position six and seven. To obtain better results in this respect, it has been shown that a much more detailed CFD model is required. Le et al. [49] applied Direct Numerical Simulation (DNS) to the problem and obtained a good agreement. Unfortunately, such detailed modelling is far out of reach for practical turbomachinery applications due to the immense computational effort and is probably not required. It has to be accepted that the size of separation regions may not be predicted perfectly accurate especially under the complex flow situation found under LVF operating conditions in LP steam turbines.

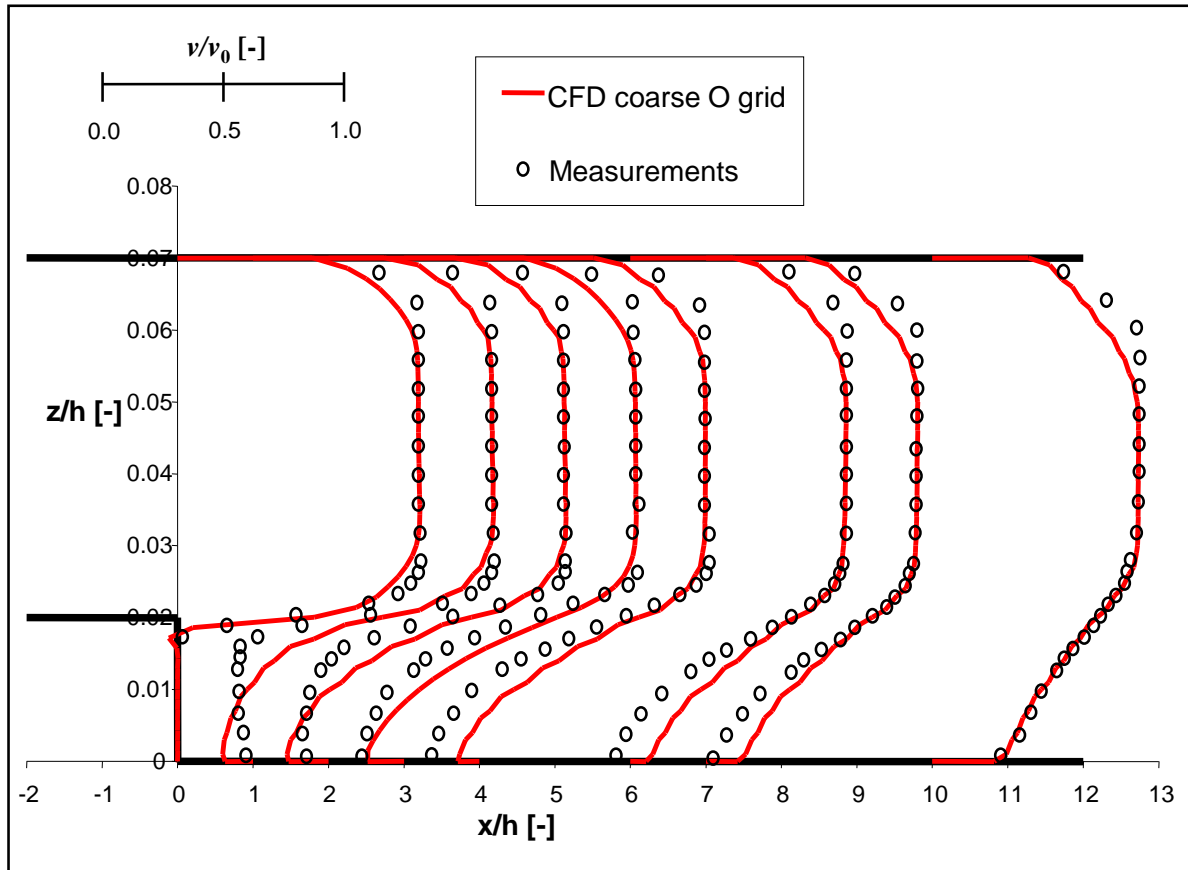


Figure 25: Measurement versus CFD axial velocity profiles, measurement results from Schulte [48]

To investigate the behaviour over the mixing plane one calculation has been performed using both mesh domains in the stationary frame and a one to one interface. In the second calculation, the downstream mesh domain has been defined as rotating with a mixing plane connecting the two mesh regions. As the flow is perfectly rotationally symmetric, no difference is expected between the two cases. In fact, both cases have shown identical results demonstrating that the mixing plane in the CFD can handle reverse flow in the given simple case. This is important as mixing planes will be used in different turbine CFD cases, where a large amount of reverse flow occurs and determine the boundary conditions for the full annulus modelled stage.

#### 4.1.2 Rotating stall in a vaneless diffuser

A simplified rotating stall case has been chosen to investigate the CFD code in the modelling of these conditions. Rotating stall can also occur in vaneless diffusers. An appropriate geometry and the corresponding boundary conditions have been taken from Ljevar [34]. The dimensions of the flow domain are briefly introduced in Table 5. The medium used is water.

Table 5: Diffuser data

	Symbol	Unit	Value
<b>Diffuser height</b>	$h$	[m]	0.008
<b>Outer radius</b>	$r_3$	[m]	0.4908
<b>Inner radius</b>	$r_2$	[m]	0.3227
<b>Radial inlet velocity</b>	$v_{r2}$	[m/s]	0.907
<b>Tangential inlet velocity</b>	$v_{t2}$	[m/s]	7.61
<b>Mass flow rate</b>	$\dot{m}$	[kg/s]	14.7

The incoming flow has a high tangential velocity, which is triggering the flow instability. Below a critical inlet angle, rotating stall is likely to occur. To simplify the case further, no circumferential variation in flow quantities, which one would normally observe from the impeller outflow, are introduced at the inlet. Similar as for the backward facing step, the flow domain can be treated as 2D, but due to the CFX solver, three axial computational nodes are added to the model. The mesh is also relatively coarse with a hexahedral structure. At the two disk shaped boundaries of the diffuser, symmetry conditions are enforced. Only after a few impeller revolutions, where the impeller speed defines the inlet tangential velocity, rotating stall occurs with the an inlet angle in the critical range. Four stall cells are rotating at a fraction of the impeller speed, see Figure 26. This is taking place without any artificial triggering or any wall bounded flow.

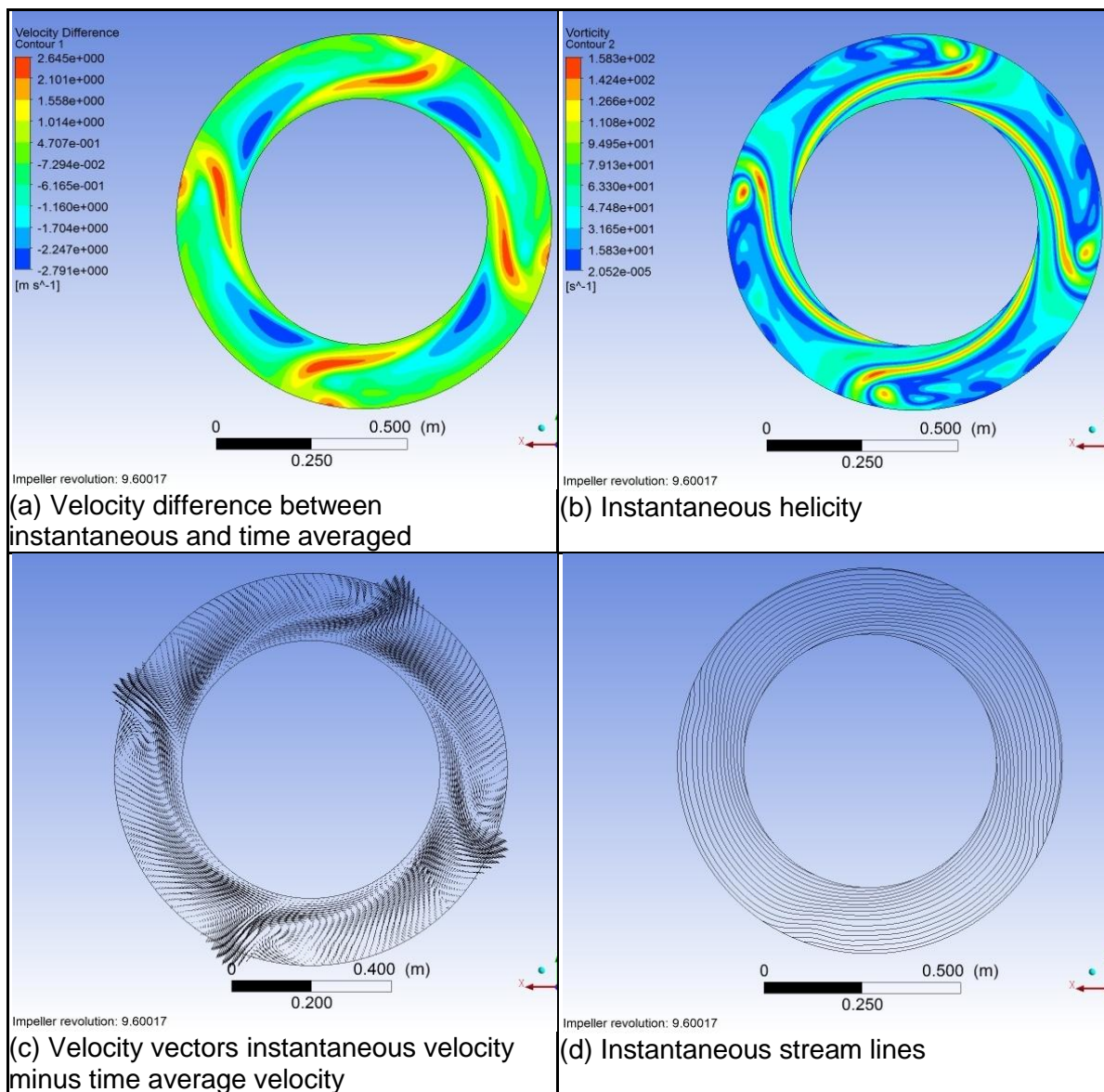


Figure 26: Flow field after rotating stall has been established

Figure 27 shows the results of instantaneous helicity for different turbulence models. Based on the Reynolds number the flow can be expected to be turbulent for the given flow situation. An inlet turbulence level of 5% has been specified. One calculation has also been performed without employing a turbulence model. The rotating stall situation is also present in laminar flow. It illustrates that in essence this flow instability is not due to the presence of turbulence. Ljevar [34] reported that employing a standard engineering turbulence model under these conditions can lead to results that do not represent the expectations. The flow with rotating stall leads in Ljevar's CFD investigation to an overproduction of artificial eddy viscosity and consequently to a damping and poor prediction of the rotating stall flow.

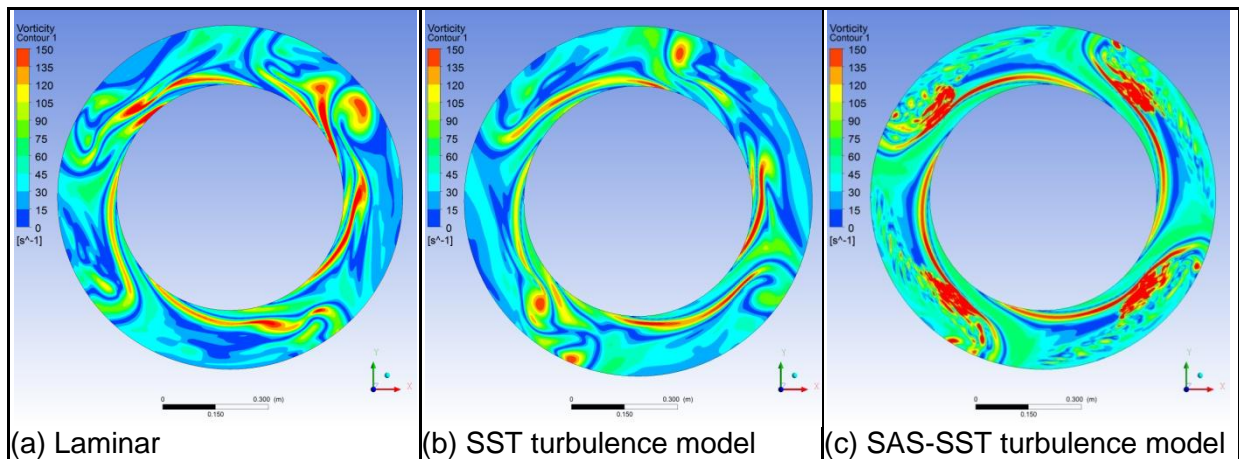


Figure 27: Instantaneous helicity under rotating stall with different turbulence models

In the investigation carried out here, the employed SST turbulence model did not lead to a similar situation. Stall cells did also occur as it is illustrated in Figure 27 (b). In a third step the turbulent scale-resolving SAS-SST model has been used. The blending factor indicated that the SAS model switched from the SST model to the scale-resolving model in the region where stall cells are present, see Figure 28. In addition, the helicity contour plot shows that turbulent fluctuations are resolved with smaller high helicity patches.

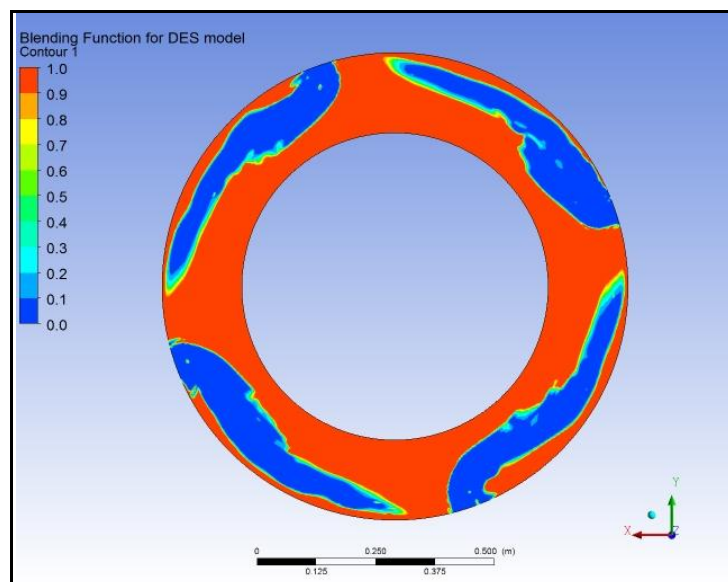


Figure 28: Blending factor for the SAS-SST turbulence model

However, unlike the work reported by Ljevar [34], all cases result in a set of four stall cells with a similar rotating frequency. It can therefore not be concluded, which of the models is required for a more accurate prediction. A laminar modelling is not applicable for the turbine situation as the flow is wall bounded with turbulent boundary layers. The comparison between the standard engineering turbulence model SST and the turbulent scale-resolving SAS model needs to be repeated for the turbine case to verify if the prediction of the rotating stall situation is influenced.

## **4.2 Air model turbine**

The CFD methodology described in section 3.2.2.1 has been applied to the air model turbine. Different volume flows and shaft speeds have been measured. In the following sections a rotor speed of 4000 rpm and a flow coefficient of 0.06 is compared to the CFD result. All unsteady CFD calculations have been initialised with a converged steady state computation. As mentioned earlier in section 3.2.2.1 no instability occurred for the initial coarse computational mesh. With a mesh refinement, a fluctuating pressure monitor signal has been detected after less than one rotor revolution indicating a low frequent flow unsteadiness as it is expected from the measurement experience. Before starting a deeper analysis of the unsteady flow field, the time averaged results have been compared with the time averaged measurement results. This is mainly necessary to check whether both CFD and measurement representing a similar global flow field and operating point.

### **4.2.1 Time averaged flow field**

Figure 29 shows the meridional flow field for the flow coefficient investigated by both measurement and CFD. The flow is drawn into the root of the driven rotor and exits towards the exhaust at the tip of the blade. An area of recirculation is created in front of the blade, where some of the flow at the casing is moved upstream towards the stator row forming the casing vortex. There is a large area of recirculation behind the rotor blade adjacent to the diffuser hub cone. This recirculation is partly drawn into the rotor blade row at the root. As mentioned in the introduction, this pattern is typical for the low flow regime. What is remarkable here is that this has been established at near atmospheric pressure and at reduced rotational speed. The overall characteristic of the flow field is well captured by the CFD calculation showing the regions of separation. Considering the complex nature of the flow field, and measurement issues concerning the physical measuring probe, it is not surprising that some of the low velocity regions show different velocity vectors. What is significant is that both techniques identify the same main through flow as well as the accompanying recirculation regions.



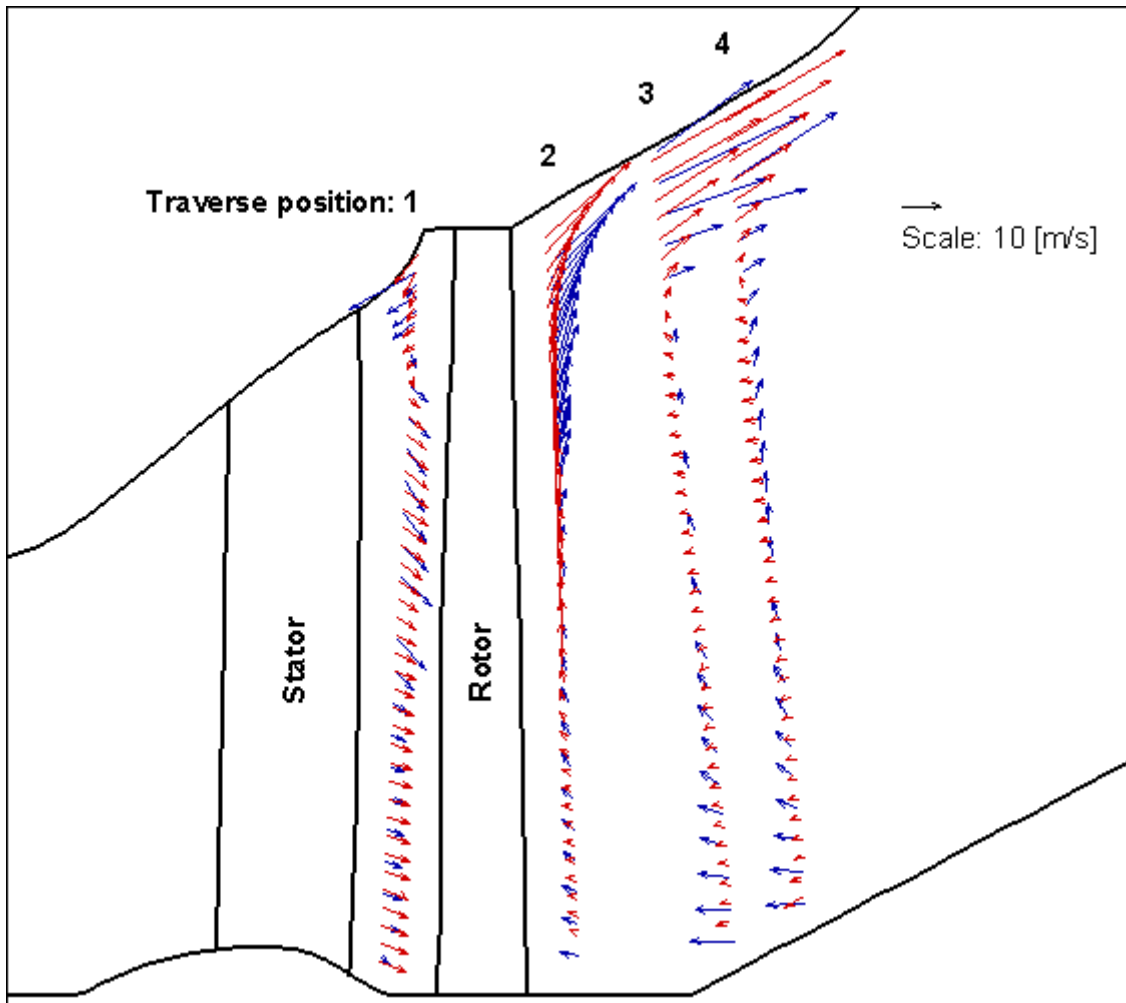


Figure 29: Meridional flow field (blue arrows: time averaged measurement, red arrows: steady state CFD)

The largest component of the flow vector close to the rotor blade is the circumferential velocity.

Figure 30 compares the velocity for two different measurement planes. Close to the casing between stator and rotor blade the flow travels nearly with the blade speed in circumferential direction. Considering the complex flow structure good quantitative agreement with the CFD results has been found. Higher levels of swirl are predicted by CFD after the rotor blade in the separated region extending from the hub towards mid span. This could be linked to an over prediction of the swirling component on the large hub separation zone. This zone is bounded by the downstream diffuser back wall and might even extend further into the exhaust cavity. These geometrical features are not entirely represented in the CFD diffuser and exhaust modelling as it was describe in section 3.2.2.1.



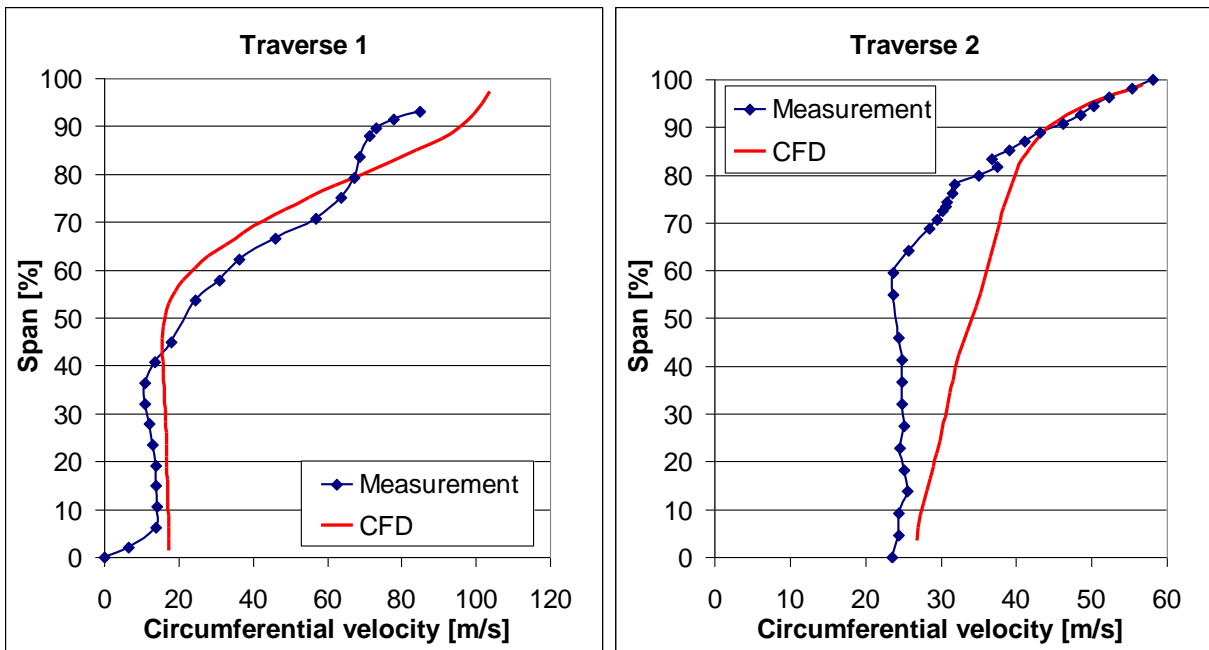


Figure 30: Circumferential velocity in front and behind the rotor blade

In summary, the time averaged flow field is predicted acceptably well considering the flow situation. Deviations between CFD and measurement have been found in regions where the flow velocity is low and very close to the rotor blade row where interference with the large probe shaft can be expected. Nevertheless, all characteristic separation zones are resolved illustrating that the chosen operating point of the CFD simulation is consistent with the measurement operating conditions.

#### 4.2.2 Unsteady flow field

After comparing the time averaged flow field with the measurement, the periodic phenomenon has been analysed in the frequency domain. In Figure 31 a FFT result of a CFD calculation is shown. A clear peak is visible for the frequency corresponding to the rotating pressure fluctuation. Two harmonic multiples of this peak are also present, as the signal is not perfectly sinusoidal. These peaks should not be confused with the set of multiple peaks found in measurements. Due to the limited runtime, CFD only shows one or two different cell numbers in five to ten rotor revolutions runtime. In the example given, one set of twelve cells was present over seven rotor revolutions. As the flow field is monitored in the relative frame of reference, another weak peak is present at 50 times the rotating frequency representing the number of stator blade wakes.

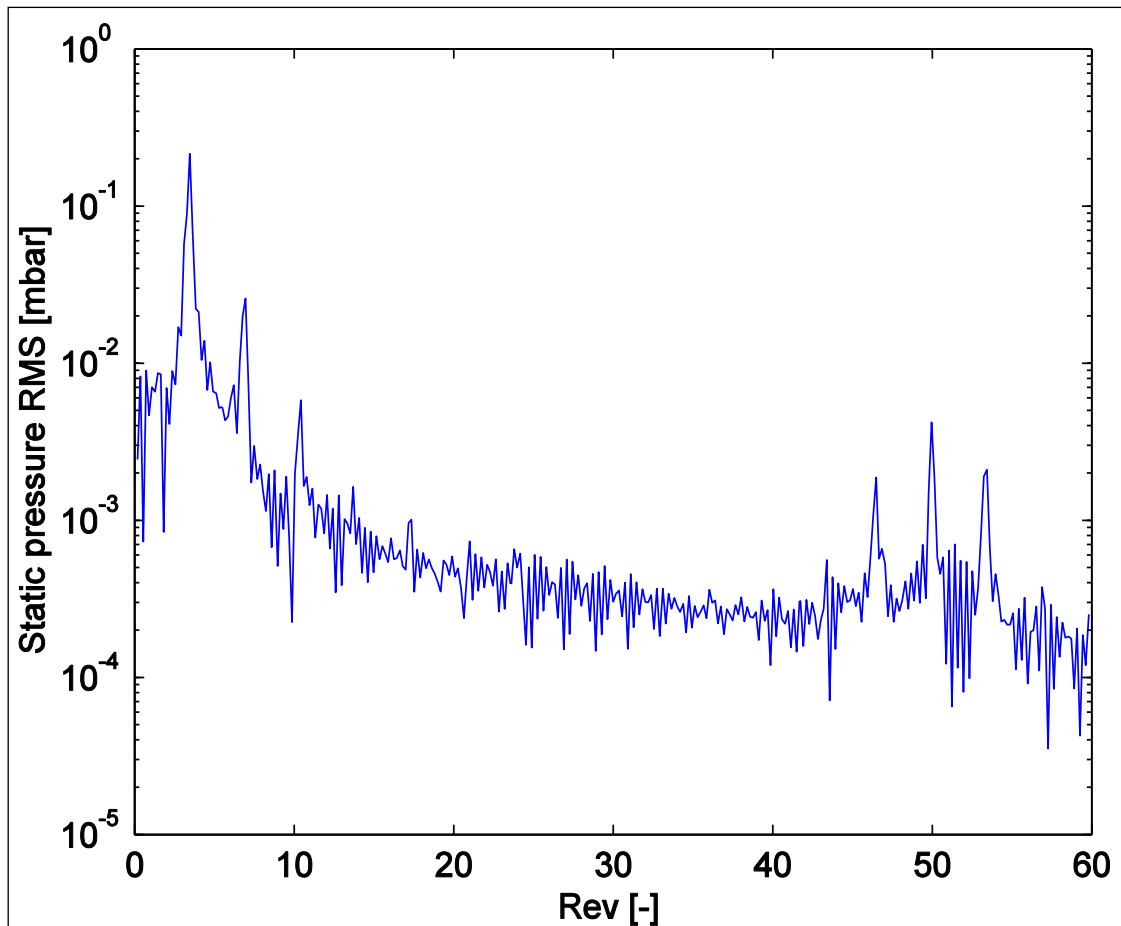


Figure 31: FFT for one static pressure monitor point between stator and rotor, 80% span, CFD, relative frame of reference

It is possible to determine the fractional speed and number of cells from two pressure monitor points, with one in the relative and one in the absolute frame. For verification, the number of cells can also be illustrated using a contour plot. As mentioned earlier, it is not possible to find all likely sets of cells due to the limited runtime, this is because individual cell counts may be present for several rotor revolutions in reality. The patterns detected in the CFD calculations have always been in the interval of cell numbers observed in the measurement. Discrepancy between CFD and the measurement was found for the fractional speed relative to the wheel. In cases where the fractional speed in the measurement was found to be approximately 0.5 of the rotor speed, CFD predicted it to be situated between 0.6 and 0.7.

Unsteady data has been recorded for different probe traverse planes. To identify the radial location of the cells, the pressure amplitude for individual cell patterns is plotted in Figure 32. As in the measurement, CFD predicts one set of cells being dominant, whereas the others are significantly weaker in amplitude. In the inter-blade space between stator and rotor blade the highest activity is found around 60% to 70% span according to the measurement. The CFD calculation predicts the highest amplitudes around 80% span. This discrepancy could be related either to the flow penetration by the relatively large probe, or to the prediction of the highly separated flow regime by CFD. Behind the LSMB at the traverse position 2, a pronounced peak of unsteadiness for the dominant cell number has been found around 80% span. The CFD results in a plateau of increased activity starting from 30% span. This may be related to the fact that the through flow is leaving the blade assembly at lower span heights as it has been found in the meridional view, Figure 29. Further downstream the

circumferential non-uniformity in static pressure of the cells reduces rapidly. Therefore, traverse position four is not displayed.

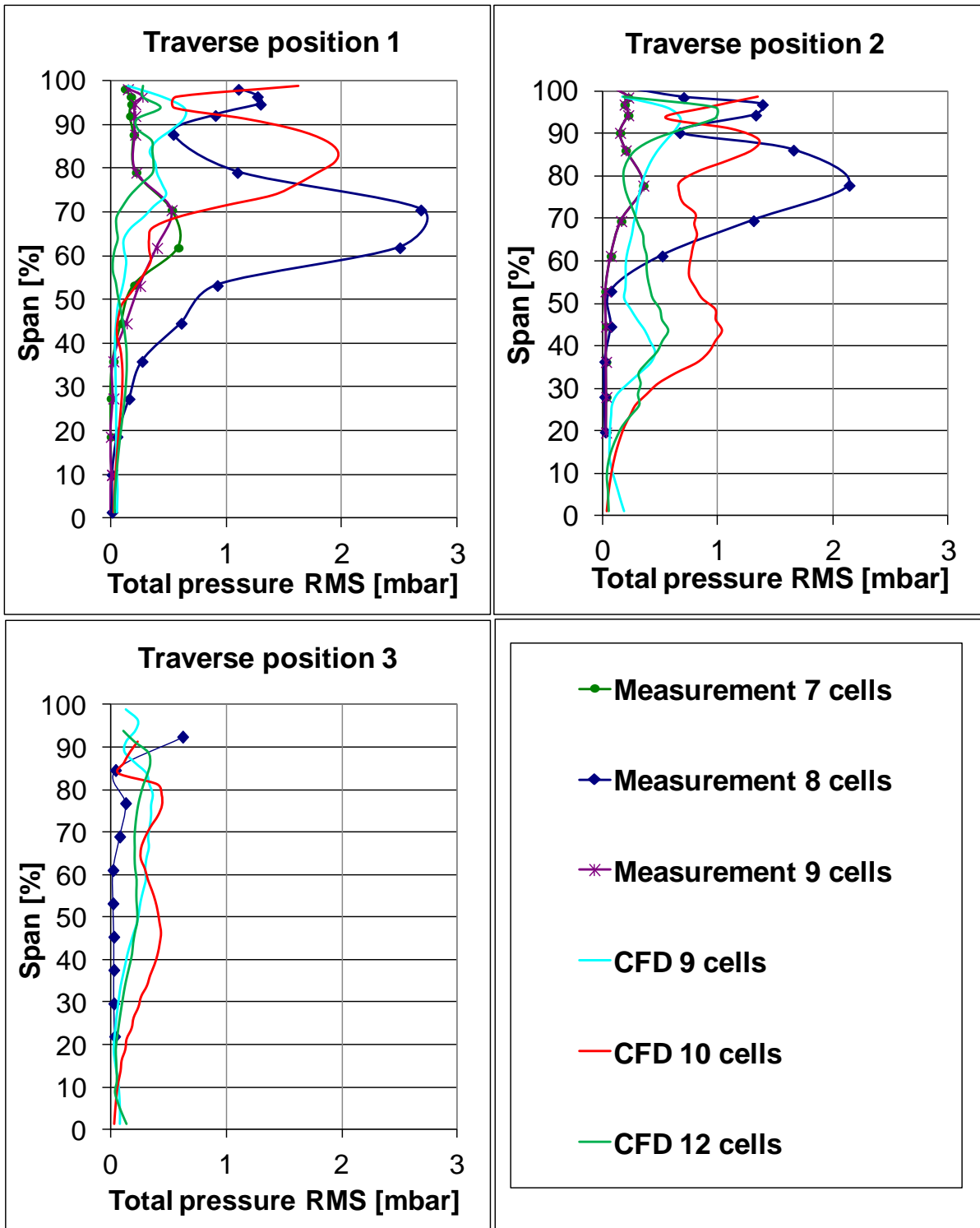


Figure 32: Unsteady pressure amplitude for different cell counts, the traverse positions are shown in Figure 12, page 24

### 4.2.3 Rotating stall cells flow structure

After a set of rotating cells is established the instantaneous flow field has been investigated. In a plane at the leading edge of the rotor, the regions of flow entering the blade passage and leaving it are visible in Figure 33. A twelve cell pattern can be identified by visual inspection defined by regions where flow is entering the stage and leaving the blade row upstream close to the casing. This is also in line with the unsteady pressure traverse, where the region of highest unsteadiness between stator and rotor has been identified close to the casing.

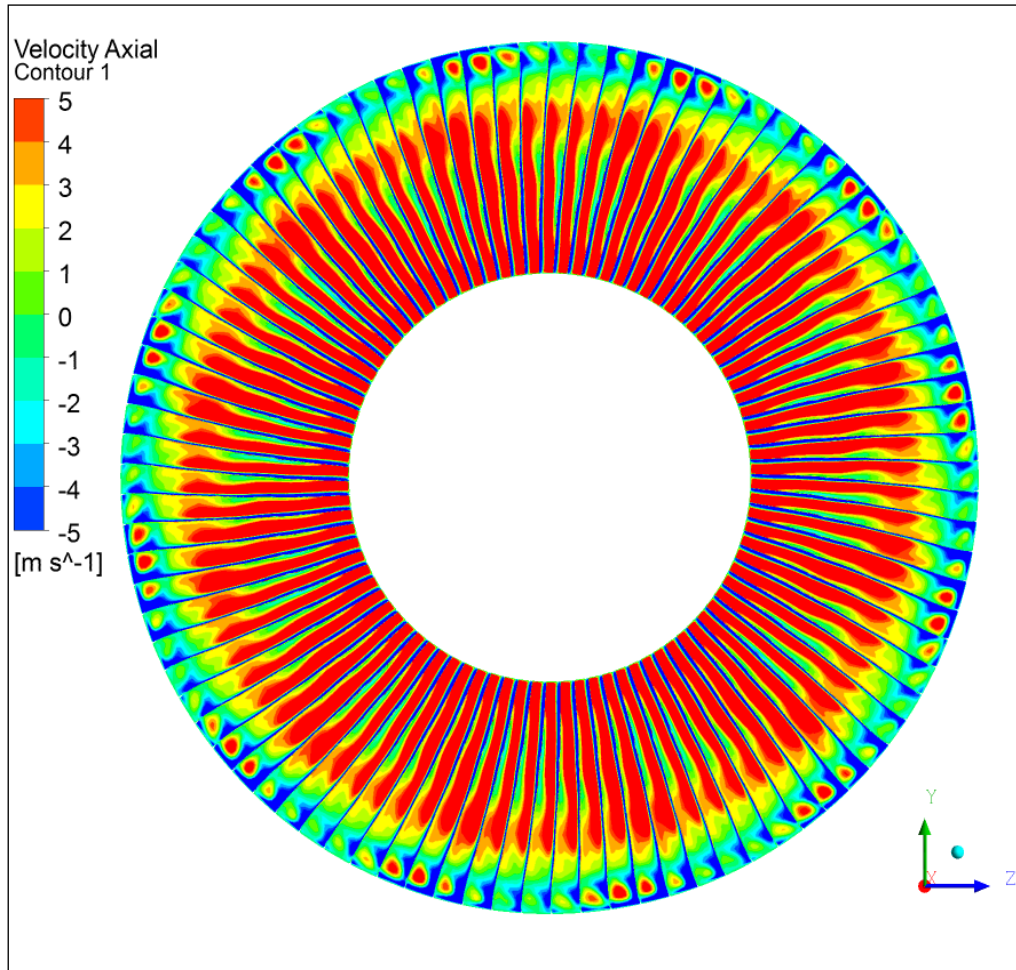


Figure 33: Rotor blade leading edge plane, axial velocity



In a blade-to-blade view, the passing of a stall cell can be observed. Figure 34 shows the movement of a cell in the relative frame, which takes about 4.2ms. A first observation in the blade-to-blade view is the strong negative inlet flow incidence to the rotor row - the incoming flow is nearly perpendicular to the machine axis. This leads to a large separated zone adjacent to the rotor blade at the pressure side. Flow is accelerated radially outwards in this separation region as it is highlighted by the back ground contour. Another separation zone is located on the suction side starting from about 50% axial chord downstream for the time instances (a) and (b). For (b) this zone is already smaller in size and allows flow to pass through the cascade. Between (b) and (c) the separation is convected downstream, giving way to a sizeable through flow. In the instance (d) the through flow is again decelerated indicating the arrival of a new stall cell. The flow carries a pronounced radial velocity component. It is therefore difficult to judge if the propagation of the cells is initiated by a deflection of the incoming flow, the fluid transport in radial direction or even the flow field behind the rotor blade. Despite the complex flow condition a regular set of stall cells is formed which propagates against the direction of rotation with a stable fractional speed, relative to the rotor blade.

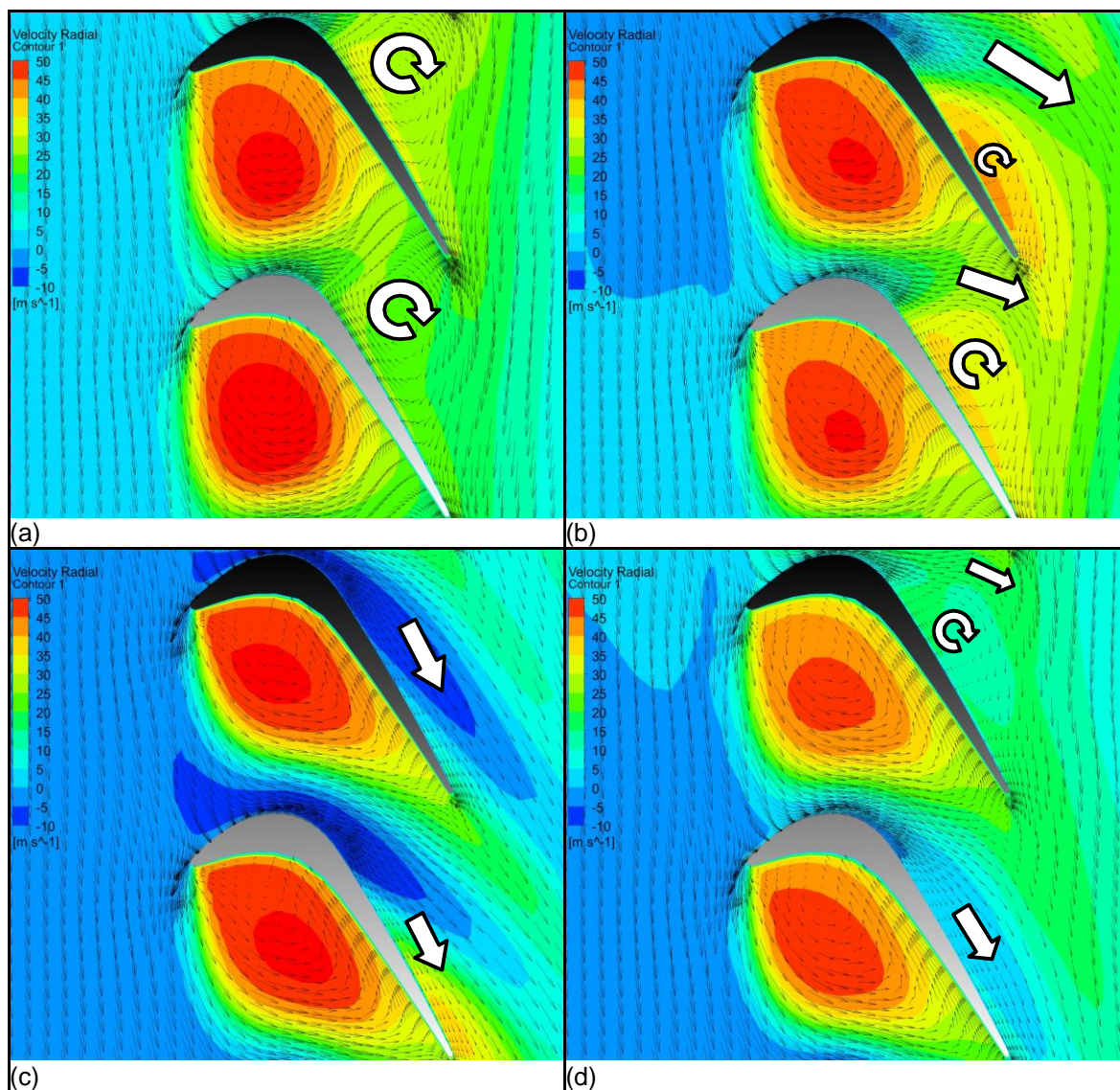


Figure 34: One cell passing in the relative frame at 50% span with relative velocity vectors in the blade-to-blade plane, radial velocity as contour and indicative white arrows

Another way to look at the phenomenon is presented in Figure 35. The deviation from the circumferentially band wise averaged axial Mach number is shown. Regions of positive and negative deviation are presented in red and blue, respectively. The rotating fluctuation is characterized by two bands, where the tip region shows a negative deviation a lower band between 60% and 75% span shows a positive deviation for a given angular position. This phase shifted pattern is also found in the CFD results. The two banded character of the unsteady flow is likely to be related to the presence of the torus vortex close to the casing.

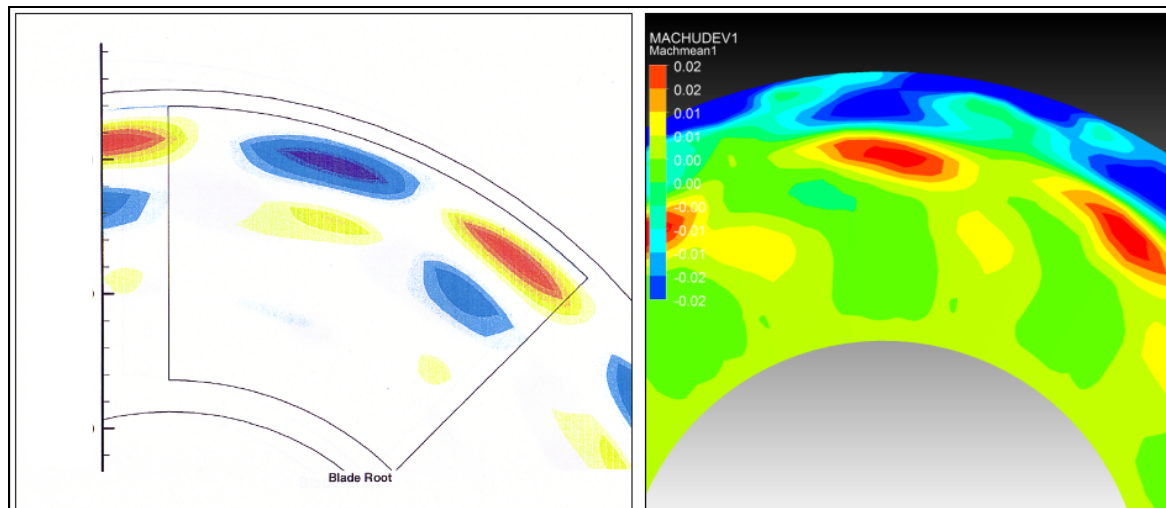


Figure 35: Inter-blade space plane with deviation of the axial Mach number from circumferential average value, left: Measurement, right: CFD

The two regions are also found in the amplitude of unsteady pressure related to the rotating cells. Figure 32 shows a region of unsteadiness between 90 and 100% span which exists over a wide range of flow coefficients. For lower volume flows, a second region of pressure fluctuation is present at span heights between 60 and 90%.

#### 4.2.4 Summary air model turbine

After some initial difficulties, it was possible to establish the rotating stall phenomenon in the numerical analysis of the air model turbine without artificial triggering. Many qualitative similarities with the measurement results have been observed. This includes the capturing of the global time averaged flow field, the establishing of a set of rotating stall cells with a cell count in the range of the measured cell count and a two-banded unsteadiness close to the casing, which is fluctuating out of phase. It supports the conclusion that the CFD approach captures the key physical effects observed in the measurement campaign. Unfortunately, the quantification of the fractional speed of the stall cells relative velocity to the rotor and the magnitude of unsteady pressure does not fully agree with the measurement results. This could indicate that the model is good enough to resolve the rotating stall, but some physical effects, which are determining the exact frequency and strength of the rotating stall pattern are not captured correctly by the chosen modelling.

#### 4.3 Steam model turbine

The steam turbine model represents some additional challenges in terms of numerical modelling as compared to the air turbine. These are mainly the multistage environment, the medium steam and the complex exhaust geometry. Additionally, the flow velocities are significantly higher as compared to the air model turbine with Mach numbers in some regions of the flow close to one. In a first step, a conventional single passage calculation with equilibrium steam properties including the four test turbine stages has been carried out to determine the boundary conditions for the two stage unsteady computations. As stated earlier, the unsteady full annulus computations have been carried out using ideal gas as a

medium to reduce the computational time. After first unsteady results have been obtained for the steam turbine model it became clear that significant stall cells only appear if a realistic exhaust geometry is modelled. After rotating stall has been present in a simulation with similarities to the measurement, comparison will be made between the air and the steam turbine. Similar to the air model turbine the steam model turbine numerical analysis has shown a significant deviation in the rotating stall frequency as well as unsteady pressure amplitude. To address these problems the modelling has been further enhanced using scale-resolving turbulence modelling, the SAS-SST model available in *ANSYS CFX*. As these enhancements showed promising results more geometrical details have been included to further improve the modelling accuracy. It has been shown that the inclusion of a realistic tip gap is important for the correct prediction of the fractional speed for the steam turbine model, whereas it is not required to trigger rotating stall and has a minor effect on the air model results in the tip gap range investigated.

After obtaining sufficient agreement between measurement and numerical modelling qualitatively and quantitatively, the unsteady effect has been investigated in more detail. Of major interest is the unsteady behaviour and the sensitivity to the geometry, which is driving the phenomenon. In a final discussion the question is clarified if the initial assumption that the effect can be categorised as rotating stall is correct.

#### 4.3.1 Steady state single passage calculation with equilibrium steam

Initial CFD calculations have been performed to determine the boundary conditions and investigate the steam conditions in the turbine. In Figure 36 the geometry of the full steam model turbine is shown. The computational domain extended through all four stages, the axial radial diffuser and a simplified exhaust box adjacent to the diffuser domain, which is not shown in the illustration. In all domain sections rotational symmetry is enforced. The stage interfaces have been modelled using a mixing plane.

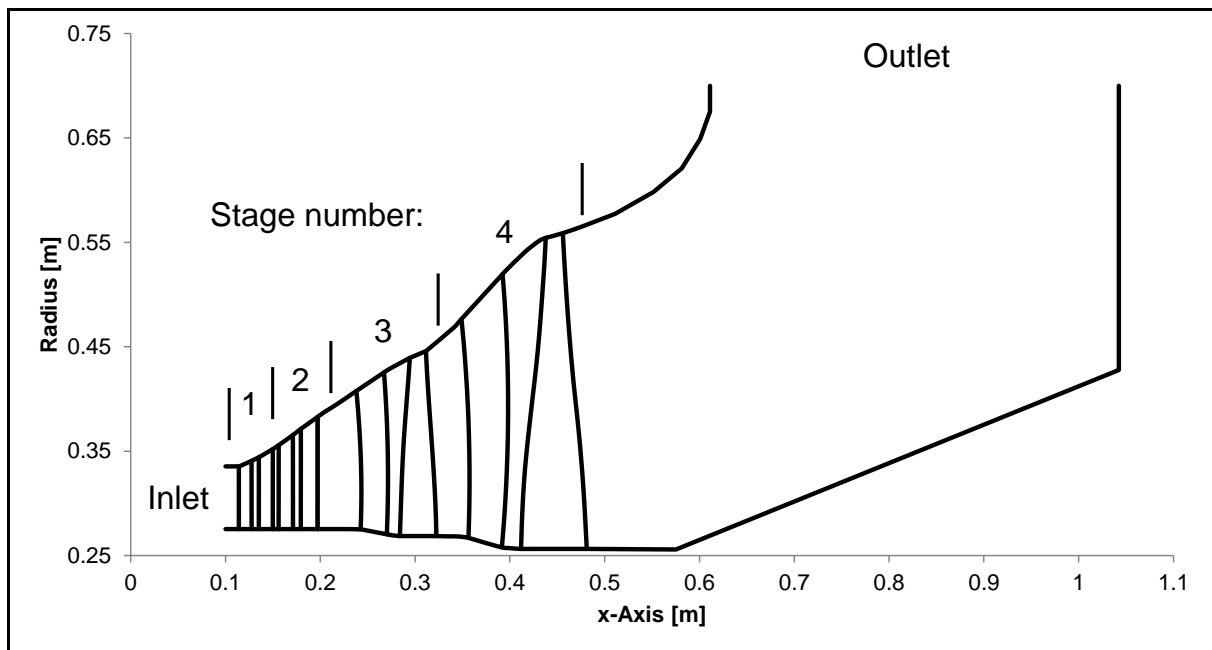


Figure 36: Meridional cross-section of the full steam model turbine cylinder including the axial radial exhaust, blade rows in grey

Different operating points have been investigated starting from conditions where all stages are still doing positive work on the turbine shaft. Figure 37 illustrates the change of the expansion line with a reduction of mass flow and in the last step with an increase in condenser pressure. The markers indicate the leading edge stator and trailing edge rotor

control planes. In all cases the penultimate stage is still generating, although small, positive work.

This allows in combination with the low-pressure ratio across the domain an ideal gas assumption for the unsteady computation, which reduces the computational effort. The lowest volume flow point with 5 % mass flow and 90 mbar represents the highest volume flow point where rotating stall appears. Inlet boundary conditions for the two stage unsteady computation have been taken between stage two and stage three.

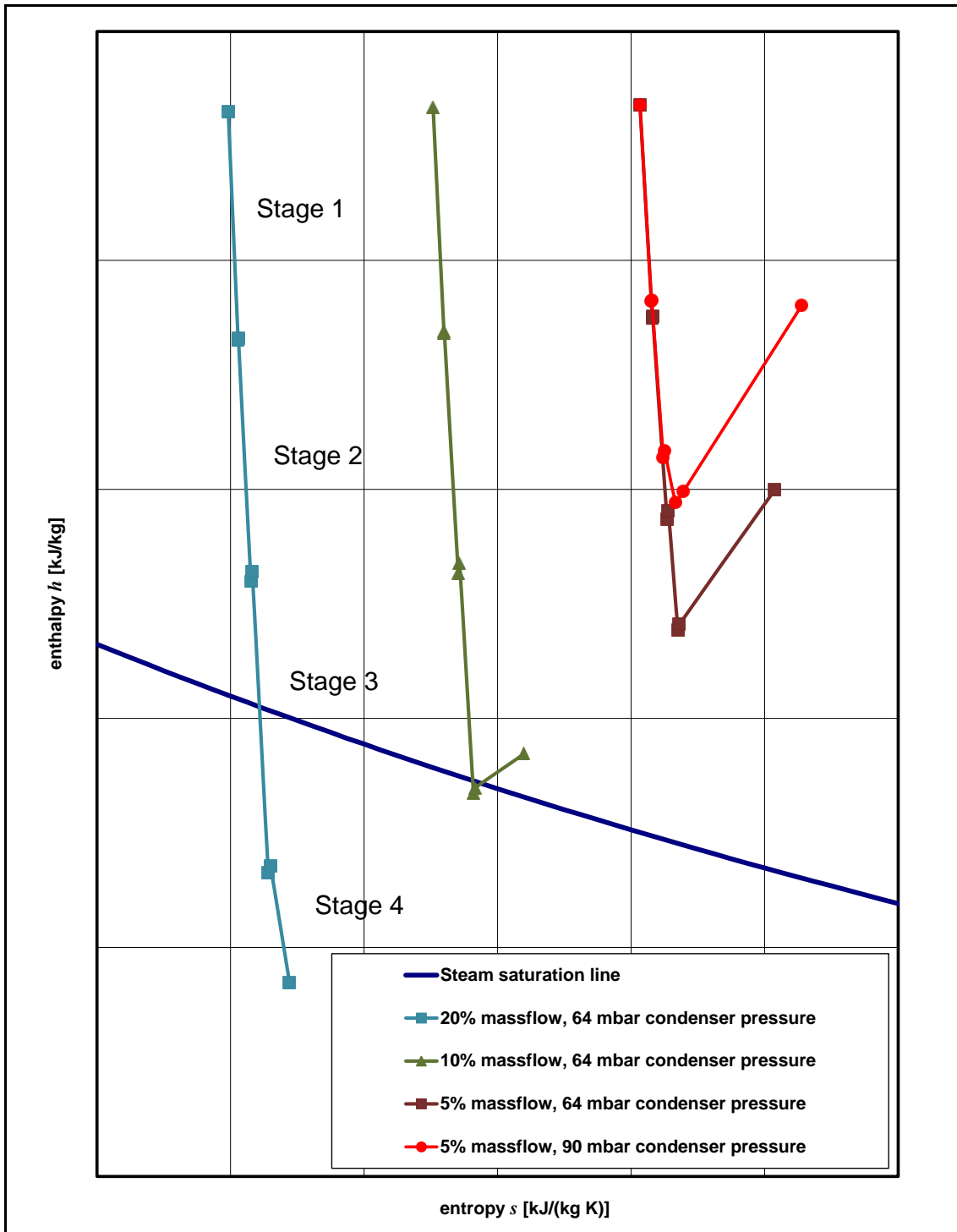


Figure 37: Expansion lines for different volume flows, four stage CFD result - steam model turbine



In Figure 38 the temperature at the LSMB blade surface is compared. The tendency towards higher temperatures is observed with a reduction in volume flow. CFD is predicting generally higher temperatures than measured. This is related to the fact that the CFD model is adiabatic and thus preventing heat flux through the inner casing as it occurs in the model turbine. The heat fluxes in the steam model turbine have been minimised by waiting until the temperature measurements stabilise. Nevertheless, as shown in Figure 38, the temperature is over predicted by approximately 25 °C, due to the adiabatic assumption in the CFD model.

As it was mentioned in section 2.1.3, Gerschütz [36] observed a frequency shift of the rotating instability with an increased inlet temperature to the model turbine as well as a decreased unsteady pressure amplitude. Unfortunately, the inlet temperature of the steam model turbine used could not be controlled but only measured and applied as a boundary condition to the CFD calculation. Comparing measurements with different inlet temperature due to seasonal operation changes of the steam supplying power plant revealed a different trend compared to Gerschütz findings. An increase of the inlet temperature had also led to a decrease of pressure amplitudes. This is linked to the change in fluid density and therefore aerodynamic force, which is associated with higher temperatures. On the other hand, the frequency of the rotating stall remained nearly unchanged. This is in line with the finding that the rotating frequency of the rotating stall cells is only marginally changing with a reduction in volume flow, whereas the temperature is increasing significantly. Most likely, the rotating fluctuations measured by Gerschütz in the 12 m<sup>2</sup> model turbine are related to the tip clearance flow and more sensitive to the local Mach number. For the steam model turbine investigated here, it is claimed that the frequency prediction is not significantly affected by elevated temperature levels in the CFD calculation. The modelling of the heat transfer at the inner casing is therefore not required.

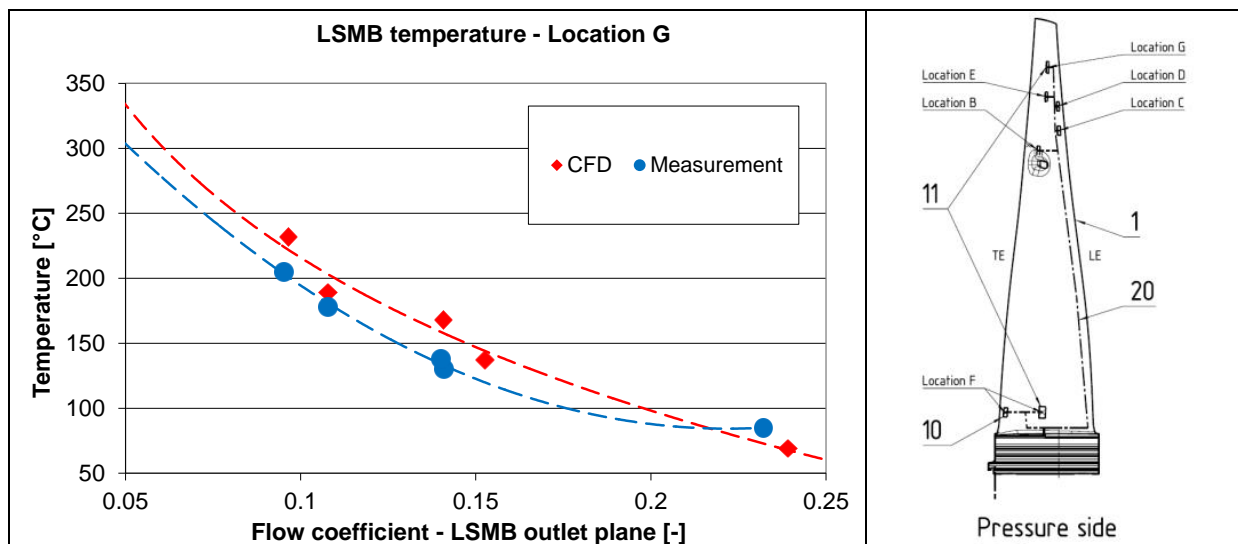


Figure 38: LSMB blade surface temperature measured at the strain gauge location G

#### 4.3.2 Realistic exhaust geometry

Figure 39 compares flow quantities for the different exhaust variants. The velocity field has a high circumferential non-uniformity of the returning flow for the realistic exhaust, which has been captured with three circumferentially placed probes, see Figure 12(b). The hood side probe S06 shows a positive tangential velocity. Towards the condenser side the symmetry of the swirling diffuser hub separation bubble is broken leading to even slightly negative swirl in the traverses S05 and S07. For the symmetric case the tangential movement of the

separated flow behind the LSMB is undisturbed leading to an over prediction of tangential velocity.

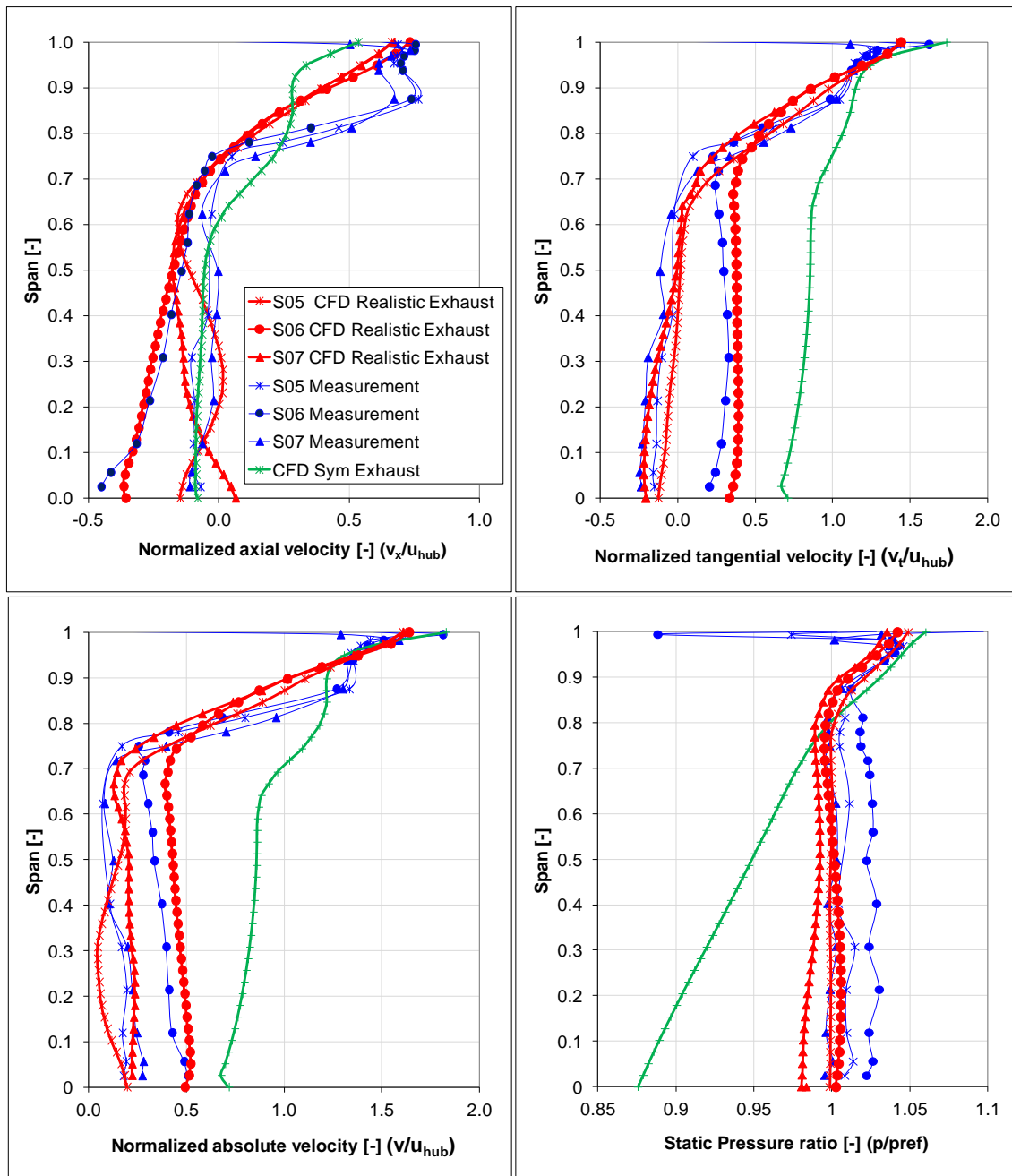


Figure 39: Time averaged flow field downstream of the steam model turbine LSMB in plane 62, see Figure 12

The measurement data confirms that the global flow structure can be predicted by CFD. In particular the non-uniformity of the returning flow around the circumference is well captured. Discrepancy is found in the remaining core flow velocity at 85% span. A closer look at the CFD results revealed that the double peak axial velocity behaviour is resolved but diffuses quickly towards the traverse location due to the comparatively coarse tetrahedral mesh in the diffuser domain. Unlike under design flow conditions the static pressure variation for the three traverses is marginal as the separated flow regime does not lead to significantly different diffusion between hood and condenser side of the exhaust system. The static pressure is nearly constant in the low momentum separation zone. The high swirl in the symmetric case results in an unrealistic static pressure gradient.

For the realistic axial-radial exhaust, a comparatively strong rotating stall pattern is present after less than one rotor revolution. The frequency of the disturbance is in a range of four to nine times the rotor frequency. The level of underlying noise and the peak pressure amplitude related to the rotating cells is more than a magnitude higher than in the symmetric exhaust case. Interestingly the frequency of the peak pressure is only marginally different between the two exhaust variants. On the high frequency side that blade passing is resolved in both cases. The results are indicating that non-circumferential disturbances may amplify an existing instability.

The presented results demonstrate that the modelling of the realistic exhaust geometry is important for LVF simulations, not only to trigger the instability but also to better resolve the highly non-uniform flow behind the LSMB. The presented CFD data in the sections below is therefore related to the results from the realistic exhaust configuration for the steam model turbine.

### 4.3.3 Influence of the exhaust on the unsteady flow behaviour

Starting from a steady state solution this calculation has been performed for several rotor revolutions without leading to rotating stall. An FFT analysis revealed a very weak rotating instability, see Figure 40. Possibly this instability grows stronger after many more rotor revolutions although there has been no detectable rise of amplitudes over the last 10 rotor revolutions. This leads to the conclusion that the instability remains hardly detectable in the symmetric exhaust case.

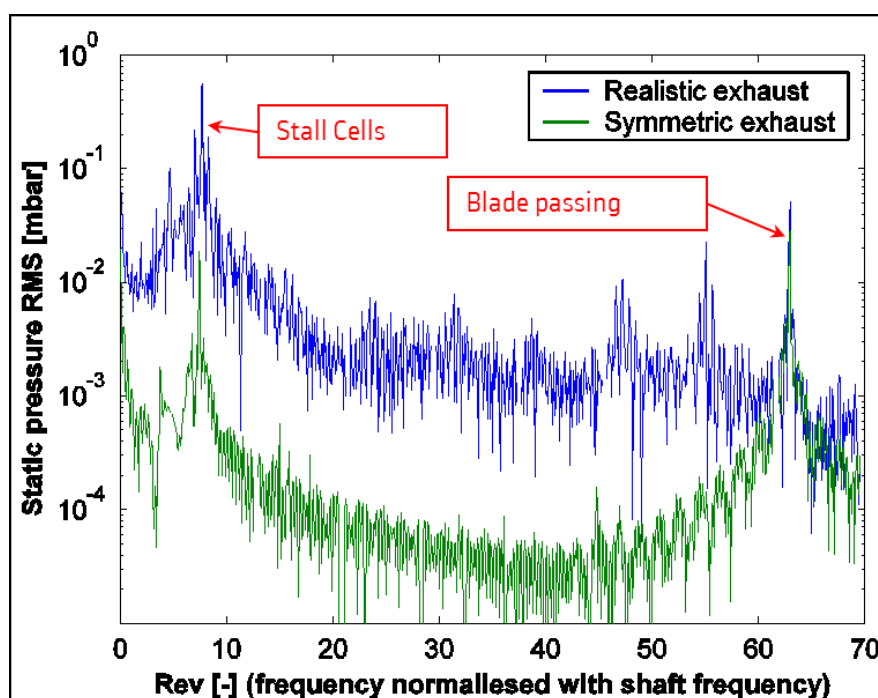


Figure 40: FFT analysis of 10 rotor revolutions, static pressure in plane 61 at 95% span height

### 4.3.4 Comparison to the air model turbine

The air model, as well as the CFD, is a vehicle used to investigate the behaviour of an actual steam turbine. In this section air model and the steam model measurements are compared to each other as well as the corresponding CFD results. Although the steam model turbine is more similar to the full size turbine, the air model turbine is useful because it is much more simple to operate and to change certain geometry features. In addition, the air model turbine

has a distinctly different geometry compared to the geometry investigated in the steam model turbine, see section 3.1. Both model turbines have shown rotating stall in the a similar flow coefficient range. It is therefore also an opportunity to test the numerical modelling approach on two different turbine geometries, verifying that the prediction capabilities are not case dependent. Furthermore, it is of interest to understand if the physical flow phenomena in both turbines leading to the rotating flow instability are of the same nature.

Figure 41 illustrates the global meridional flow field for the two turbines as modelled by CFD. Both characteristic separation regions are present with the casing vortex between stator and rotor and the large separation zone behind the LMSB. Another separation zone is present in the steam model at the stator inlet. This separation is related to the highly swirling flow leaving the low loaded penultimate stage. However, when operated at the same flow coefficient the flow remains attached in the air model due to the axial inflow without a penultimate stage. Differences are also found in the amount of flow being entrained from the diffuser into the rotor. The spanwise thickness of the remaining core flow at the casing behind the rotor confirms the similar volume flow through both machines.

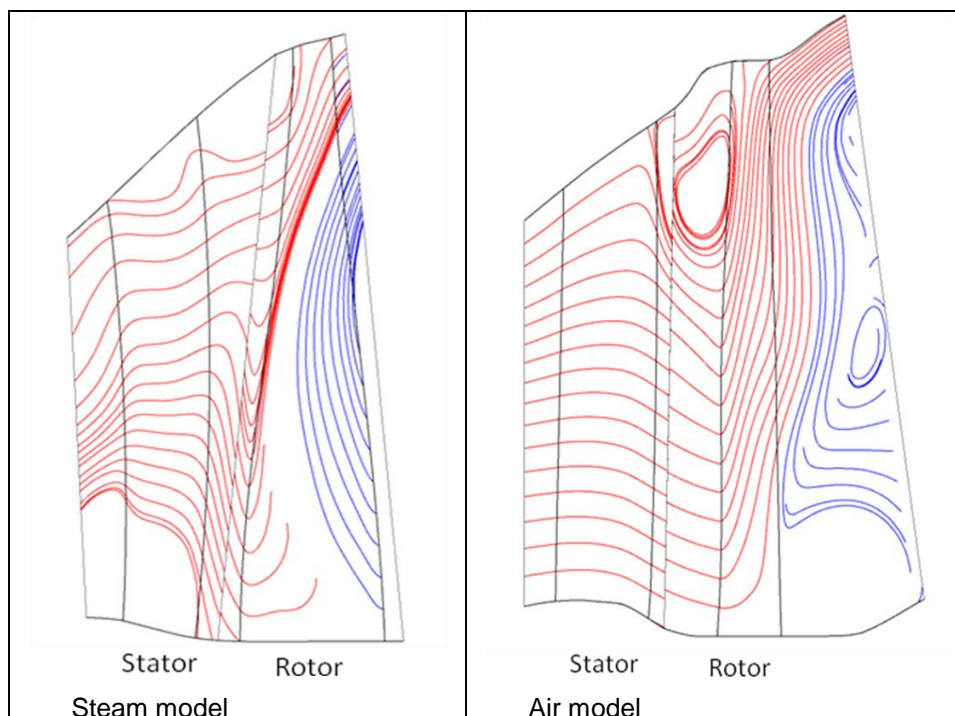


Figure 41: Circumferentially averaged meridional stream lines from CFD at  $\phi=0.06$

Despite the differences between the two models, a rotating stall mechanism is present in similar flow coefficient range of  $\phi$  between  $\sim 0.04$  and  $\sim 0.15$ . Moreover, the stall cell number and fractional speed of the cells to the rotor are similar. A group of cell systems is found with a preference for one cell set. Furthermore, the fractional speed is around 50% in the measurement. CFD is predicting the rotating pressure cells in both cases. As for the air model the propagation speed of the cells against the rotation here referred to as fractional speed is over-predicted by about  $\sim 10\%$ . The full set of cell numbers is not resolved with CFD due to the limited runtime. Nevertheless, all cell numbers found in various CFD calculations have been within the interval of cell numbers observed during the tests.

Thanks to the unsteady pressure traverse it is also possible to compare the radial location of the unsteadiness. Figure 42 compares the unsteady pressure amplitude of the dominant cell pattern at a  $\phi$  of 0.06. It has to be pointed out that the amplitude between CFD and measurement cannot be directly compared due to the fact that all cell sets are measured,

whilst only a limited number is modelled in the CFD. The measured amplitude is therefore dependent on the time spent in one cell pattern. The ratio between the different cell patterns is not fully resolved by CFD due to the limited simulated time of about ten rotor revolutions. Despite this fact, the illustration allows a comparison of the radial distributions indicating the region of unsteadiness. The unsteady pressure has also been normalised to remove the effect of the fluid density and the different flow velocities as it has been defined in section 3.1.4.2. The two banded unsteady flow behaviour described earlier for the air model is especially measured in the downstream probe. Good agreement of the radial distribution is found between air model, steam model and the steam model CFD in the downstream traverse. For the air model CFD the lower peak is at lower span heights and weaker than the measurement. Possible reasons for this deviation have been discussed in the section 4.2.2. Similar deviation between CFD and measurement is found in the upstream traverse for the air model. Agreement is again found for the steam model with the peak pressure location in both cases at 90% span. It has to be pointed out that the location between stator and rotor is very narrow. The comparatively large pressure probe may lead to blockage modifying the unsteady pressure field.

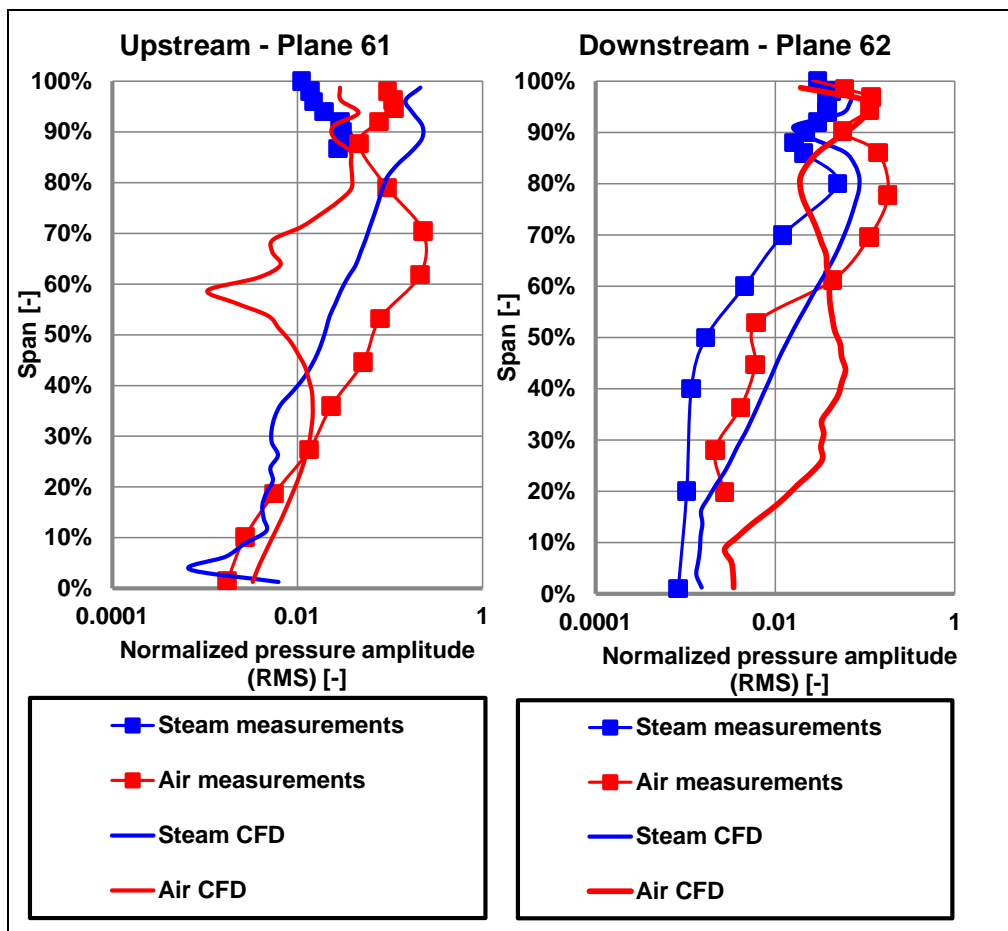


Figure 42: Unsteady pressure traverses for CFD and measurement, pressure amplitude of dominant cell pattern at  $\phi=0.06$

The CFD analysis permits an insight into the flow leading to this unsteady flow phenomenon. Figure 43 shows a conical cut of the passage and the separated flow field. As mentioned in the introduction, the flow enters the blade row with a highly negative incidence leading to a pressure side separation. Only in the tip region where the profile has almost no camber flow is attached on the pressure side. This is also the region where a rotating separation pattern first occurs when entering the ventilation zone. With a further reduction of the volume flow another fluctuation separation zone establishes itself on the suction side close to the trailing



edge, see Figure 43. Both regions are linked to each other in terms of frequency but are out of phase. In the separated flow regions the fluid is moved radially outwards. This effect is illustrated by the background contour in Figure 43. Whereas the separation system in the air and steam model is very similar lower levels of non-dimensional radial flow is present in the air model.

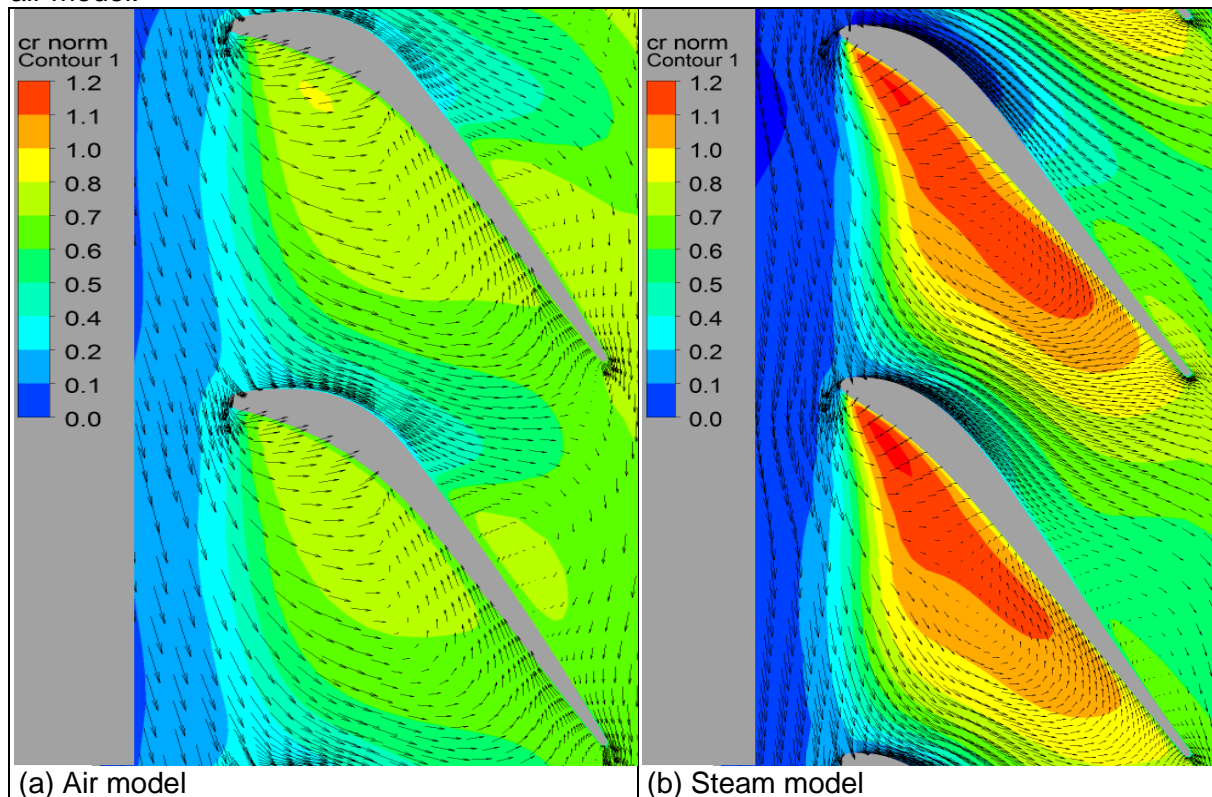


Figure 43: Blade-to-blade view at 70% span with radial velocity contour normalized with  $u_{hub}$  and projected flow vectors at  $\phi=0.06$  (profile geometry is indicative for confidentiality reasons)

In conclusion, both air and steam model turbine are presenting a similar time averaged and unsteady flow field at a given flow coefficient. The time instantaneous flow field in a blade-to-blade perspective is of a similar nature, too. This is the case despite the largely different geometry, with for example the blade count of the air model LSMB being  $\sim 40\%$  higher than the steam model turbine. It is very likely that both turbines are experiencing the same unsteady flow phenomenon. In addition, for both turbines the numerical modelling is able to capture the qualitative flow behaviour, with multiple stall cells rotating at a fractional speed of the rotor. However, for example to determine if the LSMB is operating out of resonance with the rotating stall to the natural blade frequency cannot be reliably determined with the CFD modelling. This is because the fractional speed of the rotating stall cells is in both cases over predicted by about 10%. This leads consequently to an unsteady forcing frequency in the relative frame of the rotor being 10% too high. This has indicated that most probably a more complex CFD modelling is required to account for effects, which are influencing the fractional speed of the stall cells relative to the rotor.

#### 4.4 Scale-resolving turbulence modelling

Standard engineering turbulence models are mainly developed for wall bounded non-swirling flow. The flow field under LVF operation is therefore challenging for these models. One option to approach this problem is to employ a turbulence modelling, which at least resolves larger turbulent structures preventing them being confused with larger coherent structures as it was discussed in section 3.2.5. The previous sections illustrated that with the URANS approach used there, the rotating stall phenomenon is captured but shows significant

discrepancy in terms of rotating frequency for the stall cells. In addition, the exact size and location of the separation zone is not perfectly captured. This could be associated with a short coming of the employed turbulence model. By using the existing CFD model the turbulent scale-resolving SAS-SST model (later referred to as SAS model) has been applied following the best practice guidelines provided by Menter [41]. No further computational grid density refinement has been applied. On the other hand, the time resolution has been increased by a factor of four to achieve a CFL number of approximately one as it is recommended in the best practice guidelines. The CFD calculation has been initialised with a converged URANS calculation employing the SST turbulence model, which simulated several rotor revolutions.

After the scale-resolving computation has been performed for sufficient rotor revolutions to obtain stable pressure and global mass flow signals, the time averaged flow field is compared in a first step. This is to check whether the different turbulence modelling has an effect on the global flow field. Figure 44 shows a traverse result downstream of the rotor of the steam model turbine. Comparing the URANS and SAS results small differences are visible in the large separation zone behind the rotor. The SAS slightly improved the agreement with the measurement in this region. On the other hand, the axial velocity close to the casing is still not well modelled as this is most likely related to the coarse mesh in the diffuser casing region to save some computational effort. Generally both turbulence modelling approaches capture the highly non-axisymmetric and separated time average flow field acceptably well.

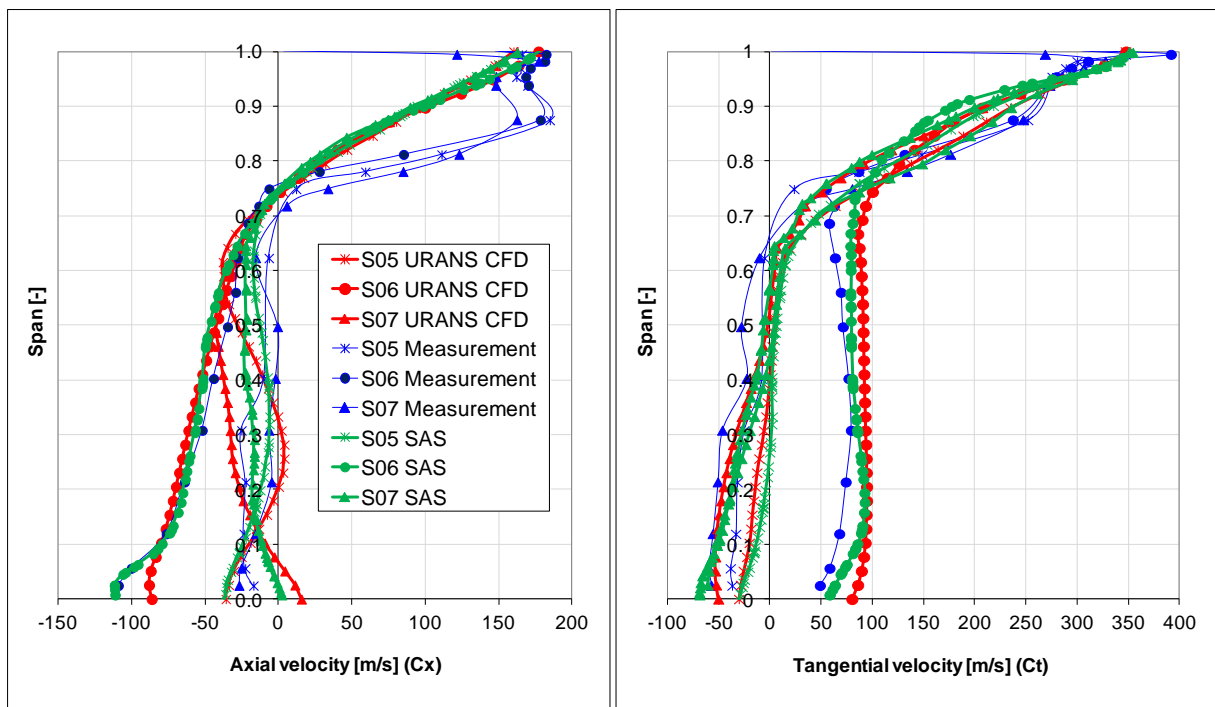


Figure 44: Spanwise distribution of time averaged flow velocity in the 62 plane of the steam model turbine

The SAS model can blend between a resolution of turbulent structures and a modelling of turbulence with the SST model as it was described in section 3.2.5. Therefore, the question arises whether turbulent structures have been resolved. Figure 45 compares the vortex structures in the exhaust of the steam model turbine between the URANS and SAS modelling. The vortex structures are detected using the Q-criterion, which is accounting for the strain rate and vorticity rate created by vortices. The URANS solution is resolving the large vortical structures linked to the separation zones in the exhaust. This is also underlined by the ring shaped appearance. A completely different result is obtained with the

SAS model. The model allows large turbulence structures to appear in the exhaust indicated by the worm shaped smaller vortices. The larger vortical structures of the separated region are not visible in this analysis, but still present as indicated by the radial traverse comparison.

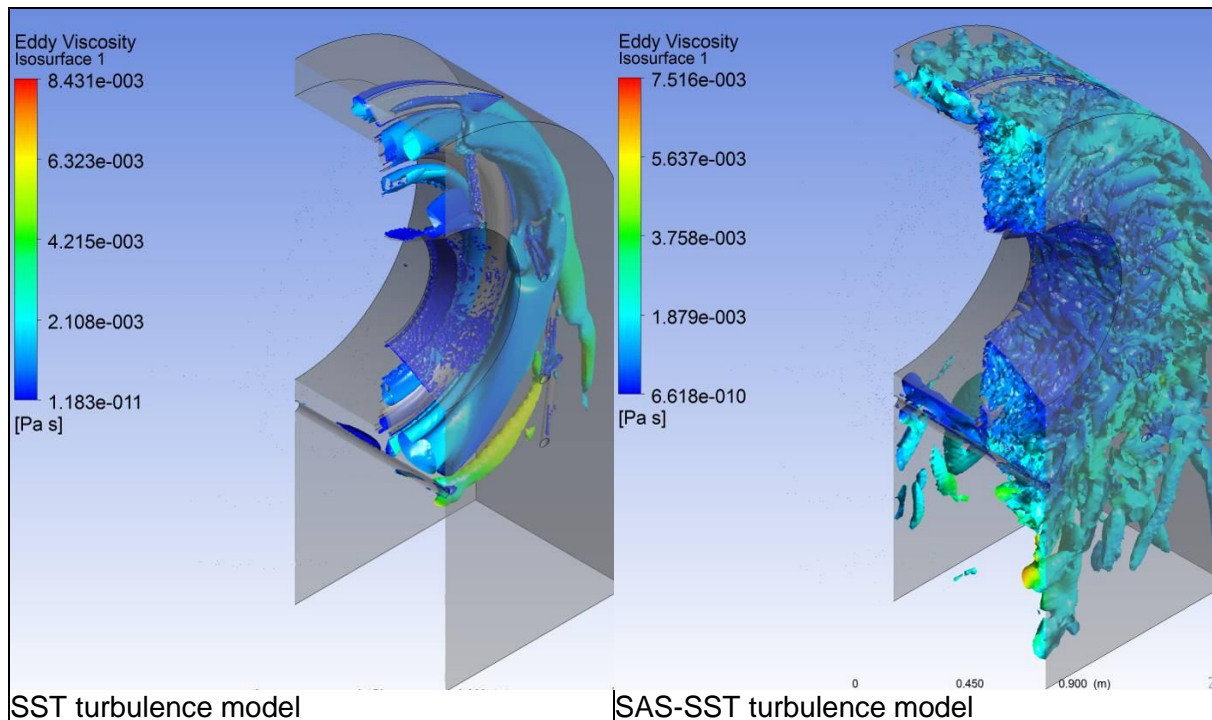


Figure 45: Iso-surface to detect vortex structures: Q-Criterion:  $Q = \Omega^2 - S^2$  ( $S = \text{Strain rate}$ ,  $\Omega = \text{vorticity rate}$ ) =  $10e7$ , eddy viscosity contour on the iso-surface

The influence of turbulence on the flow is modelled through the Boussinesq assumption, where the viscosity is artificially increased. With the SAS model some of the turbulent velocity fluctuation is actually resolved in the simulation. Consequently, less eddy viscosity needs to be added. Figure 46 compares the level of eddy viscosity between the two models in the last stage of the steam model turbine. The level of eddy viscosity is significantly lower with the SAS model allowing medium to large scale turbulent structures to occur.



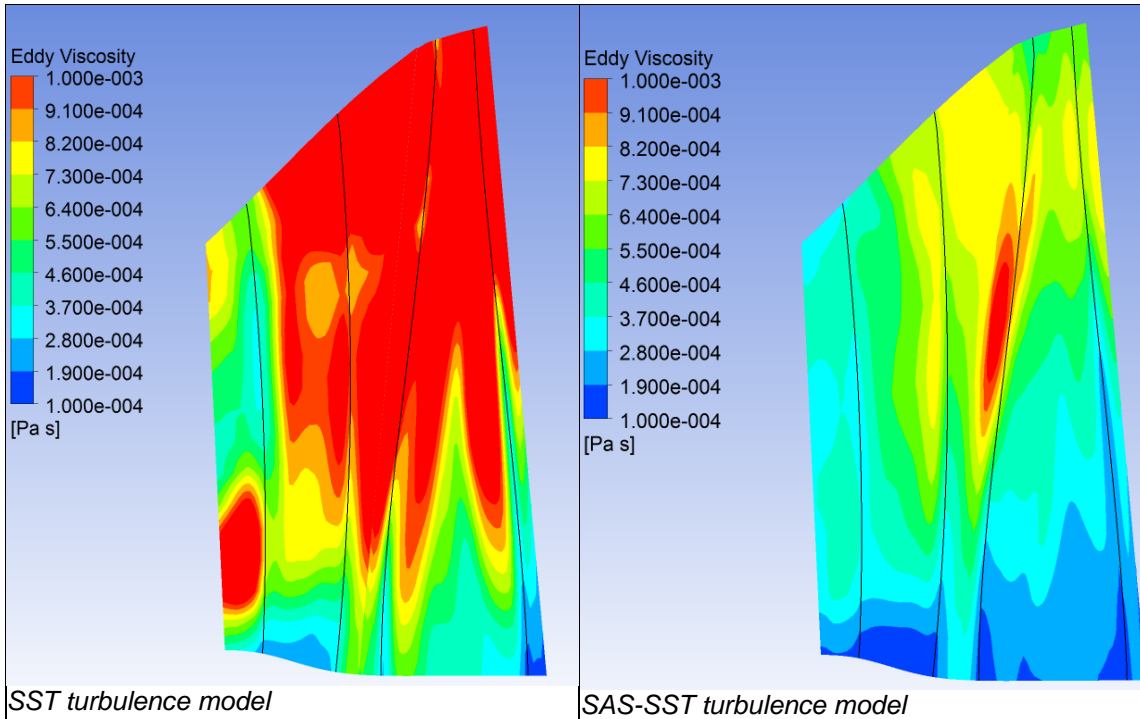


Figure 46: Circumferentially averaged eddy viscosity in a meridional plane of stator and rotor, steam model turbine

Figure 47 illustrates the time history of a pressure monitor point between stator and rotor. The calculation with SST turbulence model has been run for 7 rotor revolutions under constant turbine operating conditions. To observe changes in the frequency domain a FFT window with a size of two rotor revolutions has been moved with 0.2 rotor revolution increments through the time series. This approach reveals more information in time at the cost of frequency resolution, because the FFT window is smaller compared to using the whole time trace. On the high frequency side, the rotor blade passing is visible corresponding to 63 rotor blades. A large band with very low pressure fluctuations is present between frequencies of about 3-4 times the shaft rotating frequency.

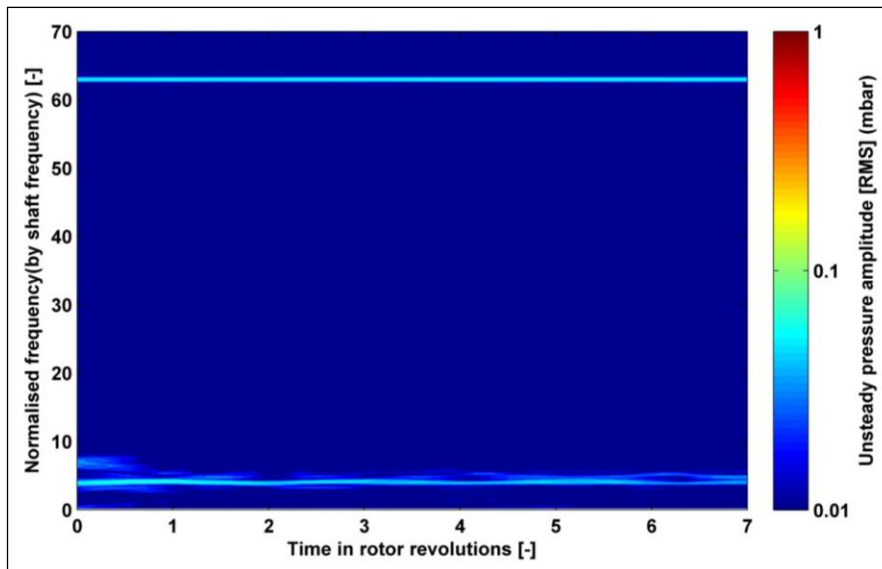


Figure 47: Time moving FFT for a pressure monitor point between stator and rotor at 87% span, SST turbulence model, steam model turbine

An entirely different situation does occur in the SAS simulation, see Figure 48. Over the whole frequency band plotted a higher level of unsteady pressure fluctuations are present. Again, two frequency regions with coherent signals are found. A stronger blade-passing signal is present as compared to the SST simulation. In addition, an interference between the rotating stall cells is visible. The rotating stall signal is by a factor of 10 stronger than in the SST simulation. In addition, a low and high stall cell pattern can be seen indicated by the nearly continuous two red lines. Not only the general background noise generated by turbulent fluctuations is elevated, especially in the frequency range of the rotating stall a base of high turbulent fluctuations is simulated. This effect has also been reported by Gerschütz [36] and Truckenmüller [15].

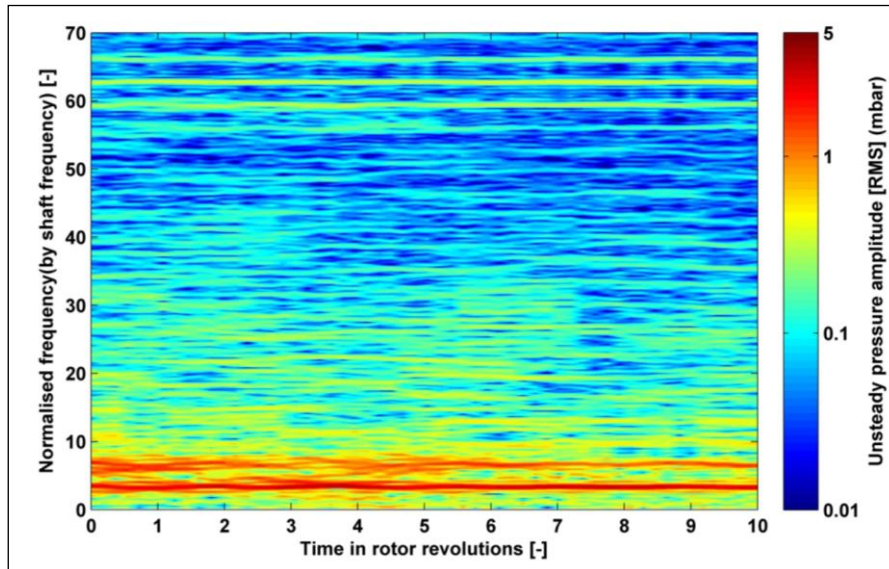


Figure 48: Time moving FFT for a pressure monitor point between stator and rotor at 87% span, SAS turbulence model, steam model turbine

Figure 49 shows a zoom in of the previous contour plot allowing a more detailed look into the unsteady behaviour of the stall cells. As it was discussed in the literature review, the number of stall cells is varying over time stochastically, while maintaining the fractional speed to the rotor. This leads to the characteristic equally spaced lines in the frequency domain indicating the different integer stall cell counts. Within the time moving FFT presented transitions between different cell counts are smeared out to a certain extend but are still visible. The strong signal at around 3.2 of the rotating frequency is related to a seven cell stall system. With a fractional speed of about 48% signs of the six and eight cell system are visible at  $\sim 2.7$  and  $\sim 3.7$  of the rotating frequency.

In the first three to four rotor revolutions the cell system seems still to change as the global parameters are not fully settled. Beside the low frequent cell system a high frequent system is present between six and seven times the rotating frequency which can be identified as a 13 or 14 cell stall cell system. The system is weaker and more intermittent. This type of higher frequency cell system has also been found in the measurement and will be discussed later.

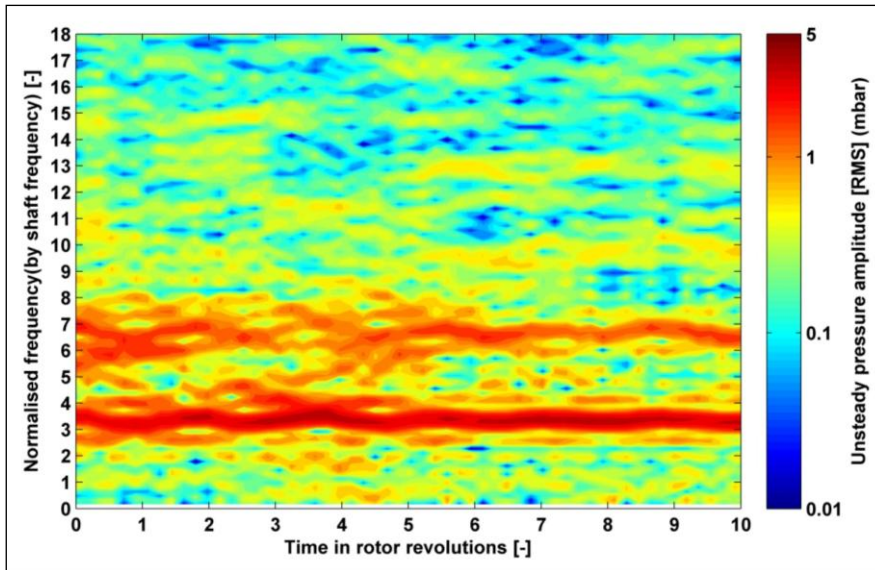


Figure 49: Time moving FFT for a pressure monitor point between stator and rotor at 87% span, SAS turbulence model, steam model turbine

In Figure 50 the same post-processing has been applied to a measurement result at the same location. Unlike the CFD simulations many rotor revolution can be recorded in the measurement. On the other hand, the sampling frequency is 20 times smaller as compared to the SAS simulation. This allows the displaying only up to 18 times the rotor rotating frequency, but this covers the region of interest. The measurement signal also contains a higher level of background turbulent fluctuations being highest for lower frequencies. A coherent signal is found for 3.2 and 3.7 times the rotor rotating frequency, which corresponds to the rotating stall cells.

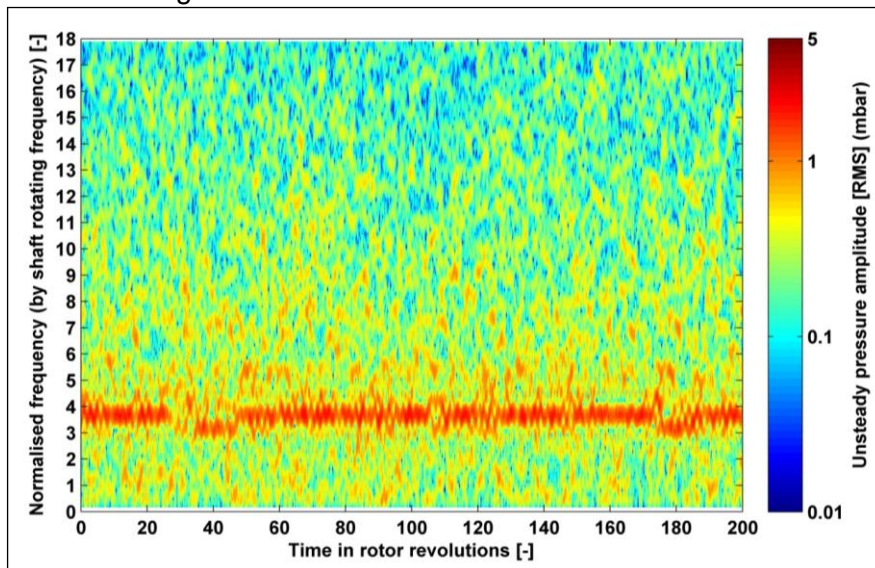


Figure 50: Time moving FFT of an unsteady pressure signal of the steam model turbine recorded at 87% span between rotor and stator, steam model turbine

Figure 51 is a zoom in of Figure 50 showing the first 10 rotor revolutions. It can be qualitatively compared with the 10 rotor revolutions computed with CFD. Comparable background turbulent fluctuations are present in both results. The signal of the seven stall cells is clearly visible with some indication of six and eight. In the sampled measurement window the higher order stall cell system only appears in distributed patches. Later it will be shown in Figure 52 that a sampling over 7500 rotor revolutions reveals that also in the

measurement the higher order stall cell system is present as it was found in the measurement.

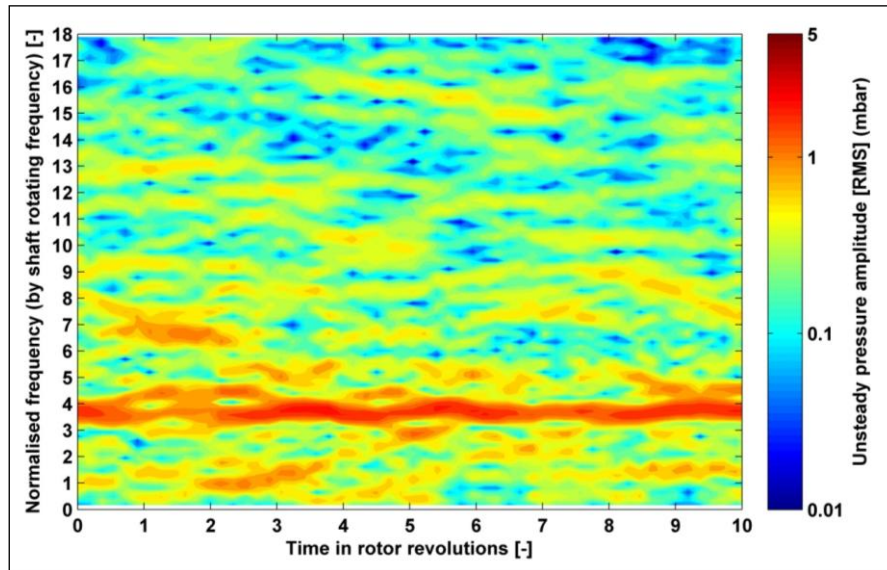


Figure 51: Zoom-in: Time moving FFT of an unsteady pressure signal of the steam model turbine recorded at 87% span between rotor and stator, steam model turbine

Figure 52 compares the two turbulence models as well as the measurement in a frequency spectrum versus span in a plane between stator and rotor. The SST results confirm the low activity with some weak indication of rotating pressure disturbances. High amplitudes associated with the rotating stall cells are SAS-SST found over the recorded span height with the SAS model. The frequency of the low order cell pattern is in line with the measurement results. The higher cell count signal between five and eight times the rotating frequency is at higher frequencies as the measurement. This is linked with the fact that the flow coefficient between the measurement and the CFD is not perfectly matched. This influence will be discussed in the following section. Similarity in background turbulent fluctuations is found although a finer frequency resolution for the CFD results would require many more rotor revolutions to be calculated.



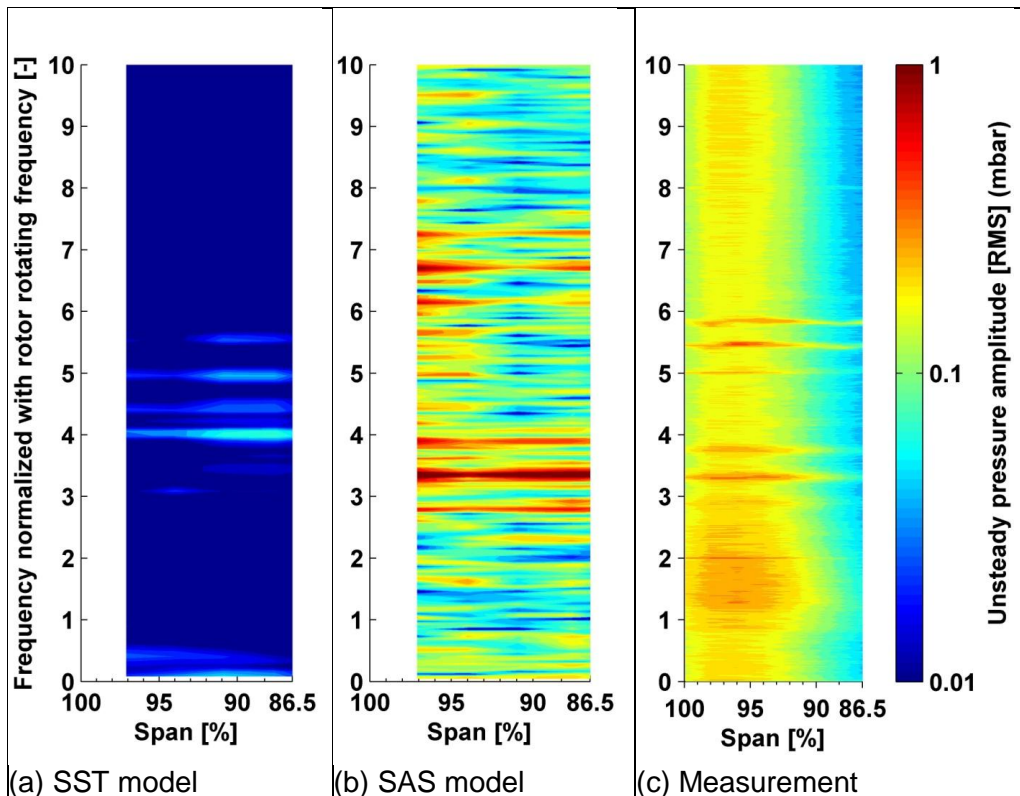


Figure 52: Unsteady traverse measurement plane 61 (between stator and rotor), steam model turbine

The SAS scale-resolving model is better than the standard engineering turbulence model to capture the stall cells in terms of pressure amplitude, cell numbers and fractional speed to the rotor. As discussed in the section 3.2.5 it is likely that the large scale turbulent fluctuations and the coherent stall cell pressure fluctuations are dissipated by the high levels of eddy viscosity resulting from the URANS approach employing the SST turbulence model. Scale-resolving modelling is therefore used for better prediction of the unsteady flow field.

#### 4.5 Flow coefficient influence

The flow coefficient is the most important parameter, which defines the operating regime and flow behaviour under LVF conditions. The rotating stall phenomenon appears in a defined range of flow coefficients regardless of the pressure level as it was found in the presented measurement campaign as well as in literature. The characteristic nature of the rotating stall phenomenon itself is also dependent on the volume flow. Figure 53 illustrates the fractional stall cell speed against the flow coefficient for the steam model turbine. The measurement indicated a slight reduction of the fractional speed with an increase in volume flow. A similar trend is predicted with the CFD computation employing the SAS model. Although this gradient is relatively small, it is important as it defines the range of frequencies in the relative frame. If for example the fractional speed varies by  $\sim 0.05$  and two cell numbers are present the whole frequency band between two engine orders (multiples of the rotating frequency) can be excited. On the other hand, a high gradient will lead to excitation only in a very narrow flow coefficient range. Gerschütz [36] and Truckenmüller [15] for example observed excitation only in a relative volume flow band between 13% and 14%.

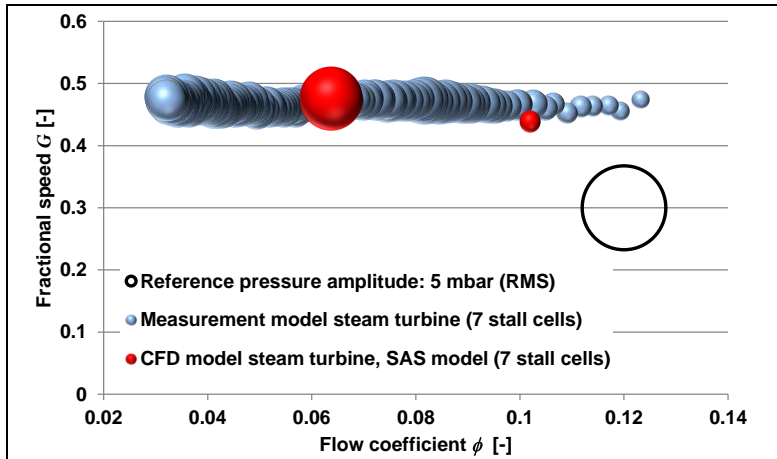


Figure 53: Flow coefficient versus fractional speed and pressure amplitude at the casing between stator and rotor plane 61, low frequency stall pattern, steam model turbine

For the steam model turbine investigated a second higher order set of rotating stall cells has been observed. Unlike the lower order cells a higher gradient in fractional speed is observed, see Figure 54. For the calculated higher flow coefficient point no signal has been detected for higher cell numbers in the measurement. However, a high order cell pattern was present in the CFD computation following the trend of the measurement results in terms of fractional speed.

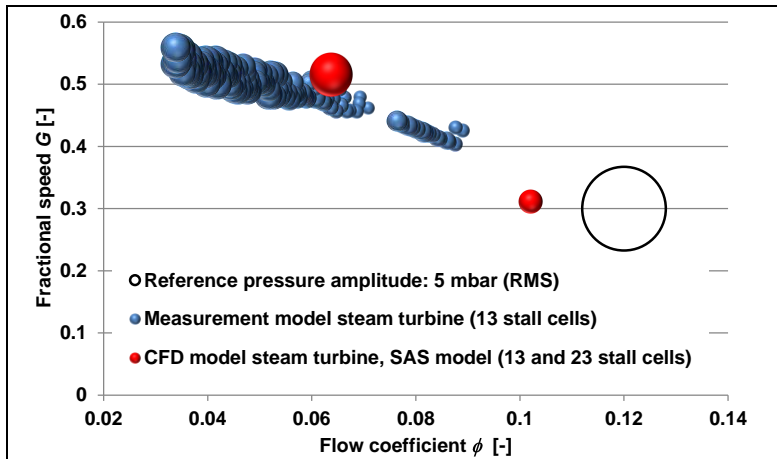


Figure 54: Flow coefficient versus fractional speed and pressure amplitude at the casing between stator and rotor plane 61, high frequency stall pattern, steam model turbine

Figure 55 shows the unsteady pressure traverse results for the two flow coefficients calculated as well as the measurement results. For the higher volume flow the unsteady pressure fluctuations are reducing in intensity. The radial extent of the fluctuations is also reduced, still two regions of unsteadiness are present. The measurement result is at a flow coefficient between the two CFD simulations in terms of stall cell strength as well as turbulent background fluctuations. Beside the two cell systems a region of higher unsteadiness between one and two time the rotating frequency is present which is not resolved by CFD. Below 90% span the amplitudes of the unsteadiness is dropping rapidly, this is also found for the higher flow coefficient CFD calculation.

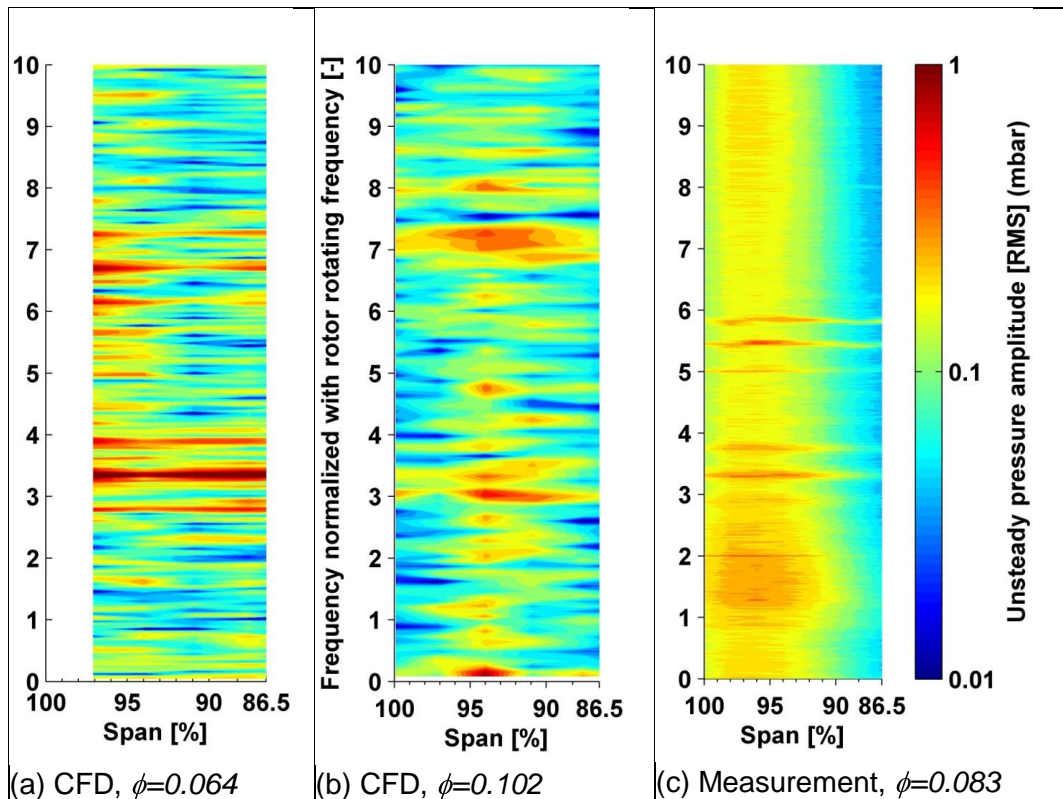


Figure 55: Unsteady traverse measurement plane 61 (between stator and rotor), steam model turbine

In the measurement, the fractional speed of the stall cells is dependent on the flow coefficient. This trend is also captured by CFD for the steam model turbine, although the exact gradient is not reproduced. Due to the relative small changes of the low cell count stall it is difficult to understand what is driving these changes. This effect may be related to the individual LSMB blade design. This theory is supported by the fact that the air model turbine is presenting an opposite gradient as compared to the steam model turbine, see Figure 56. The CFD computation employing the SAS scale-resolving model predicts the cell fractional speed well. As reported earlier, computations with the SST turbulence model significantly over-predicts the fractional speed, but have shown to resolve the trend at slightly higher fractional speeds with higher flow coefficients.

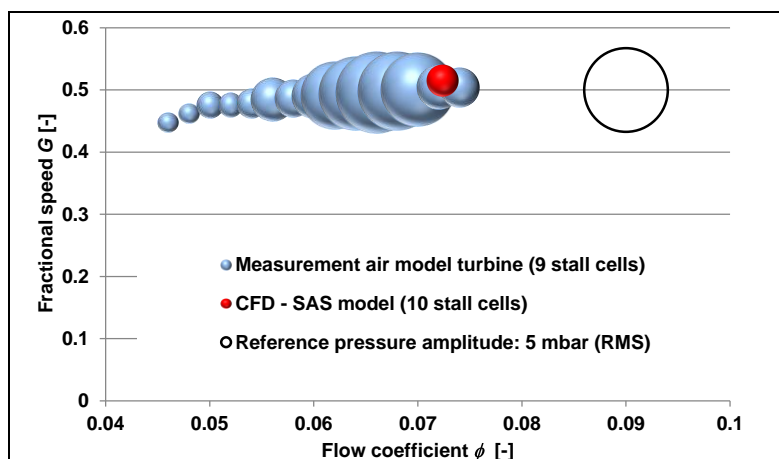


Figure 56: Flow coefficient versus fractional speed and pressure amplitude at the casing between stator and rotor, air model turbine

## 4.6 Tip gap influence

The unsteady flow structure of the rotating stall is located relatively close to the casing of the turbine. Typical LMBS feature a sizable radial clearance to prevent rubbing at the casing and account for a differential expansion especially with a flared tip as it is designed in the steam model turbine. In the initial studies, the tip gap above the LSMB has been omitted to reduce the computational effort. In a first step, a tip gap has been applied to the air model turbine computation employing the SST turbulence model. The same radial tip gap size has been selected as it is found in the model turbine of 1 mm. This corresponds to realistic tip gap size, as it would be found scaled in a full size machine. After several rotor revolutions of the calculation it became apparent that changes of the unsteady flow field and frequency data was minor. Particularly the fractional speed of the stall cells is still too high and similar to the mode without tip gap. This leads to the conclusion that similar effects may be experienced in the steam model turbine. As a feature of the steam model turbine with the flared LSMB tip, the radial clearance is not as well defined as in the model air turbine. With the differential expansion due to the thermal effects under LVF the tip gap varies slightly during operation between  $2.1 \pm 0.2$  mm (hot/no cooling spray water) and  $2.4 \pm 0.4$  mm (cold/cooling spray water on) in the steam model turbine. Therefore two tip gap sizes of 1.5 mm and 3 mm were investigated with CFD, which are extending the real range of tip gap sizes and the variation expected in full size LP turbines. Unlike the air turbine significant effects have been observed for the steam turbine model by introduction of the tip gap while employing the SST turbulence model.

Figure 57 illustrates the frequency content of the unsteady pressure signal between stator and rotor for the computation with SST turbulence mode. The introduction of a tip gap has a sizable effect on the unsteady pressure field by changing both the frequency and amplitude content. The stall cell count as well as the fractional speed is dropping. In terms of pressure amplitude, the anyway low levels found in the SST turbulence model investigation are reduced further with the 3 mm tip gap to a level where it is difficult to detect any low frequency disturbance linked to a rotating pressure field disturbance.

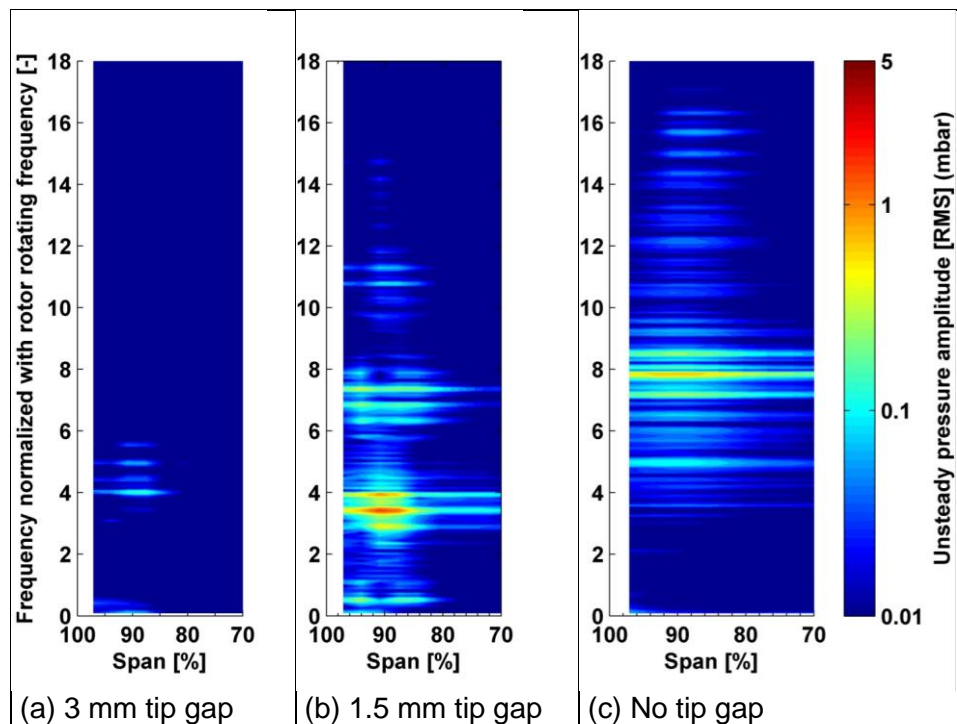


Figure 57: Unsteady traverse measurement plane 61 (between stator and rotor), CFD SST turbulence model, steam model turbine



Simulation using the SAS scale-resolving model presents a completely different result. For all three configurations two groups of stall cells are present, which are comparable in strength for the low frequent cells set, see Figure 58. Due to a shorter run time of the no tip gap case a reduced frequency resolution is presented slightly smearing out the high pressure peaks. Above 95% span the effect of the tip leakage flow is visible introducing an increased amount of disturbances for the 3 mm tip gap case.

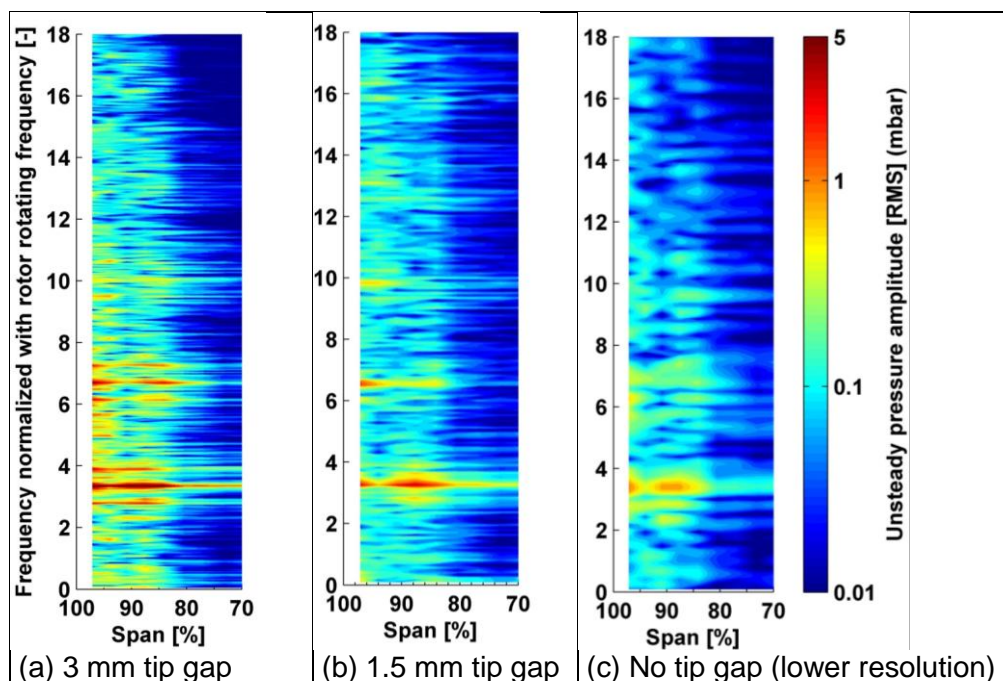


Figure 58: Unsteady traverse measurement plane 61 (between stator and rotor), CFD SAS turbulence model, steam model turbine

Interestingly, the difference between the two tip gap sizes is relatively minor, but not modelling a tip gap has some effect on the prediction of the unsteady pressure amplitude and the fraction speed of the stall cells, see Figure 59. In the simulation, the leakage flow seems to slow down the stall cells tangential velocity reducing the fractional speed by 0.012. A further increase of the tip gap again increases the fractional speed slightly. The measured fractional speed is between the computed fractional speeds for the cases including a tip gap giving good confidence in the results, even though a similar investigation was not undertaken in the test turbine.

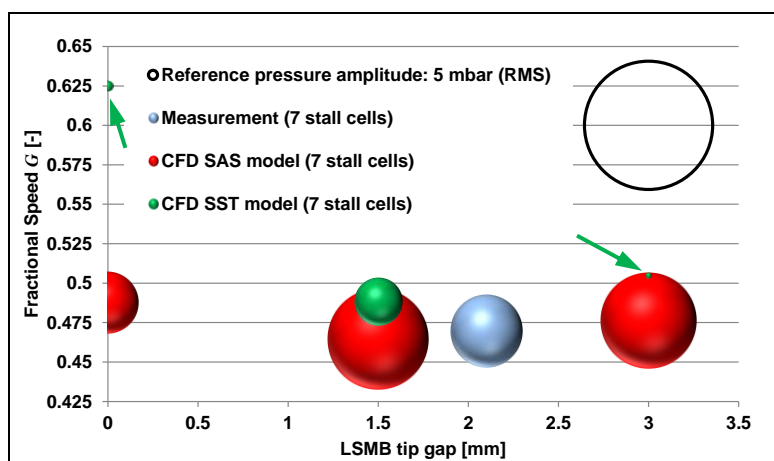


Figure 59: Flow coefficient versus tip gap size and pressure amplitude at the casing between stator and rotor plane 61, steam model turbine

The SST turbulence model does not sufficiently resolve the unsteady pressure field, while being unrealistically influenced by the tip gap size. The SAS scale-resolving model presents a consistent set of relatively strong stall cells for all three cases (no tip gap, 1.5mm tip gap and 3mm tip gap). It is clear that the fractional speed is slightly affected by the tip gap size, but the rotating stall phenomenon is not caused by the tip leakage as it was suggested by Gerschütz [14].

## 4.7 Exhaust influence

It was already mentioned that the steam turbine model required a realistic exhaust geometry for the stall cells to be present in a realistic strength when employing the SST turbulence model. This leads to the conclusion that the exhaust geometry is very important for the correct modelling of the rotating stall phenomenon. Typical steam turbine application can employ many different exhaust types especially when existing power plants are upgraded with a new rotor and inner casing while maintaining the outer casing. As well as the unrealistic symmetric exhaust type also two realistic exhaust geometries have been investigated, see Figure 60. For both realistic geometries, measurement data is available from the steam model turbine. During the measurement campaigns, it was observed that the exhaust geometry has significant impact on the unsteady flow behaviour.

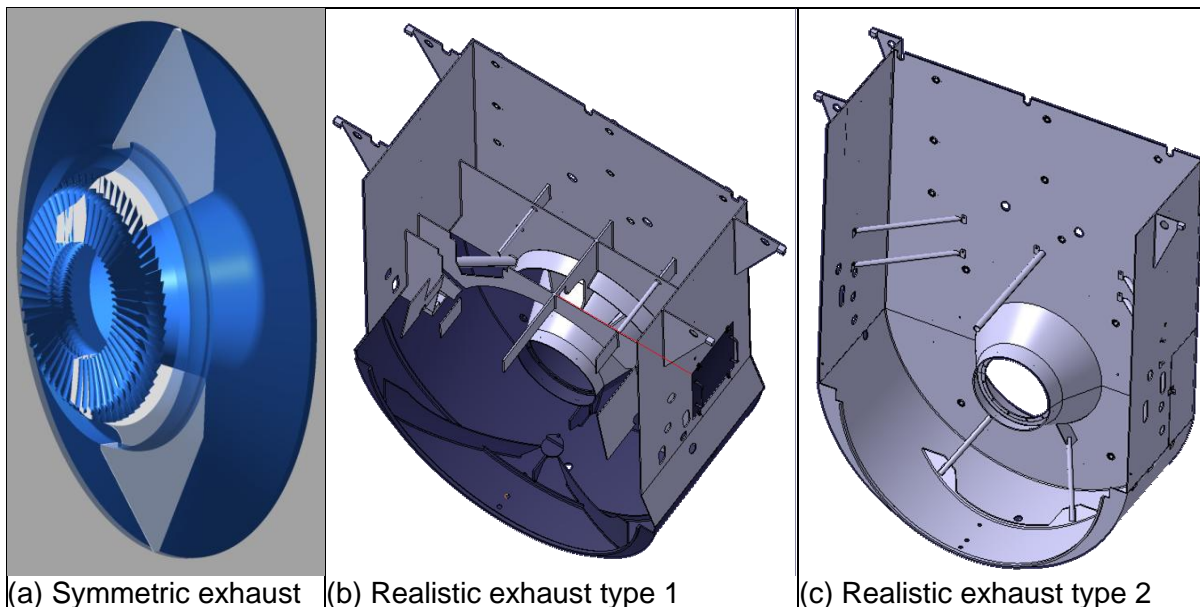


Figure 60: Different exhaust configurations for the steam model turbine

Figure 61 compares the time history of a pressure monitor point for the two exhaust variants. For exhaust type 1 a strong seven cells stall system is formed after less than two rotor revolutions, the second exhaust type shows weak signs of an instability developing but no consistent signal. It is also noticeable that the level of turbulent fluctuations of the complete displayed frequency range is lower. It can be concluded that the more compact exhaust type 2 leads to significantly lower pressure fluctuations by the rotating stall.

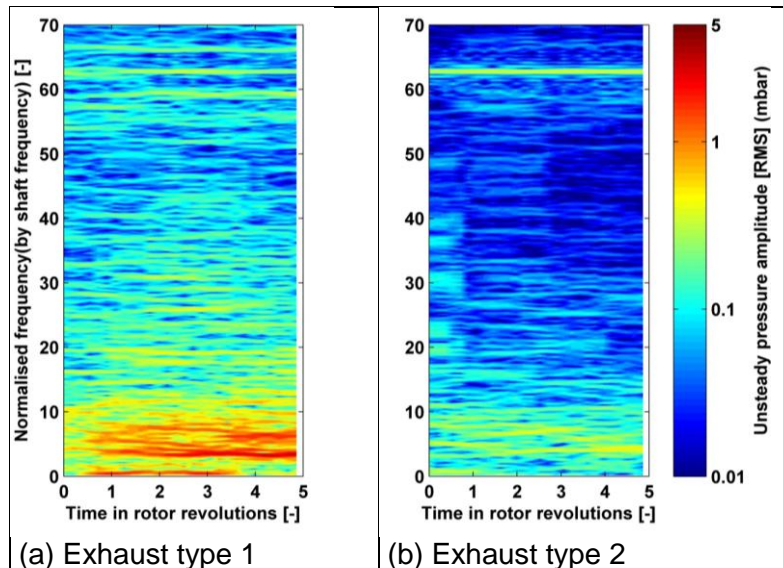


Figure 61: Time moving FFT for an unsteady pressure monitor point (between stator and rotor), CFD SAS turbulence model, no LSMB tip gap, steam model turbine

The low levels of flow unsteadiness that may be attributed to low frequency stall cells are confirmed by unsteady pressure measurement data, see Figure 62. Whereas the exhaust type 1 shows clear indications of a group of stall cells visible as individual peaks, the exhaust type 2 does not include significant unsteady pressure signals that could be linked to low frequency stall cells, which could excite the LSMB. The larger peak visible for the exhaust type 2 at 5.2 times the rotating frequency could not be linked to a rotating pressure disturbance. The low level of activity for both exhaust types is linked to the measurement location at the casing. Unfortunately not traverse data has been recorded for exhaust type two. Nevertheless, the strain gauge signal did confirm the absence of significant low frequent stall cells.

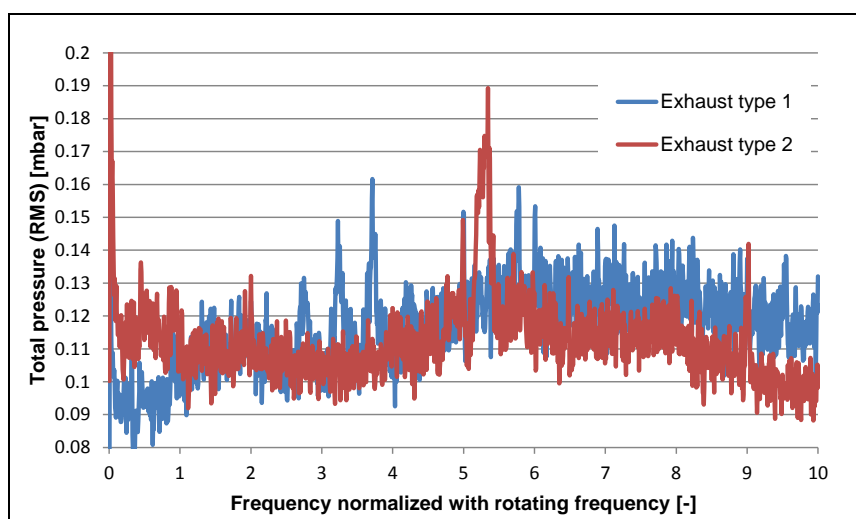


Figure 62: Unsteady pressure signal at the casing between stator and rotor, plane 61, measurement, steam model turbine

Most likely these differences are caused by the changes in the separated flow field in the exhaust system. Figure 63 shows the circumferential velocity of the flow downstream of the LSMB. In particular, the flow returning to the LSMB in the large separation region is sizably different between the two exhaust types. The more compact exhaust type 2 presents a much higher swirling component in the separation region changing the inflow to the LSMB. The more distorted flow field in the exhaust type 1 is even showing regions with rotation against the rotor rotation. These changes in the flow field are expected to change the unsteady behaviour of the stall cells. It can also be concluded that the used CFD modelling is resolving these effects by reducing the unsteadiness for the exhaust type 2.

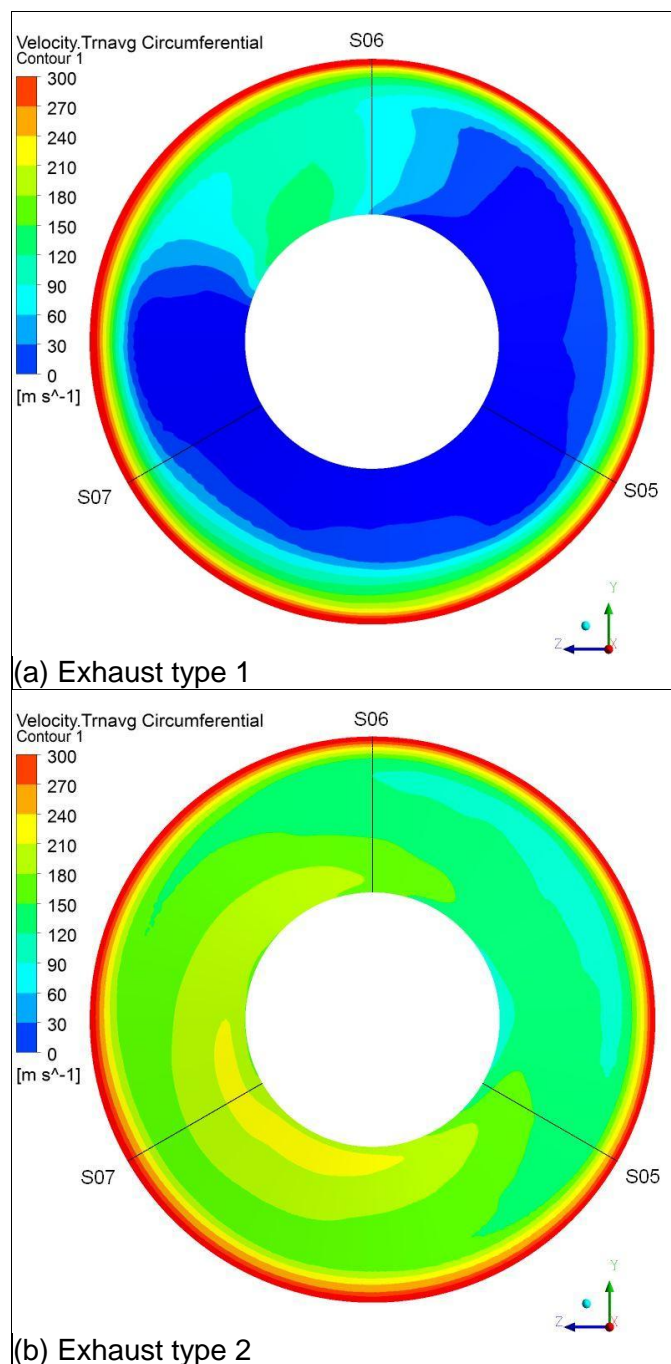


Figure 63: Circumferential velocity downstream of the LSMB, plane 62, CFD time averaged, steam model turbine



## 4.8 Flow physics and stall cell propagation mechanism

In section 2.2.5, it was stated that the rotating disturbance observed in LP steam turbines under LVF operation can be classified as rotating stall or more particularly part-span rotating stall. This statement has been based on the findings in open literature, which have been developed using measurements to investigate the phenomenon. It has been demonstrated in the previous chapter that with the correct CFD modelling the characteristic unsteady flow phenomenon can be reproduced. This allows a deeper insight to the actual flow physics.

Figure 64 illustrates the unsteady pressure amplitudes on the blade surface of the steam model turbine. The amplitudes extracted are associated with seven disturbances around the circumference. This means other pressure fluctuations related to stationary engine order disturbances are filtered out and the sole effect of the seven stall cells is visible. As expected from the traverse results the main region of unsteadiness is in the upper 50% of the blade.

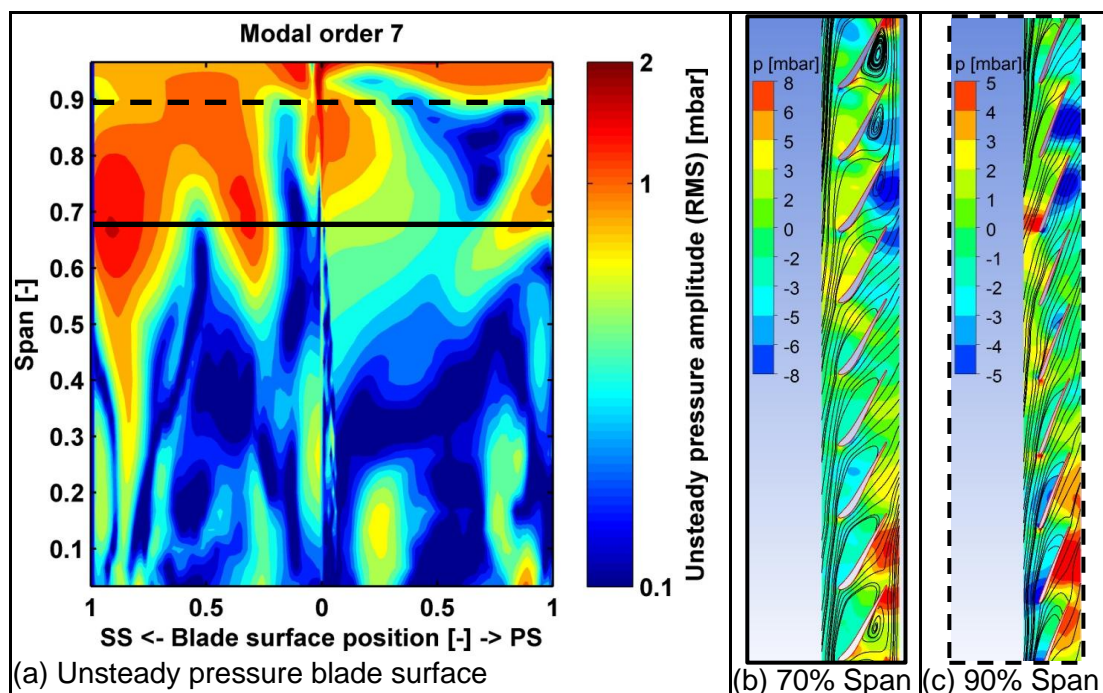


Figure 64: Left: Unsteady pressure distribution (CFD) on the blade surface caused by seven stall cells; right, instantaneous blade-to-blade view illustrating the separation region and pressure variation from the time average, CFD SAS model, steam model turbine (profile geometry is indicative for confidentiality reasons)

The region with the highest pressure fluctuations caused by the stall cells is located on the suction side close to the trailing edge between 60% and 80% span. A blade-to-blade view in Figure 64 (b) illustrates that this pressure fluctuation is associated with a large alternating separation region which is blocking the passage. With a stall cell extending over nine passages the following stall cell is visible at the bottom of the diagram Figure 64 (b). The contour plot is showing the pressure deviation from the time averaged pressure field. It can be observed that the initiation of the separation is associated with a low pressure field relative to the time average whereas the vanishing of the separation zone leads to higher pressure levels. Another region of unsteadiness caused by the rotating stall cells is located at a similar span height again on the suction surface but further upstream between 0.3 and 0.4 normalised blade surface position. It is roughly the region from where the flow starts to separate if a stall cells is present. It is also the region with highest curvature being the guided part of the passage. Along with the suction side separation, the pressure side separation zone also increases in size but never vanishes. The remaining inlet flow, which is now entering the passage with the highest incidence angle, leads to a small increase in

pressure, which is visible on the top two blade sections, Figure 64 (b). A different situation is found in the top 20% of blade span height. The smaller region of unsteadiness on the suction side is reduced in strength and wider, whereas the major separation on the suction side is not present as in the 70% span height region. The blade-to-blade view at 90% span in Figure 64 (c) illustrates that these changes are linked to the typical changes of the highly twisted LSMB sections. The sections at this height have little to negative section camber and a higher stagger angle favouring the flow angles under LVF resulting in lower negative incidence. This allows the flow to attach temporarily on the pressure side. The flow is then turned towards the machine axis representing compressor operation leading to a pressure rise. Consequently, a smaller region of unsteadiness is located at the pressure side close to the leading edge where the flow separates as a stall cell passes by. Close to the blade tip above 90% span, the blade surface pressure is likely to be influenced by the leakage flow, which is in opposite direction compared to design operation from suction to the pressure side as the turbine operates in compressor mode.

Figure 65 adds the phase angle corresponding to the blade surface unsteady pressure distribution. A threshold of 0.6 mbar unsteady pressure amplitude has been used for the phase plot where regions below that value appear in blue. Interestingly the large region of unsteadiness at the suction side close to the trailing edge is around 180° out of phase with the smaller unsteady region further upstream on the suction side. This illustrates that under stalled conditions the low-pressure region is associated with a high pressure region closer to the leading edge between 60 and 75% span. An alternating behaviour is also observed right at the leading edge between 75 and 90% span along with the separation from the pressure side. The suction side surface between 80 and 90% is showing lower phase angles lagging behind the largest region of unsteadiness around 70% span at the suction side trailing edge region. This is also an explanation for the two-banded unsteadiness recorded by the traverse measurement, which has been reported for the air and steam model turbine, see section 4.3.4.

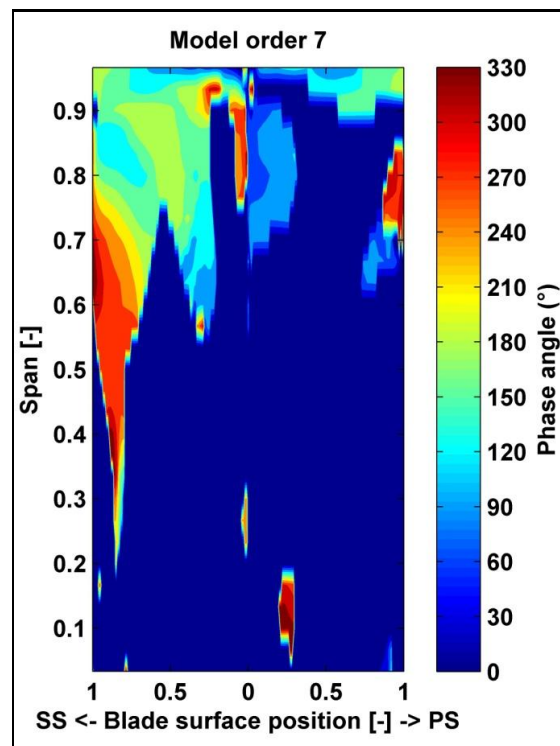


Figure 65: Corresponding phase to Figure 64 with a 0.6 mbar threshold, CFD, SAS model, steam model turbine

On the blade surface as well as in a blade-to-blade view the flow is found to be highly complex. Similarities to classical rotating stall in axial turbines can be found because individual passages are blocked which consequently leads to a changed inlet flow angle to the neighbouring passage. The situation is complicated by two factors. Firstly, the blade geometry of a LSMB changes significantly over height. Lower span sections are characterised by high camber profiles with lower stagger angles making attached flow on the pressure side impossible under LVF. More similarities to axial compressor flow are observed above 80% span where the profiles have a low camber and high stagger angle. Secondly, these illustrations do not describe the large radial component of the flow, which is the dominating part of the flow vectors under LVF operation.

A plane perpendicular to the machine axis between stator and rotor is presented in Figure 66. The first observation is that the main region of through flow is confined to a band between 70% and 90% span. The large blue coloured region close to the casing is marking the upper half of the casing vortex with negative axial velocities. It can be observed how the casing vortex increases in size and then diminishes between 40° and 50° theta. This change is linked to changes to the inflow at lower span sections as described earlier. Regions of increased axial velocity are found between 20° and 40° theta.

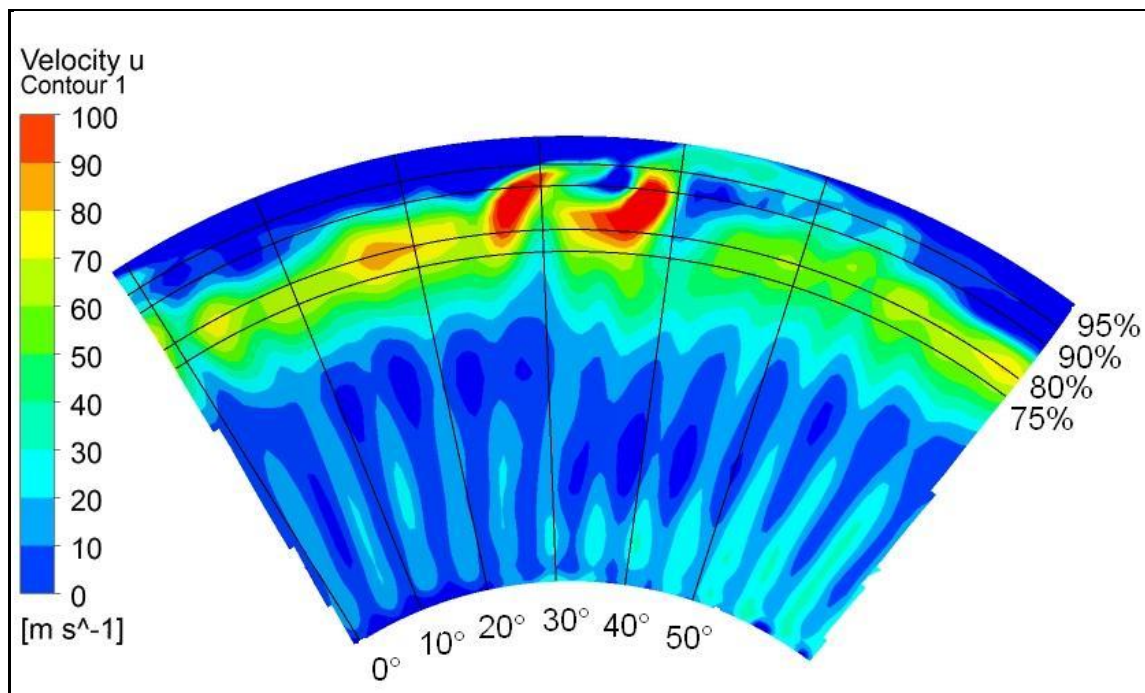


Figure 66: Plane perpendicular to the machine axis at a 50% axial location between stator trailing edge and rotor leading edge, CFD SAS model, steam model turbine

Figure 67 illustrates the flow field in meridional planes for different circumferential positions. With seven stall cells the flow situation repeats approximately after 51° in the tangential direction. Six cuts show the circumferential velocity as contour and the streamlines based on the radial and axial flow vector component in the meridional plane. Because this is a result of a transient simulation, the streamlines are a family of curves, which are tangent to the instantaneous velocity vectors and should not be confused with path lines, which show where particles travel in time. The planes are at fixed theta positions sampled at the same time instance cutting randomly through the blades visible by the white areas between the leading and trailing edge positions. This is no problem because the focus is on the inter-blade space between stator and rotor, which is affected by the stall cell. At the first angular position, Figure 67 (a), the flow in the region of the stall cells between 70 and 100% span



has a positive axial flow component entering the rotor above this height. The axial velocity component is very low under these conditions. The tangential flow velocities in the axial gap are significantly lower than the blade tangential velocity. Both effects lead to the highest negative incidence to the rotor blade. In the second plane, Figure 67 (b), the flow starts to reverse close to the casing forming the casing vortex. This results in a reduction of through flow area in the axial gap slightly increasing the axial velocity. Additionally, the fluid moved upstream has a high tangential velocity leaving the rotor blade passage with increased tangential momentum. In Figure 67 (c) the casing vortex reaches its maximum size. The inflow to the rotor blade passage at around 70 to 80% span is significantly changed due to the high tangential velocity of the vortex and the further increased axial velocity. The reduced negative incidence leads to flow passing the rotor more axially with reduced or vanished separation regions on the suction and pressure side. Less flow is consequently transported radially outwards in the separation zones. As less flow is arriving at the blade tip the casing vortex starts to diminish as it can be observed in Figure 67 (d). In Figure 67 (e) the casing vortex collapses with some remaining recirculation close to the stator trailing edge. In Figure 67 (f) the next stall cell starts with a flow field very similar to the initial situation in Figure 67 (a). It can be concluded that the alternating two banded separation in the bladed zone described earlier is directly coupled with a torus vortex that appears intermittently at the blade tip.

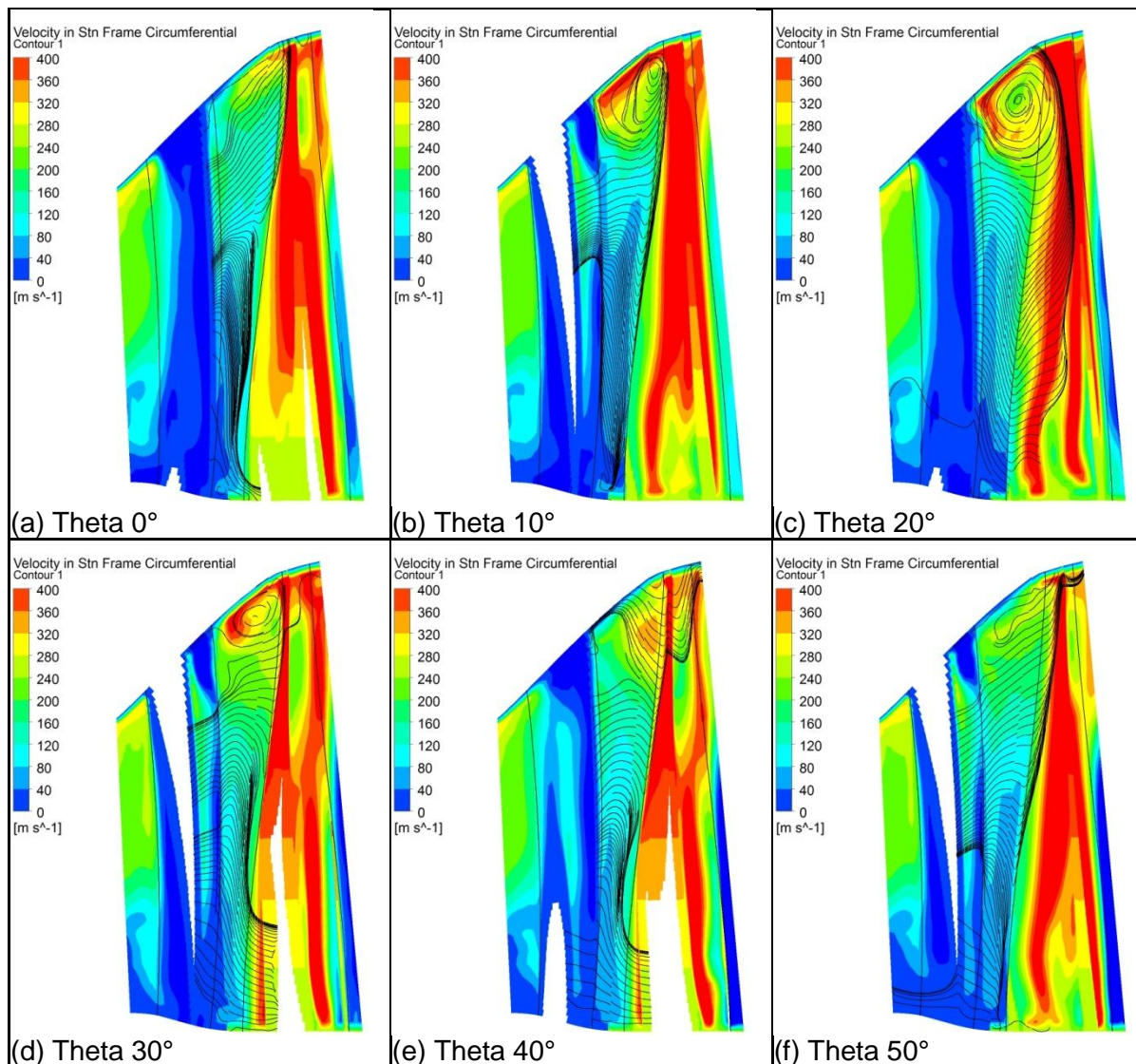


Figure 67: Meridional cuts at different theta positions, CFD SAS model, steam model turbine



Figure 68 is illustrating the axial velocity for different span heights. As described earlier the flow towards the rotor blade is always in positive axial direction up to approximately 85% span. Nevertheless, Figure 68 (a) and (b) show that the inflow to the rotor is perturbed in the theta range between 10° and 40° where a casing vortex is present. Locally the axial velocity is increased in confined regions most probably split by the stator blades influence. At 90% span, see Figure 68 (c), flow is leaving some rotor passages upstream. Larger regions of high axial velocity are visible which are affecting the inflow at lower span sections as they are transported towards the hub by the casing vortex. Close to the casing at 95% span, see Figure 68 (d), fluid flows upstream nearly reaching the stator trailing edge between 0° and 30° theta position. Fluid is still transported downstream in passages between 30° and 50° theta.

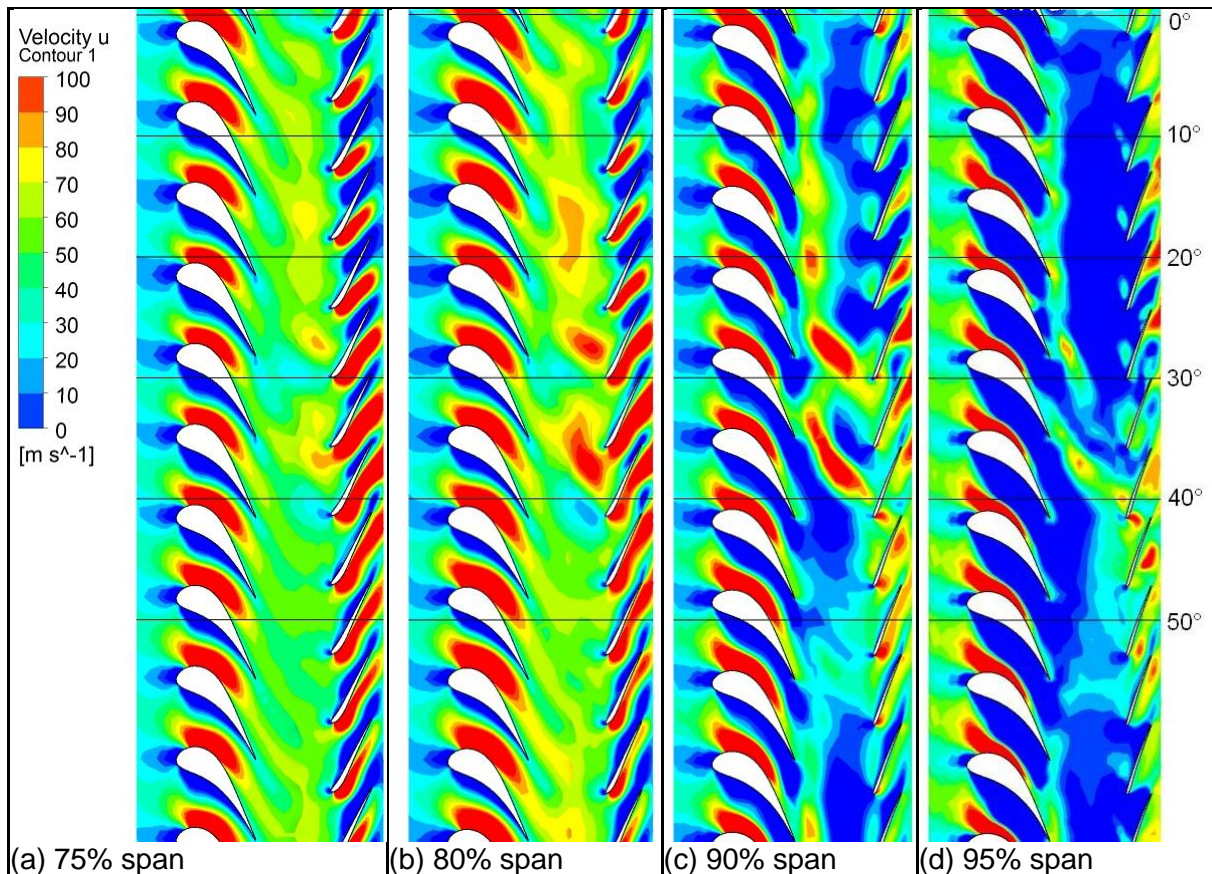


Figure 68: Blade-to-blade view for different span heights, axial velocity contour, CFD SAS model, steam model turbine (profile geometry is indicative for confidentiality reasons)

To better understand the roll-up of the casing vortex another illustration has been created containing 3D streamlines. Again, these streamlines should not be confused with path lines and represent the instantaneous velocity vectors, see Figure 69. Essentially, two regions around the circumference can be distinguished. In one region flow passes the rotor blade row although highly distorted by the radial upwards moving flow in the rotor passage. In this region no casing vortex is present. In the second region flow enters the passage and is swept upstream forming the casing vortex not allowing substantial through flow. The colour of the stream lines is indication the relative circumferential velocity of the fluid to the rotor blades. It can be observed that the flow which leaves the passage upstream, travels with the velocity of the rotor. Outside of the rotor passage in the gap between stator and rotor the flow reduces quickly tangential momentum moving against the direction of rotation in the rotor relative system. The flow is then forming the casing vortex and enters again the blade row at lower span sections. This mechanism causes the transport of the disturbances

against the rotor in the relative system. As the vortex interacts with the stationary and rotating blade row, see for example Figure 67 (c), a propagation velocity of about half the rotor tangential velocity seems plausible. The actual number of stall cells is most likely influenced by the space of the annular volume where they form and their spatial extent.

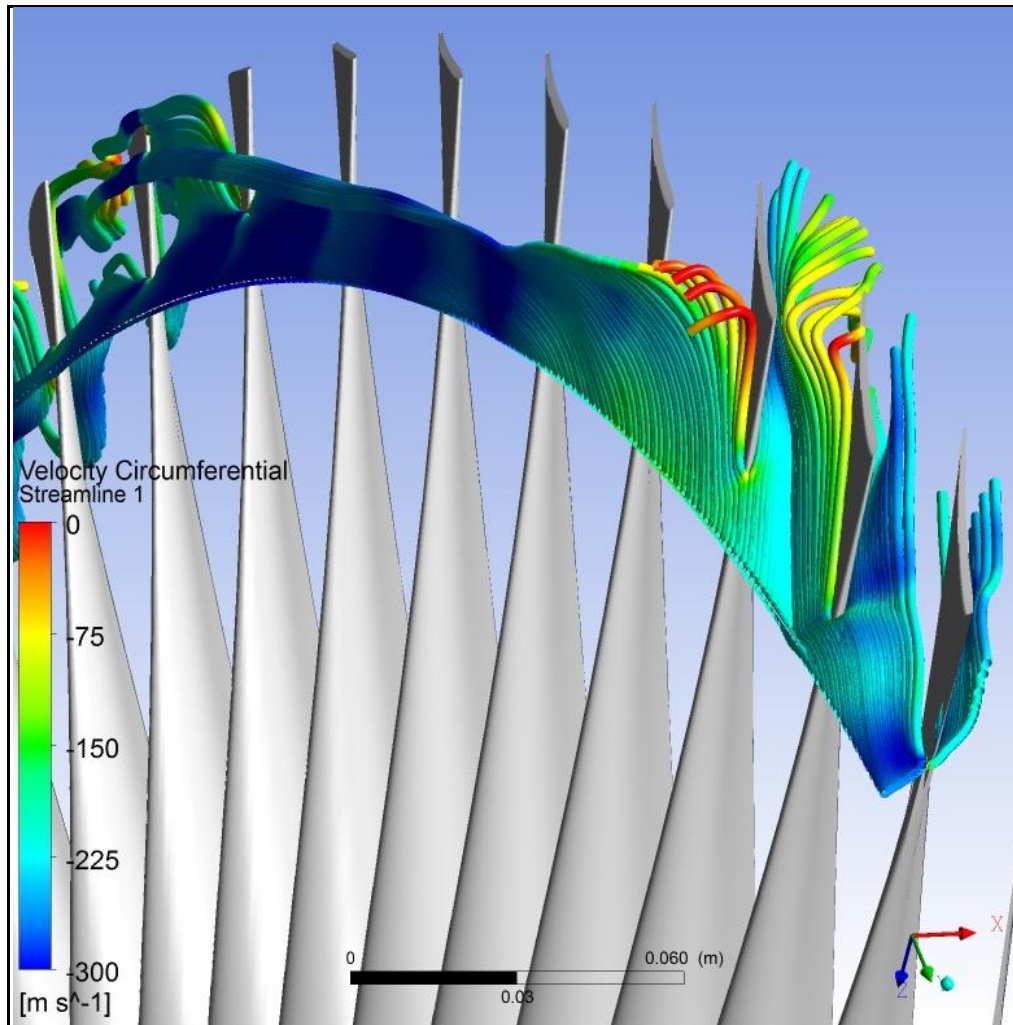


Figure 69: 3D steam lines entering the rotor blade row at 75% span contour colouring of the streamlines is the relative circumferential velocity in the rotor domain, SAS model, steam model turbine

In summary, the unsteady flow field under LVF can be seen as complex system of vortex structures. The casing vortex is unstable, leading to a pulsation of through flow in the tip region. Lower span sections of the LSMB do not transport fluid in a similar way due to the highly camber profiles with leading edges designed for positive angles of attack. Analogous to rotating stall, the propagation of the regions with reverse or stalled flow is moving against the direction of rotation in the relative frame of reference. Unlike compressor rotating stall it is not possible to understand or model the transport mechanism in a two-dimensional modelling approach. The major simplifications of the vortex flow would be unacceptable in this case.

In the appendix, the same set of illustrations is provided for the air model turbine. Although the turbine geometry is significantly different a similar unsteady flow field is present. One difference is that the casing vortex does not disappear completely during a stall cell passing. Nevertheless, the casing vortex significantly reduces in size and allows for more through flow for a short period of time as it was found in the steam model turbine.

## 4.9 Summary results and discussion

Table 6 concludes the sections on the results by listing all key numerical simulations performed. The major findings are listed in the right hand column.

Table 6: Overview of simulations and key findings

	Mesh	Turbulence model	Feature	Findings
<b>Backward facing step</b>	Fine	SST	One-to-one interface	Comparison with measurements
	Fine	SST	Mixing-plane	Same as on-to-one
<b>Vaneless diffuser</b>	Fine	Laminar	-	Rotating stall present
	Fine	SST	-	Rotating stall present
	Fine	SAS-SST	-	Rotating stall present
<b>Air model turbine - Full annulus</b>	Coarse	SST	-	No rotating stall
	Medium	SST	-	Rotating stall present
	Fine	SST	-	Cell fractional speed as medium mesh
	Medium	SAS-SST	Tip gap	Cell fractional speed close to measurement results
<b>Steam model turbine - Full cylinder</b>	Medium	SST	7 operating points	Ideal gas assumption valid, inlet conditions for full annulus calculation
<b>Steam model turbine - Full annulus</b>	Coarse	SST	-	No rotating stall
	Medium	SST	-	Weak rotating stall present
	Fine	SST	-	Weak rotating stall present
	Medium	SST	Tip gap	Weak rotating stall present
	Medium	SST	Realistic exhaust	Rotating stall present
	Medium	SAS-SST	Realistic exhaust	Cell fractional speed close to measurement results
	Medium	SAS-SST	Realistic exhaust and small tip gap	Tip gap has minor impact on low frequency stall cell
	Medium	SAS-SST	Realistic exhaust and large tip gap	Tip gap has minor impact on low frequency stall cell
	Medium	SAS-SST	Exhaust type 2 and large tip gap	Effect of exhaust is captured
	Medium	SAS-SST	Lowest volume flow	Trend against volume flow is captured
	Medium	SAS-SST	Higher volume flow	Trend against volume flow is captured

## 5. Conclusions

In the future, steam turbines have to be designed to allow more flexible operation conditions compared to the past. This has to be done while meeting other important targets such as efficiency, reliability and costs. The validation of LSMBs in low-pressure steam turbines for LVF operation is typically undertaken in model turbines. These validation campaigns are long and costly, in the case that vibration problems are detected the LSMB may need to be redesigned and again validated causing further delay in the product development. In this report, an unsteady aerodynamic phenomenon has been investigated in detail, which can lead to unallowable blade vibration under off design conditions. It has been shown that this effect can be investigated with both simplified model turbines and complex numerical modelling. It has also been shown that the fundamental mechanism is not an aero-elastic phenomenon and thus allowing a numerical investigation without fluid structure coupling.

Data from two different test rigs has been used to validate the numerical results. Both model turbines differ significantly in their blade geometry and flow path design, flow speed and working fluid. It has been shown that both turbines, instrumented with sophisticated measurement equipment, the characteristic rotating stall is present in the expected flow coefficient range. Different similarity parameters were discussed to understand the differences between model and full-scale machine. As it was found in open literature, the only deviating similarity parameter, the Reynolds number, does not significantly affect the results.

The investigation to find an appropriate CFD modelling approach has proven to be difficult. Not only were the models extremely large and required long computational times, different calculations did not show the expected unsteady phenomenon after many rotor revolutions. With a sufficiently fine computational grid the rotating stall phenomenon was triggered naturally after less than one rotor revolution and thus very long computational time. Many qualitative similarities with the measurement results have been observed. This includes the global time averaged flow field, the existence of a set of rotating stall cells and a two-banded unsteadiness close to the casing. Unfortunately, one of the key parameters was not captured correctly: the fractional speed relative to the rotor which determines, in combination with the number of stall cells, the excitation frequency. In order to be able to predict whether a LSMB is out of resonance during the development phase prior to a model turbine test a sufficiently accurate and reliable prediction is required. This deviation also indicated a basic problem in the modelling of the flow physics.

It has been discussed in detail whether a URANS approach as used in standard engineering practice is sufficient to resolve this particular unsteady flow phenomena correctly. Clearly, the turbulence models are not calibrated for the type of flow present under LVF conditions. It has also been pointed out that there is possibly no spectral gap between the large-scale turbulence and the coherent rotating stall flow structure. In standard turbulence models the eddy viscosity may damp out large scale vortex structures and lead to incorrect prediction of the unsteady phenomenon of interest.

A step towards resolving turbulent scales and therefore resolving the problems mentioned above has been made by employing the SAS-SST model. It has been identified as the best compromise between resolving large-scale turbulence and limiting the computational effort. Turbulent fluctuations have been resolved in the frequency range of interest, which has significantly improved the prediction capabilities. Although the effects on the time-averaged results were rather small, unsteady flow quantities such as the fractional speed could now be predicted very well if model parameters such as the grid density are calibrated correctly by measured data. For both very different model turbines, it was shown that the sophisticated

turbulent scale-resolving modelling is required to predict accurately the rotating stall phenomenon.

After obtaining results that were sufficiently close to the measurement, different effects on the unsteady behaviour have been investigated. As found in the measurements, the fractional speed is dependent on the flow coefficient. A high and low frequent set of disturbances is present with different sensitivities to the volume flow. The same result has been observed in the CFD calculation. The actual gradient between the air and steam model is nearly reversed indicating that this dependency is linked to the individual turbine geometry or Mach number.

In both measurement and CFD it has been shown that the rotating stall is highly sensitive to the exhaust geometry. Therefore, a sufficient modelling of the exhaust is required. The returning separated flow in the exhaust volume is influencing the strength and fractional speed of the stall cells. Unlike the exhaust, the tip clearance of the LSMB has only limited effect on the low frequency set of stall cells. It is clear that the effect is not caused by the leakage flow over the tip. Only the region very close to the casing is affected showing increased unsteady fluctuations. Higher frequency unsteady fluctuations are affected to a greater extent by the change of tip clearance.

Monitoring the change in time of the unsteady pressure field in the frequency domain revealed that changes to different stall cell numbers also occur in the CFD calculations despite the computational time being limited. Time traces from measurements have shown that individual stall cell counts can be present for several rotor revolutions. This means that if the full set of possible stall cell counts have to be resolved, the CFD calculation has to be performed for many more rotor revolutions. Nevertheless, CFD predicts the most dominant cell count in all the calculations. This allows checking for resonance with blade natural frequencies by assuming the presence of lower and higher cell numbers with the same fractional speed.

The aerodynamic excitation mechanism is complex with two dominant regions at the suction side fluctuating out of phase, this results in a two banded rotating stall. Unlike the impression from meridional illustrations of the flow field under LVF, the casing vortex between stator and rotor is not always present around the circumference alternating with the stall cell. Moreover, the casing vortex has been identified to play a key role for the propagation of the stall cells against the direction of rotation in the relative system. Regions where no casing vortex appears involve through flow similar to an axial compressor turning the flow toward the machine axis and increasing the pressure. In regions with casing vortex the flow is moved upstream rolling downstream again changing the inflow to passages further away at lower span heights. Although there are distinct differences with compressor rotating stall understanding such as the fact that a turbine is entering the unstable operating conditions with already highly separated flow, the similarities still outweigh the differences.

In conclusion, a detailed insight to the unsteady flow phenomenon under LVF in LP steam turbines has been gained using both measurement data and numerical modelling. A CFD approach has been developed to predict accurately the fractional speed, the cell count and geometrical dependencies of the stall cells being a benefit for both, future LSMB designs and further research investigating this phenomenon. Future LSMB configurations can be designed free of resonance with the LVF excitation mechanism and will therefore require model testing only for confirmation.



## 6. Proposals for further investigations

The investigation is based on two model turbine geometries and a limited number of operating points. In a first step, the validation matrix should be increased with more test cases where measurement data is available in terms of geometries and operating points. This is required to quantify the accuracy of the fractional speed prediction more precisely.

The CFD modelling approach presented can be used to study the sensitivities of the rotating stall on the blade geometry and other major design parameters such as the flow path design. Large parameter studies are usually not possible in model turbines because the manufacturing of many different blade geometries is too costly. CFD can give an insight how to influence the frequency and strength of the stall cells in an early stage of the LSMB design.

Presently the numerical simulations take too much time to be applied in a typical design iteration of an LSMB development. Possibilities should be explored how to reduce the computational effort. A further parallelisation would speed up the computation requiring even larger computational clusters. A relatively recent development for faster computations is the use of Graphics Processing Unit (GPU) technology. The processor architecture allows highly parallel computations, but the CFD code developed for Central Processing Units (CPUs) has to be rewritten.

For the presented study, aero-elastic effects have been disregarded. It is known from measurements that the stall cells interact with the blade vibration motion if resonance occurs. Such lock-in effects between fluid and structure can only be analysed with a coupled model including the flow and structural domain. It has been observed, that often the stall cell pressure fluctuations are relatively weak not causing excessive blade vibration even being in resonance with a natural frequency of the LSMB. A coupled computation would permit the computation of the limit cycle vibration amplitude and predict whether the alternating stress is situated within allowable range.

A major finding of the study was that standard turbulence modelling is not sufficient to capture the unsteady effects correctly. The employed SAS-SST model is a first step towards resolving large-scale turbulent fluctuations. If further validation studies show that the model is not sufficiently accurate, other approaches such as Detached Eddy Simulation (DES) or Large Eddy Simulation (LES) could be employed. Especially LES is currently, from an perspective of computational effort, far out of reach as a significantly finer computational mesh would be required while maintaining the full annulus modelling. DES approaches are therefore the most likely step forward to clarify if even better results can be achieved than with the SAS-SST model.

## 7. References

- [1] B. Troyanovskii, V. Lagun, E. Maiorskii, K. Noiman, and L. Simoyu, "Designing Steam Turbine Last Stages", *Teploenergetika*, vol. 17, pp. 16-20, 1970.
- [2] V. Lagun, Z. Simoyu, Y. Frumin, L. Povolotskii, and F. Sukharev, "Features of operation of a turbine stage with low Dml ratio under conditions of low loads", *Teploenergetika*, vol. 18, pp. 21-24, 1971.
- [3] Y. Shnee, F. Ponomarev, M. Fedorov, and L. Bystritskii, "Features of operation of a turbine stage with low Dm/l ratio under conditions of low loads", *Teploenergetika*, vol. 18, pp. 39-42, 1971.
- [4] A. Teufelberger, "Ventilation von Dampfturbinen bei Schwachlast, Leerlauf und Leistungsaufnahme", *VDI Berichte*, vol. 361, pp. 145-152, 1980.
- [5] Y. Shnee, O. Ponomarev, V. Slabchenko, M. Zatsev, and M. Fedorov, "Influence of the operational factors on dynamic stresses in moving blades of a turbine stage", *Teploenergetika*, vol. 21, pp. 49-52, 1974.
- [6] W. Engelke, M. Gloger, W. Maly, and H. Termuehlen, "Large steam turbine free-standing blade development based on 30 years of experience", in *AMERICAN POWER CONFERENCE*, Chicago, Illinois, 1978.
- [7] M. Gloger, K. Neumann, and H. Termuehlen, "Design Criteria for Reliable Low-Pressure Blading", *ASME*, vol. 86-JPGC-Pwr-42, 1986.
- [8] A. Kondakov, L. Simoyu, and V. Lagun, "Investigation of the Restistance to Vibration of the Moving Blades of the Low-pressure Cylinders of a High-capacity Steam Turbine", *Teploenergetika*, vol. 33 pp. 665-669, 1986.
- [9] H. Stetter and C. Besigk, "Auslegung und Betrieb von ND-Endstufen unter Berücksichtigung stark variabler Strömungsverhältnisse", *MAN*, 1985.
- [10] D. Schmidt and W. Riess, "Steady and unsteady flow measurements in the last stages of LP steam turbines", in *3rd European Turbomachinery Conference*, London, 1999, pp. 723-734.
- [11] R. Pigott and J. Abel, "Vibrations and Stability of Turbine Blades at Stall", *Transactions of the ASME Journal of Engineering for Power*, pp. 201-208, 1974.
- [12] A. G. Kostyuk, "Vibrations of the Moving Rows of the Last Stages of a Steam Turbine under Off-design Operation conditions", *Thermal engineering*, vol. 30, pp. 22-26, 1983.
- [13] O. J. R. Queune and L. He, "Experimental Study of 3D Unsteady Flow Around Oscillating Blade With Part-Span Separation", *Journal of turbomachinery*, vol. 123, pp. 519-525, 2001.
- [14] W. Gerschütz, *Experimentelle Untersuchung von rotierenden Strömungsinstabilitäten im Betriebsbereich der Ventiation einer Niederdruck-Dampfturbine*. Düsseldorf: VDI Verlag, 2006.
- [15] F. Truckenmüller, "Untersuchung zur aerodynamisch induzierten Schwingungsanregung von Niederdruck-Laufschaufeln bei extremer Teillast", *ITSM, Universität Stuttgart*, 2002.
- [16] I. Usachev, E. Efimenko, V. Il'nikh, V. Kolyasnikov, and V. Neumim, "Excitation of axial Oscillations of Steam Turbine Rotors under operating Conditions", *Energomashinostroenie*, vol. 3, pp. 5-9, 1981.
- [17] M. Petrovic and W. Riess, "Off-design flow analysis of low-pressure steam turbines", *Proceedings of the Institution of Mechanical Engineers, Part A: Journal of Power and Energy*, vol. 211, pp. 215-224, 1997.
- [18] N. Herzog, Y. Gundogdu, G. Kang, J. R. Seume, and K. Rothe, "Part Load Operation of a Four-Stage Turbine", *ASME Conference Proceedings*, vol. 2005, pp. 663-672, 2005.



- [19] R. Sigg, "Numerical and experimental investigation of a low-pressure steam turbine during windage", *Proceedings of the Institution of Mechanical Engineers; Part A: Journal of Power and Energy*, vol. 223, p. 697, 2009.
- [20] L. Y. Zhang, L. He, and H. Stüer, "A Numerical Investigation of Rotating Instability in Steam Turbine Last Stage", *Journal of turbomachinery*, vol. 135, pp. 011009-011009, 2012.
- [21] L. Y. Zhang, L. He, and H. Stüer, "3-D TIME DOMAIN UNSTEADY COMPUTATION OF ROTATING INSTABILITY IN STEAM TURBINE LAST STAGE", in *Proceedings of ASME Turbo Expo, Copenhagen, 2012*.
- [22] M. Vahdati, A. I. Sayma, M. Imregun, and G. Simpson, "Core-Compressor Rotating Stall Simulation with a Multi-Bladerow Model - Unsteady Aerodynamics, Aeroacoustics and Aeroelasticity of Turbomachines", K. C. Hall, et al., Eds., ed: Springer Netherlands, 2006, pp. 313-329.
- [23] C. Rotta, *Turbulente Strömungen*. Stuttgart: B. G. Teuber, 1972.
- [24] A. Hussain, "Coherent structures and turbulence", *Journal of Fluid Mechanics*, vol. 173, 1986.
- [25] Y. Kubota, T. Suzuki, H. Tomita, T. Nagafugi, and C. Okamura, "Vibration of Rotating Bladed Disc Excited by Stationary Distributed Forces", *Bulletin of JSME*, vol. 26, pp. 1952-1957, 1983.
- [26] L. He, "Computation of unsteady flow through steam turbine blade rows at partial admission", *Proceedings of the Institution of Mechanical Engineers, Part A: Journal of Power and Energy*, vol. 211, pp. 197-205, 1997.
- [27] E. M. Greitzer, "Surge and Rotating Stall in Axial Flow Compressors—Part I: Theoretical Compression System Model", *Journal for Engineering for Power*, vol. 98, pp. 190-198, 1976.
- [28] R. Mailach, I. Lehmann, and K. Vogeler, "Rotating Instabilities in an Axial Compressor Originating From the Fluctuating Blade Tip Vortex", *Journal of turbomachinery*, vol. 123, pp. 453-460, 2001.
- [29] I. J. Day and N. A. Cumpsty, "The Measurement and Interpretation of Flow within Rotating Stall Cells in Axial Compressors ", *Journal of Mechanical Engineering Science*, vol. 20 No. 2, pp. 101-114, 1978.
- [30] T. R. Camp and I. J. Day, "1997 Best Paper Award—Turbomachinery Committee: A Study of Spike and Modal Stall Phenomena in a Low-Speed Axial Compressor", *Journal of turbomachinery*, vol. 120, pp. 393-401, 1998.
- [31] M. Inoue, M. Kuroumaru, T. Tanino, and M. Furukawa, "Propagation of Multiple Short-Length-Scale Stall Cells in an Axial Compressor Rotor", *Journal of turbomachinery*, vol. 122, pp. 45-54, 1999.
- [32] N. Kaemmer and M. Rautenberg, "A Distinction Between Different Types of Stall in a Centrifugal Compressor Stage", *Journal of Engineering for Gas Turbines and Power*, vol. 108, pp. 83-92, 1986.
- [33] S. Ljevar, H. De Lange, and A. Van Steenhoven, "Two-dimensional rotating stall analysis in a wide vaneless diffuser", *International Journal of Rotating Machinery*, vol. 2006, 2006.
- [34] S. Ljevar, "Rotating Stall in Wide Vaneless Diffusers", *Dissertation, Eindhoven University of Technology*, 2007.
- [35] P. G. Drazin and W. H. Reid, *Hydrodynamic stability*: Cambridge university press, 2004.
- [36] W. Gerschütz, M. Casey, and F. Truckenmüller, "Experimental investigations of rotating flow instabilities in the last stage of a low-pressure model steam turbine during windage", *Proceedings of the Institution of Mechanical Engineers, Part A: Journal of Power and Energy*, vol. 219, pp. 499-510, 2005.
- [37] I. McBean, S. Havakechian, and P. Masserey, "The Development of Long Last Stage Steam Turbine Blades", in *Proceedings of ASME Turbo Expo: Power for Land, Sea and Air, Glasgow, 2010*.

- [38] M. Hembera, F. Danner, M. Kainz, and H.-P. Kau, "Comparing Frequency-Based Flow Solutions to Traditional Unsteady Fluid Dynamics Analysis in Turbomachinery", in *High Performance Computing in Science and Engineering, Garching/Munich 2009*, S. Wagner, et al., Eds., ed: Springer Berlin Heidelberg, 2010, pp. 161-174.
- [39] ANSYS CFX-Solver Theory Guide. Canonsburg, PA, 2006.
- [40] M. J. Raw, *A new control-volume-based finite element procedure for the numerical solution of the fluid flow and scalar transport equations*, 1986.
- [41] F. R. Menter, "Best Practice: Scale-Resolving Simulations in ANSYS CFD", ed: ANSYS Germany GmbH, 2012.
- [42] J. Fröhlich and D. von Terzi, "Hybrid LES/RANS methods for the simulation of turbulent flows", *Progress in Aerospace Sciences*, vol. 44, pp. 349-377, 2008.
- [43] P. Tucker, "Computation of unsteady turbomachinery flows: Part 1—Progress and challenges", *Progress in Aerospace Sciences*, vol. 47, pp. 522-545, 2011.
- [44] P. G. Tucker, *Computation of unsteady internal flows: fundamental methods with case studies: Kluwer Academic Publishers*, 2001.
- [45] H. Lübcke, S. Schmidt, T. Rung, and F. Thiele, "Comparison of LES and RANS in bluff-body flows", *Journal of Wind Engineering and Industrial Aerodynamics*, vol. 89, pp. 1471-1485, 2001.
- [46] F. R. Menter, "Two-equation eddy-viscosity turbulence models for engineering applications", *AIAA Journal*, vol. 32, pp. 1598-1605, 1994.
- [47] F. Menter and Y. Egorov, "The Scale-Adaptive Simulation Method for Unsteady Turbulent Flow Predictions. Part 1: Theory and Model Description", *Flow, Turbulence and Combustion*, vol. 85, pp. 113-138, 2010.
- [48] H. Schulte, "Zur numerischen Simulation abgelöster, turbulenter Strömungen mit der Finite-Elemente-Methode", *Mitteilungen Institut für Wasserbau und Wasserwirtschaft, RWTH Aachen*, 1989.
- [49] H. Le, P. Moin, and J. Kim, "Direct numerical simulation of turbulent flow over a backward-facing step", *Journal of Fluid Mechanics*, vol. 330, pp. 349-374, 1997.

## Appendix: Air model turbine stall cell visualisation

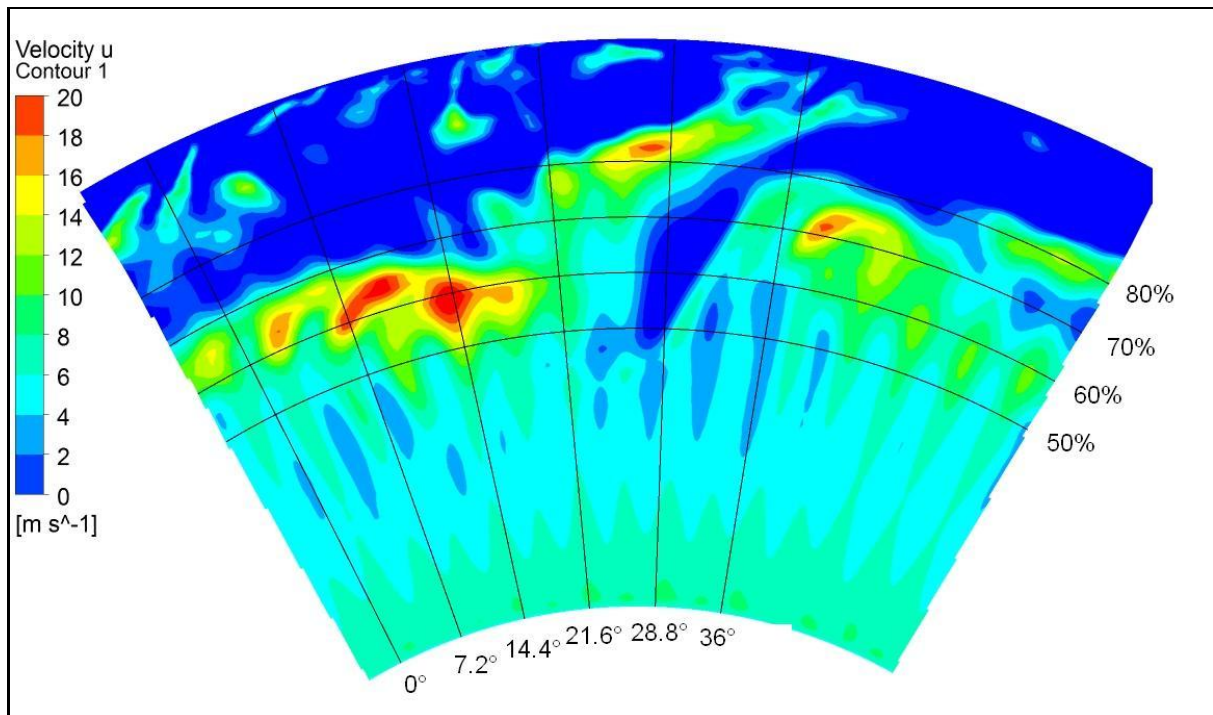


Figure 70: Plane perpendicular to the machine axis at a 50% axial location between stator trailing edge and rotor leading edge, CFD SAS model, air model turbine

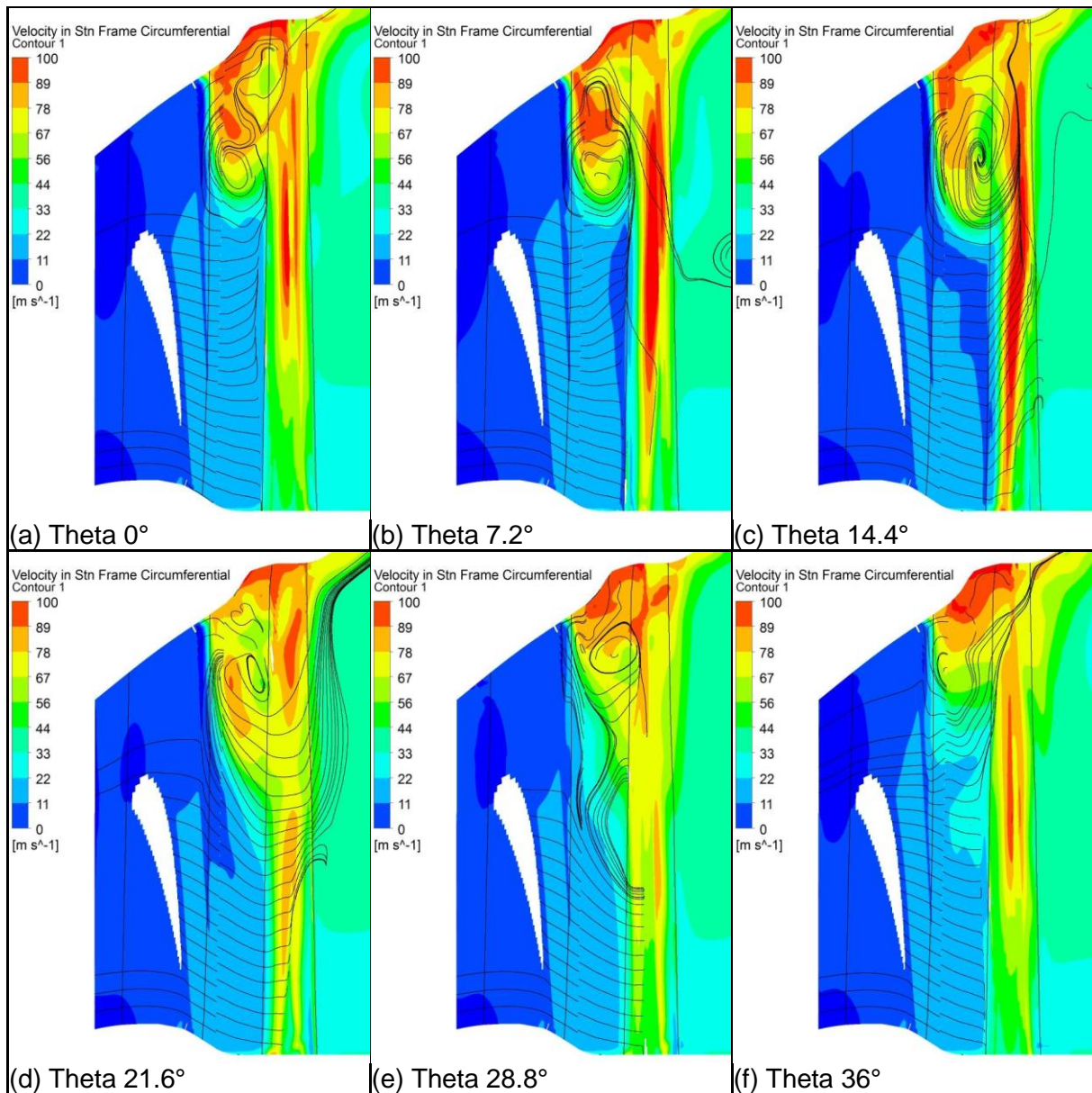


Figure 71: Meridional cuts at different theta positions, CFD SAS model, air model turbine



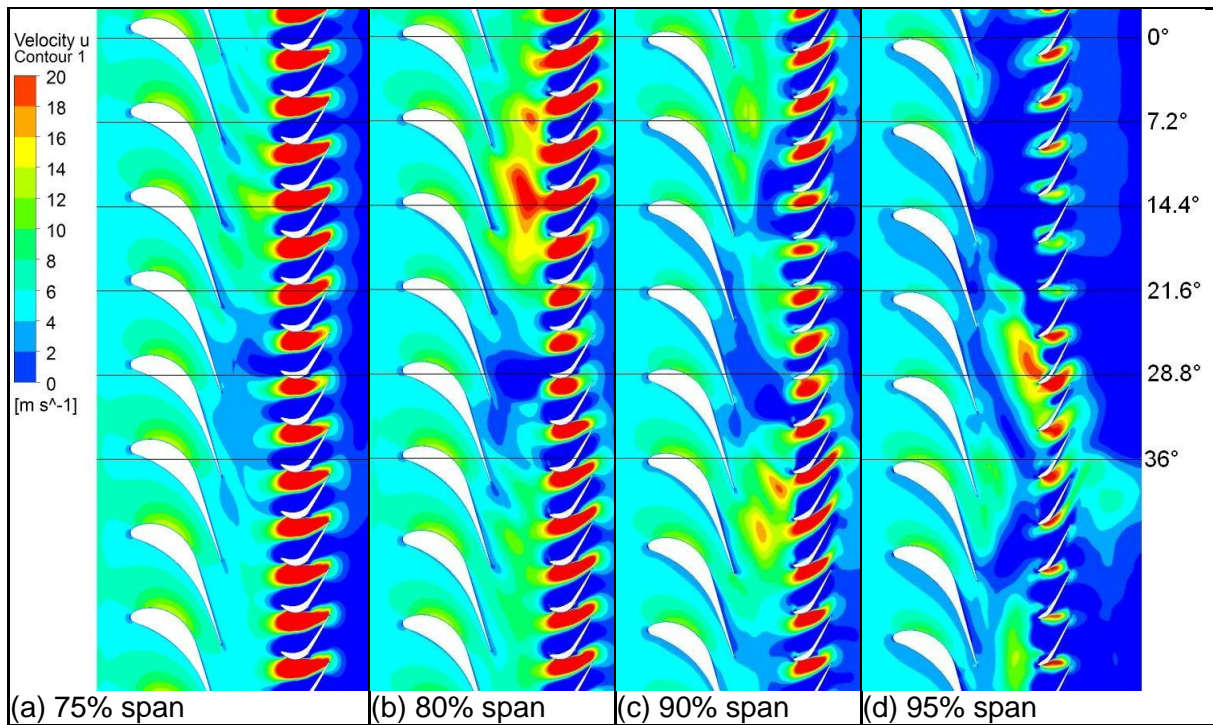


Figure 72: Blade-to-blade view for different span heights, axial velocity contour, CFD SAS model, air model turbine (profile geometry is indicative for confidentiality reasons)

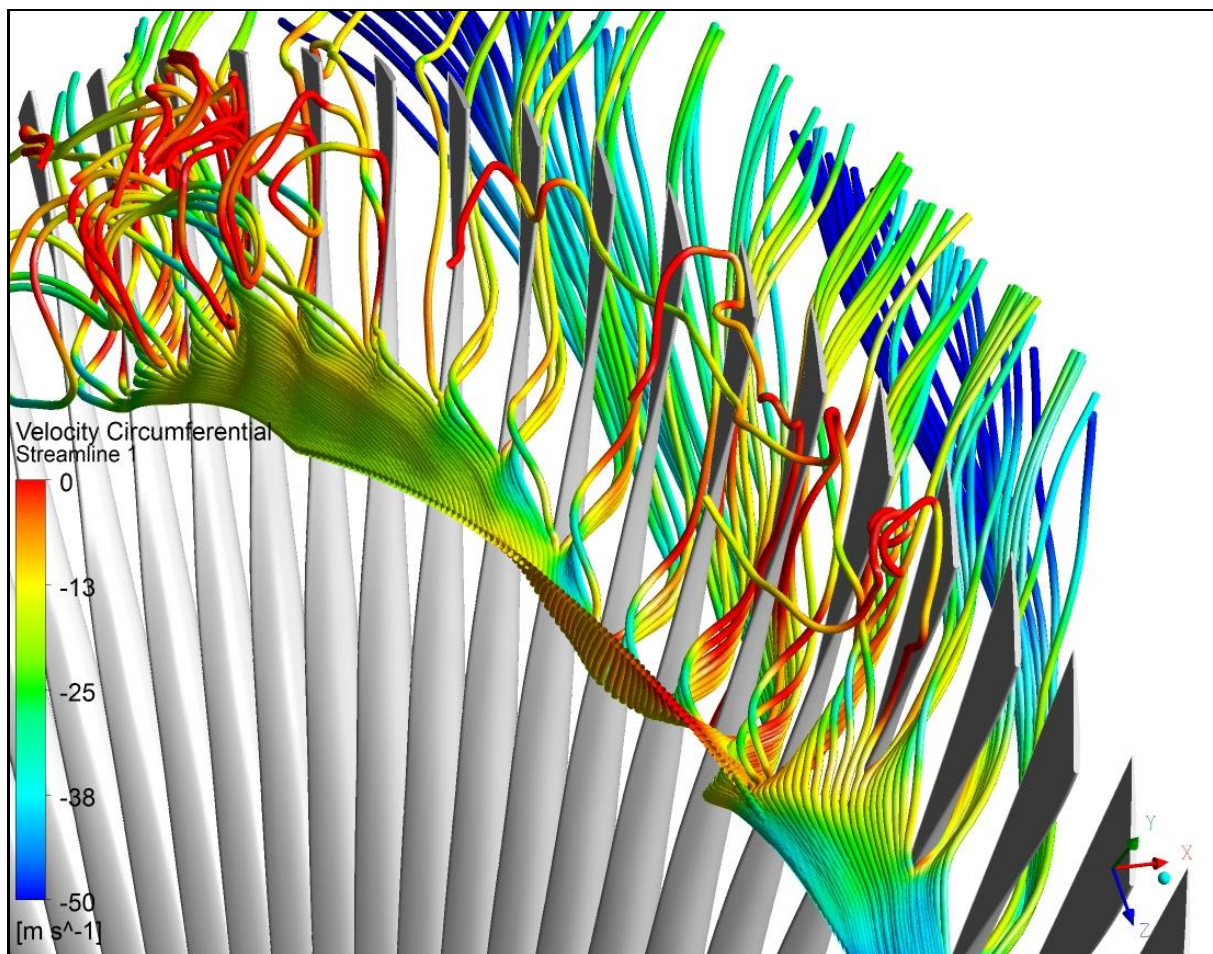


Figure 73: 3D stream lines entering the rotor blade row at 75% span contour colouring of the streamlines is the relative circumferential velocity in the rotor domain, SAS model, air model turbine

# Curriculum vitae

## Personal Details

---

Name: Benjamin Megerle  
Date of birth: 14.05.1983  
Place of birth: Donaueschingen, Germany  
Nationality: German  
Address: Hellmutstrasse 8, CH-8004 Zürich  
E-Mail: benjamin.megerle@gmail.com

## Work experience

---

### ALSTOM (Switzerland) Ltd., Baden, Switzerland

Since  
December 2011

- Technical Project Leader - Aero Numerical Tools
- Steam Turbines R&D - Core Technology Program
- Development and maintenance of in-house aero numerical tools and R&D turbine design system
- Supervision of consulting developer team

Since  
April 2008

- Aerodynamic Design Engineer
- Steam Turbines R&D Execution Last Stage & Special Blades
- Aerodynamic design and analysis of low pressure steam turbine blades

April 2006 -  
Sep. 2006

### Rolls Royce plc., Bristol und Derby, United Kingdom

- Industrial placement
- Development of a design tool for the optimisation of air-cooled turbine blades.

## Education

---

Since  
April 2010

### External PhD student at the EPFL in Lausanne:

- Doctoral program in Energy

Oct. 2002 –  
March 2008

### University of Stuttgart – Course of Studies: Mechanical Engineering

- Main subjects: Thermal Turbomachinery and Applied Dynamics

## Publications

---

- ASME Turbo Expo 2012, Copenhagen, Denmark - GT2012-68384, Best Paper Award Steam Turbines Committee
- Journal of Engineering for Gas Turbines and Power 2013 - GTP-12-1199
- ASME Turbo Expo 2013, San Antonio, Texas, USA - GT2013-95409